

DISS. ETH NO. 26301

Millimeter Precision Non-Invasive Targeted Drug Delivery to Brain

A thesis submitted to attain degree of
DOCTOR OF SCIENCES of ETH Zurich
(Dr. sc. ETH Zurich)

presented by
Mehmet Sirin Ozdas

MSc Imperial College London

born on 25.02.1986

citizen of
Republic of Turkey

accepted on recommendation of
Prof Mehmet Fatih Yanik, examiner
Prof. Klaas Enno Stephan, co-examiner
Prof. Shashank Sirsi, co-examiner

2019

"Once upon a time, I, Zhuangzi, dreamt I was a butterfly, fluttering hither and thither, to all intents and purposes a butterfly. I was conscious only of my happiness as a butterfly, unaware that I was Zhuangzi. Soon I awakened, and there I was, veritably myself again. Now I do not know whether I was then a man dreaming I was a butterfly, or whether I am now a butterfly, dreaming I am a man. Between a man and a butterfly there is necessarily a distinction. The transition is called the transformation of material things."
Zhuangzi

To my mother Şükrüye, my father Abdullah and all my family members.

Acknowledgment

PhD was a long and difficult journey and it would not be possible without having support from my lab members, family and friends.

I would like to sincerely thank to:

My supervisor, **Prof. Mehmet Fatih Yanik**, for giving me chance to work on this exciting project and supporting me for various aspects of my life during PhD. I met him in a time that I was lost and trying to find my way. He thankfully helped me find my passion and provided research facilities and guidance.

My colleagues **Aagam Shah** and **Dr. Paul Johnson** for all their support and providing a good ambience for the team work. From the very beginning we worked together and without their support and contribution, this work would not be possible. This project was tremendously difficult, we had to try many different things until we reached this level.

Dr. Wolfger von der Behrens for guiding us with animal experiments, electrophysiology, data analysis, feedback for my thesis and many other lab related issues.

Markus Marks, Tansel Baran Yasar, Prof. Shashank Sirsi, Nisheet Patel, Bifeng Wu, Dr. Mostafa Rezaie, Newsha Nejad Ghasemi, Gwendolyn English, Dr. Thom Gent, Clemens Dlaska, Stephan Ihle and all other **Neurotechnology Laboratory members** for their support. Especially **Markus** and **Baran** helped me a lot.

Beat Werner for being so generous to share his 20 years FUS expertise, providing many instruments and giving feedback on the manuscripts.

Semester project and internship students: **Orhun Caner Eren, Abdulkadir Gökçe, Michael Matter, Ekrem Fatih Yılmaz, Ahmet Uslu, Alexandra Greter, Ljubica Chimesa, Sophie Skriabine** and **Fabrizo Broca** for all their contributions to the project.

Sonja Bamert for all her help during establishment of the lab at ETH Zurich, employment and visa applications during transition times between MIT and ETH Zurich and for many other seemingly small but important things.

Janice Balzer who patiently helped me for administrative issues during my visit year at MIT.

My Friends in Boston: **Yusuf Karaca, Dr. Fikret Altunkılıç, Abulvahap Bekgöz, Süleyman Yıldız, Burak Sancaktar** for their support during my time in Boston.

Yasemin Tomaschett, from D-ITET doctoral administration, for kindly replying all my e-mails regarding PhD.

All cleaning staff of UZH for cleaning our labs every day.

Institute of Neuroinformatics administrators: **Kathrin Aguilar, Simone Schumacher, Maik Brechten** and **David Lawrence** for kind helps for many different administrative issues.

Dr. Frank Rodden for sharing his knowledge on psychiatry.

My old advisors **Prof. Giacomo Indiveri** (Institute of Neuroinformatics) and **Prof. Timothy Constandinou** (Imperial College London) for their kind support even after I left their lab. **Prof. Kevin Alloway** from Pennsylvania State University and **Prof. Angel Nunez** from Autonomous University of Madrid, **Prof. Ehud Ahissar** from Weizmann Institute, **Prof. Mathew Diamond** from SISSA for their kind answers regarding their papers when I was trying to find my way for establishing vS1-vM1 paradigm.

My Friends in Zurich: **Göktuğ Alkan**, **Onur Fişek**, **Nuri Usta**, **Bilal Yılmaz**, **Dr. Mustafa Boyvat**, **Dr. Ibrahim Ethem Güney**, **Harun Torlakçık**, **Dr. Kemal Çelebi** and **Dr. Abdullah Kahraman** for their continuous support and friendship.

My Friends in Turkey: **Talha Karademir**, **Dr. Engin Koç**, **Ahmet Cevdet Ediz** and **Dr. Mehmet Ali Türkmenoğlu** for their continuous support and friendship.

My mother and my father for being so patient, so loving and always trusting me. My siblings; **Faysal**, **Naciye**, **Selma**, **Songül**, **Naci**, **Gülsüm** and **Veysi** for being so supportive. I apologize to my nephews and nieces for not seeing their growth. And I also apologize to my uncle **Emin Gegin** whom I lost during PhD.

My brother in law **Cemalleddin Acay**, his friends; **Aşkın Akdağ**, **Serdar Aktan** and my brother's (Prof. Faysal Özdaş) friend **Prof. Vahap Özpolat** for their sincere support.

Silvio Scherr and **Reto Maier** and their team from UZH Physics Institute Machine Shop for providing us high quality machining service.

Jemere Ruby for rat and ultrasound illustrations.

My PhD committee **Prof. Klaas Enno Stephan** and **Prof. Shashank Sirsi** for being in my committee and providing valuable feedback.

I would also like to thank **ETH Zurich** for providing excellent research and educational facilities. It was great honor to walk in the corridors where Albert Einstein and many other great scientists has walked and is walking. The year I spent at **MIT** was also great time, I would like to thank all friends I met there. It was wonderful and productive time.

Table of Contents

Table of Contents	5
Abstract	11
Zusammenfassung	12
Chapter 1	14
Introduction and Motivation	14
Chapter 2	18
Focused ultrasound mediated drug delivery through intact blood-brain barrier with millimeter precision	18
2.1 Introduction	18
2.2 Results	21
2.2.1 Ultrasound-controlled drug carriers, <i>in-vitro</i> characterization and optimization	21
2.2.2 <i>In-vivo</i> modulation of a cortical circuit: vS1-vM1	27
2.2.3 Drug does not diffuse to off-target sites	34
2.2.4 Blood-Brain Barrier integrity	38
2.3 Methods	41
2.3.1 Ultrasound controlled-drug carriers	41
2.3.2 Animal preparation	42
2.3.3 Surgery	42
2.3.4 Whisker stimulation	42
2.3.5 FUS sequences	43
2.3.6 Electrophysiology and FUS drug delivery for vS1-vM1	43
2.3.7 Electrophysiology and FUS drug delivery for vS1-V1	44
2.3.8 Visual stimulation	44
2.3.9 Electrophysiology and LIFU	45
2.3.10 Simultaneous vS1 and vM1 recordings	45
2.3.11 <i>In-vitro</i> FUS characterization	45
2.3.12 Electrophysiology data analysis	46
2.3.13 Histology and IVIS spectrum imaging	47
2.3.14 MRI imaging	47
2.3.15 Extraction of muscimol from muscimol loaded UC-carriers for LC-HR-MS/MS quantification	48
2.3.16 Quantification of muscimol with LC-HR-MS/MS	48
2.3.17 Statistical analysis	50
2.4 Discussion	50
Chapter 3	54
Automated 3D-scanning system for fast characterization of transcranial focused ultrasound fields in rodent skull	54
3.1 Introduction	54
3.2 Results	56
3.2.1 Scanning FUS beam with and without skull <i>ex-vivo</i>	56

3.3 Methods.....	59
3.3.1 Experimental setup and FUS pressure distribution measurement protocol.....	59
3.3.2 Calibration of optical distance sensor	60
3.3.3 FUS setup and transducer calibration	60
3.3.4 Calculation of skull transmission factor.....	62
3.3.5 Degassing water.....	62
3.3.6 μ CT imaging and 3D image reconstruction.....	63
3.4 Discussion	64
Chapter 4.....	65
Transient seizures followed by FUS induced BBB opening.....	65
4.1 Introduction	65
4.2 Results	67
4.3 Methods.....	72
4.3.1 Focused Ultrasound.....	72
4.3.2 Electrophysiology data analysis	72
4.4 Discussion	74
Chapter 5.....	76
Concluding Remarks	76
Chapter 6.....	80
Appendix	80
References.....	83

List of Abbreviations

tFUS=Transcranial Focused Ultrasound Stimulation

DBS=Deep Brain Stimulation

BBB=Blood-Brain Barrier

LIFU=Low Intensity Focused Ultrasound

TMS=Transcranial Magnetic Stimulation

PRF=Pulse Repetition Frequency

MI=Mechanical index

PNP=Peak Negative Pressure

NOC=Number of Cycles.

MPa=Megapascal

vM1=Vibrissae Motor Cortex

vS1=Vibrissae Sensory Cortex (Barrel Cortex)

wEP=Whisker Evoked Potential

VEP=Visually Evoked Potential

eLFP=Evoked Local Field Potential

FDA=Food and Drug Administrations

GABA= Gamma-Aminobutyric Acid

FUS+MBs=Focused Ultrasound and Microbubbles

TZ=Transitional Zone

MRI=Magnetic Resonance Imaging

EB=Evans Blue

CNS=Central Nervous System

HU=Hounsfield Units

List of Figures

Figure 2.1 Concept of focal aggregation and uncaging of ultrasound-controlled drug carriers (UC-carriers).....	20
Figure 2.2 In-vitro characterization of focal aggregation and uncaging of drugs from ultrasound-controlled carriers (UC-carriers).....	25
Figure 2.3 BBB Opening following sonication in-vivo using in-vitro AU-FUS (1) parameters.....	26
Figure 2.4 UC-carrier and liposome Size Distributions	27
Figure 2.5 Projections from vS1 to vM1 (TZ region) and the map of TZ region on vM1 from top.....	29
Figure 2.6 Functional and anatomical connectivity between vS1 and vM1	30
Figure 2.7 Experimental setup for in-vivo drug delivery in vS1-vM1 paradigm.....	30
Figure 2.8 BBB opening in vS1 with FUS+MBs and BBB opening in vM1 due to probe insertion.....	31
Figure 2.9 In-vivo receptor-specific and focal modulation of vS1-vM1 circuitry by AU-FUS sequence and UC-Carriers.	32
Figure 2.10 Drug doesn't diffuse to off-target sites.....	36
Figure 2.11 Blood-brain barrier integrity following our AU-FUS sequence and conventional Burst-FUS.	39
Figure 3.1 3D, 2D and 1D Scan of FUS intensity with and without skull.....	57
Figure 3.2 Validation of a numerical model with experimental data collected with our method.....	58
Figure 3.3 Schematic for automated pressure mapping system of skull effects on FUS..	61
Figure 3.4 Real setup images and scanning protocol.....	61
Figure 3.5 Demonstration of water and skull degassing setups.	63
Figure 4.1 Graphical abstract of the experimental setup.	68
Figure 4.2 FUS induced cortical seizure characterization.	70
Figure 4.3 BBB opening following FUS sonication.....	71
Figure 6.1 Chromatograms of ISTD at 200 ng/mL (top) and muscimol standard solution at 2 ng/mL (bottom) concentration measured with LC-HR-MS/MS.....	81
Figure 6.2 Calibration curve of muscimol standard solutions used for quantification. ...	82

List of Tables

Table 2-1 FUS Parameters used for in-vivo and in-vitro experiments.....	26
Table 4-1 Example of Ultrasound sequences for BBB opening.....	70
Table 6-1 Preparation of the standard and ISTD solutions used for quantification.	80
Table 6-2 Weighted and measured concentrations.	81

Declaration

I hereby confirm that the work presented in this thesis is my own, except as specified in the text and described below.

The ultrasound sequence was designed by the collective ideas of Aagam Shah, Paul Johnson, and me.

The ultrasound-controlled drug carriers were designed by Aagam Shah along with Shashank Sirsi's guidance. The carriers were prepared by Aagam Shah, Nisheet Patel and Paul Johnson. The *in-vitro* studies were designed and performed by Aagam Shah and Nisheet Patel.

Paul Johnson designed histology experiments with the help of Aagam Shah. Paul Johnson and Aagam Shah performed perfusions and histology (with the help of Nisheet Patel) and took the IVIS spectrum images using UZH Microscopy Center. Aagam Shah performed image analysis.

I used some parts of scripts for LFP analysis and spike sorting pipeline developed by Tansel Baran Yasar and Celemens Dlaska.

Markus Marks collected MRI images and analyzed the data.

Wolfger von der Behrens helped installing electrophysiology setup and guided with data analysis.

Hazael Montranou tested the skull data with their numerical skull model. μ CT of skulls were taken by Jolanda Baumgartner. Skulls were prepared by Paul Johnson and me.

Paul Johnson and Aagam Shah performed extractions for the muscimol loading and Urs Stadler and Laurent Bigler performed the LC-HR-MS/MS.

Abstract

Targeted non-invasive drug delivery to the brain could lead to great advancements in the treatment of psychiatric disorders by enabling circuit- and receptor-specific modulation of regions that drive disease pathology. To this end, we developed ultrasound-controlled drug carriers and designed a unique two component ultrasound sequence that achieves high drug concentration in local brain regions without Blood-Brain Barrier (BBB) opening. We systemically inject the drug loaded carriers, following which our ultrasound sequence repeatedly aggregates and then uncages the drugs in the brain region of interest. As a proof of concept, we test this method in the rat brain where we inhibit information flow from vibrissae sensory cortex (vS1) to vibrissae motor cortex (vM1). We load the ultrasound-controlled drug carriers with muscimol (an ionotropic GABA_A receptor agonist) which readily crosses the BBB, we sonicate in vS1 and record evoked neural activity with a penetrating multi-electrode array from vM1. We show that the method requires orders of magnitude less drug than systemic drug delivery to achieve equivalent inhibition in the same brain region and we show that drug delivery is confined to a small area by recording from a cortical circuit which is not involved the information flow between vS1 and vM1. Using MRI contrast agents and Evans Blue dye, which do not cross the intact BBB, we show that we deliver drug without BBB opening. Moreover, we show that Focused Ultrasound and microbubbles assisted BBB (FUS+MBs) opening causes repeated transient seizures at gamma frequency range which are followed by silent periods, revealing more insight into consequences of FUS+MBs assisted BBB opening and further underscoring the concerns regarding its safety. Finally, we introduce an affordable, automated 3D scanning system for measuring skull induced distortions on FUS beam. The system helps in determining pressures used for the FUS sequence that we designed for our drug delivery method and could be used to validate numerical skull models in a fast and reliable manner. Collectively, these works significantly expand on neurotechnologies and basic neuroscience.

Zusammenfassung

Die lokale, nicht-invasive Verabreichung von Wirkstoffen im Gehirn könnte zu großen Fortschritten bei der Behandlung von psychiatrischen Störungen führen, indem Gehirnregionen, die für die Pathologie verantwortlich sind, schaltkreis- und rezeptorspezifisch moduliert werden. Zu diesem Zweck haben wir ultraschallempfindliche Wirkstoffträger und eine spezielle Ultraschallsequenz bestehend aus zwei Komponenten entwickelt, mit der eine hohe Wirkstoffkonzentration in lokalen Hirnregionen erzielt werden kann, ohne dabei die Blut-Hirn-Schranke (BHS) zu öffnen. Dabei injizieren wir systemisch die geladenen Wirkstoffträger, welche dann durch die spezielle Ultraschallsequenz wiederholt aggregiert werden und anschließend den Wirkstoff in der zu behandelnden Hirnregion freisetzen. Als „Proof of Concept“ testen wir diese Methode am Gehirn von Ratten, wo wir den Informationsfluss vom somatosensorischen Kortex der Schnurrhaare (vS1) zum motorischen Kortex der Schnurrhaare (vM1) hemmen. Dabei beladen wir die ultraschallempfindlichen Wirkstoffträger mit Muscimol (einem ionotropen GABA_A-Rezeptoragonisten, der die BHS passieren kann), beschallen vS1 und messen die evozierte neuronale Aktivität in vM1 mithilfe eines Multielektrodenarrays. Wir zeigen, dass diese Methode eine um viele Größenordnungen geringere Wirkstoffmenge im Vergleich zur systemischen Gabe benötigt, um eine vergleichbare Hemmung der neuronalen Aktivität zu erreichen. Zudem zeigen wir mithilfe von elektrophysiologischen Messungen in einem anderen kortikalen Schaltkreis, der nicht den Informationsfluss zwischen vS1 und vM1 involviert, dass bei dieser Methode die Wirkstoffabgabe auf einen kleinen Gehirnbereich beschränkt ist. Mit Hilfe von zwei Markern, die die BHS nicht passieren (einem Kontrastmitteln für die Magnetresonanztomographie und Evans Blue-Farbstoff), können wir nachweisen, dass bei unserem Ansatz der Wirkstoff abgegeben wird ohne die BHS zu öffnen. Darüber hinaus zeigen wir, dass die Kombination von fokussiertem Ultraschall (FUS) und Mikrobläschen (MB) die Blut-Hirn-Schranke (FUS + MBs) öffnen kann und dies zu vorübergehender, anfallartiger neuronaler Aktivität im Gammafrequenzbereich führt, gefolgt von längeren Perioden ohne neuronale Aktivität. Dieses Ergebnis ermöglicht eine tiefere Untersuchung der neuronalen Konsequenzen, wenn die BHS durch die Kombination von FUS + MBs geöffnet wird. Zusätzlich unterstützt dieses Ergebnis mögliche Bedenken in Bezug auf die Sicherheit

eines solchen Ansatzes. Schlussendlich stellen wir ein kostengünstiges, automatisiertes 3D-Scansystem zur Messung von Schädel-induzierten Verzerrungen des FUS-Strahls vor. Das System hilft bei der Bestimmung des Drucks, der für die von uns entwickelten FUS-Sequenz zur Wirkstoffabgabe benötigt wird. Dieses System kann verwendet werden, um numerische Schädelmodelle schnell und zuverlässig zu validieren. Zusammenfassend erweitert diese Doktorarbeit besonders die innovativen Neurotechnologien und auch die Grundlagen der Neurowissenschaften.

Chapter 1

Introduction and Motivation

The diagnosis and treatment of psychiatric disorders is still a tremendous challenge even in the 21st century. Throughout history, patients with mental disorders have been sent to “lunatic asylums”, treated with cold water baths and demonized¹. In 1812 Benjamin Rush published his book “Medical Inquiries and Observations, Upon the Diseases of the Mind” where for the first time he recognized mental illness as disease of mind not possession by evil demons. Since then, new approaches have been used for treatment of psychiatric disorders however the main revolution in the treatment of psychiatric disorders took place between 1940s and 1950s². First, John Cade proposed the use of lithium for therapeutic intervention of psychiatric disorders³. Then the fortuitous discovery of chlorpromazine, iproniazid, and mono-amine oxidase inhibitor (MAOI) antidepressants and the follow up compounds led to a new era in the treatment of psychiatric disorders. Lithium was used for mood stabilization and bipolar disorder, anti-psychotic drugs were used for positive symptoms (e.g. hallucinations and delusions) of schizophrenia and antidepressants for mood and anxiety disorders². Despite decades of research and development, there has been no or little improvement in the efficacy of the compounds since early 1950s^{4,2}. Perhaps the major domain where psychiatric drugs showed improvement was in their safety; for example antipsychotics (i.e. first vs. second generation) and the antidepressants discovered in the 1980s are safer than the MAOIs and early tricyclic drugs as they have fewer extrapyramidal side-effects^{2,5}. It is worth mentioning that on March 2019 ketamine was approved by the Food and Drug Administration (FDA) for treatment resistant depression. Ketamine is currently available to limited number of patients and administered intranasally (as esketamine) under supervision of healthcare experts due to safety concerns⁶. Although it has rapid onset of action and holds great promise as a new treatment medication for major depression, larger clinical trials are needed for its long term effects⁷. The slow progress in the field of psychiatry continues mainly due to following issues: 1) Poor understanding of disease mechanism and thereby inadequate molecular and spatial targeting. 2) Lack of animal models and thereby insufficient validation and prediction of treatment efficacy. 3) Lack of objective biomarkers, computational models and objective strategies for measuring treatment response^{8,2,4}.

Until French physician Paul Broca's discovery of the Broca area in 1861, there was still a debate whether the brain had to be viewed from holistic perspective, an organ as whole, or with compartments specialized for different functions⁹. Twenty years after Broca's discovery, the Italian physician Angelo Mosso proposed that a cognitive task increases blood flow locally where for the first time a mental disorder was related to a physiological change in the brain¹⁰. Since then although there have been gaps due to technological limitations, animal models have helped understanding possible genetic, molecular and cellular and circuit mechanisms behind psychiatric disorders. In recent years, there have been significant advancements in understanding of addiction and obsessive-compulsive disorders in animal models^{11,12,13}. However given the complexity of human brain and major differences between frontal cortex of animals and humans, development of realistic translational animal models for most psychiatric disorders is likely impossible².

Although the findings from animal models may not translate to humans directly, an enormous amount of data suggest that the drug/pharmacological treatments of psychiatric disorders require circuit and cell type specificity. For example, specific behavioral changes have been observed when neuromodulators or their receptor agonists or antagonists were directly injected to prefrontal cortex (PFC). Interestingly having too much or too little of a given neuromodulator impaired the tasks performance which suggest that proper performance of neuronal circuits may require a tight balance of neuromodulators¹⁴. Moreover, even subtypes of receptors play different roles within same circuitry; local injections of selective antagonist D1 receptors into prefrontal cortex of primates play a selective role in the mnemonic, predictive functions^{15,16}, Dopamine D2 receptor knockdown through lentiviruses induced rapid acceleration in development of "addiction-like" reward deficits and onset of "compulsive-like" food seeking in rats¹². In addition to animal experiments, recent non-invasive imaging techniques allowed recording from human brain which revealed more insights in functional connectivity differences between distinct brain regions in Schizophrenia, Depression, autism spectrum disorders (ASD), Depression and borderline personality disorder (BPD)¹⁷. And positron emission tomography (PET) imaging showed that individuals with depression have excessive neural activity in the subgenual cingulate cortex¹⁸. Together, these data from animal and human studies suggest that psychiatric disorders arise from dysfunction of cortical and subcortical brain circuits, and cell types, receptors, and subtype of receptors within the circuit.

Despite the aforementioned advancements, existing treatment strategies still rely on systemic delivery of drugs which bind to certain receptors which are usually shared by multiple brain regions (e.g. serotonin system). Thus, current treatment modalities lack circuit specificity and this may account for the numerous side effects which they evoke.

One of the main reasons for this is the lack of safe and non-invasive methods for delivery of drugs to specific brain regions in humans. A number of non-pharmacological neuromodulation methods based on electrical, magnetic or ultrasonic stimulation have been used, however they suffer from either high invasiveness or lack of receptor specificity or low spatial resolution. In the following section, we will describe some of these neuromodulation methods and explain their advantages and limitations.

The state of the art targeted neuromodulation method is optogenetics¹⁹. Although pre-clinical optogenetics studies, helped deciphering some cells and circuit mechanisms behind anxiety, depression and addiction^{20,21}, clinical applications of optogenetics requires overcoming some major hurdles such as immune responses to viral gene delivery²², danger of opsin overexpression, phototoxicity and tissue damage due to prolonged optical stimulation²³. Moreover, all commonly used viral injection methods and optical excitation of expressed genes require invasive procedures. Although non-invasive gene delivery has been achieved by the Blood-Brain Barrier (BBB) opening with ultrasound, this requires extremely high dosage of viral injection²⁴. Furthermore, BBB opening causes inflammatory²⁵ and confounding neuromodulation effects such as inhibition and behavioral changes^{26,27,28}.

Another method is Deep Brain Stimulation (DBS), it has been successfully used in over 160.000 patients²⁹ with Parkinson's Disease (PD), Dystonia and Essential Tremor by targeting specific brain circuits. DBS has also been used in the treatment of major depression³⁰ and Obsessive Compulsive Disorders (OCD)³¹. For example DBS of Nucleus Accumbens (NAc) and lateral habenula reduced anxiety level and improved motivation, while DBS of ventro-medial prefrontal cortex (vmPFC) decreased behavioral despair and enhanced hedonic behavior in rats³². Although DBS is widely used, it is very expensive and requires surgical intervention which can cause hemorrhage and infection³³. Furthermore, the efficacy of DBS for treatment of psychiatric disorders has not been demonstrated according to evidence based medicine criteria, therefore DBS is still limited to clinical trials, not commonly used for treatment of psychiatric disorders³⁴.

Transcranial Focused Ultrasound Stimulation (tFUS) or Low Intensity Focused Ultrasound (LIFU) is an emerging technique which can non-invasively excite or suppress local neural activity with high spatial resolution³⁵. Recently it has been used to induce behavioral and physiological changes in rodents³⁶, non-human primates³⁷ and humans³⁸. However, the exact mechanism behind tFUS induced neuromodulation is not known although different theories have been suggested³⁵. Moreover, recent studies alerted the neuroscience community due to its potential confounding acoustic responses through

auditory system^{39,40,41}. Perhaps one of the main challenges is the inconsistency in the reported results, while some groups claim pulsed mode is the most effective in inducing motor responses⁴², others claim continuous wave sonication is better^{43,44}. From our own experience (unpublished), we robustly observe that the inhibition ratio in the whisker evoked responses in the vibrissae somatosensory cortex (vS1) is proportional to the number of pulses, duty cycle and pressure. However a recent study reported that short pulses with low duty cycle are more likely to induce inhibition while longer repetitive pulses are more likely to induce excitation^{35,45}. Collectively, tFUS at its current stage, needs more comprehensive studies to be considered as a reliable and robust technique for non-invasive neuromodulation of the central nervous system (CNS) circuits although it can be used for some specific applications like DBS being used for Parkinson's disease.

This thesis proposes a radically new method which mediates delivery of neuromodulator drugs to distinct brain regions non-invasively and with high spatial precision to overcome the limitation of existing methods such as systemic drug administration and other non-pharmacological techniques. The second chapter describes a Focused Ultrasound (FUS) and micro-nano particle-based method for non-invasive targeted drug delivery to brain circuits without Blood-Brain Barrier (BBB) disruption, which was the main goal of this dissertation. Firstly, micro-nano particles which are used as ultrasound sensitive drug carriers are explained, then drug carriers are characterized in an *in-vitro* setup with various ultrasound sequences. Then by performing test experiments and utilizing theoretical knowledge based on previous literature, a novel ultrasound sequence is introduced, and the sequence is tested *in-vivo* for drug (Muscimol, GABA_A agonist) release to modulate a specific cortical circuit [vibrissae sensory cortex (vS1)-vibrissae motor cortex (vM1)] in anesthetized rats. A number of *in-vivo* control experiments are performed to ensure the efficiency, specificity and safety of this novel method. The third chapter introduces an affordable and fast 3D scanning robotic system for measuring attenuation and phase aberrations induced by the skull during FUS application. The system is described, and experimental protocols are explained. The results are used for the design of ultrasound sequence and ultrasound drug carriers introduced in Chapter 2. The fourth chapter discusses the consequences of FUS and microbubbles (FUS+MBs) assisted BBB opening in anesthetized rats. Repeated transient seizures and long-term inhibition of evoked potentials are observed after BBB opening. The seizure propagation through cortical layers is analyzed. Finally, the significance the findings are speculated.

Chapter 2

Focused ultrasound mediated drug delivery through intact blood-brain barrier with millimeter precision

Parts of this chapter is “in revision” stage in “Nature Communications”.

Non-invasive, receptor-specific, millimeter-precision manipulation of brain circuits

Mehmet Sirin Ozdas^{1,†}, Aagam S. Shah^{1,†}, Paul M. Johnson^{1,†}, Nisheet Patel¹, Markus Marks¹, Tansel Baran Yasar¹, Urs Stadler³, Laurent Bigler³, Wolferger von der Behrens¹, Shashank R. Sirsi^{1,2} and Mehmet Fatih Yanik¹

¹Institute of Neuroinformatics, D-ITET, ETH Zürich, Switzerland

²Department of Bioengineering, University of Texas at Dallas, Texas 75080, USA

³Department of Chemistry, University of Zurich, Switzerland

[†]Equal Contribution

Parts of this chapter will be included in A. S. Shah’s Ph.D. dissertation as it was a joint work.

2.1 Introduction

Central nervous system (CNS) disorders arise from dysfunctions in brain networks, involving different cortical, hippocampal, amygdaloid, striatal, thalamic, and other subfields of the brain as well as different cell-types and molecular targets in these subfields^{17,46,47}. However, the most common method of treatment for CNS disorders remains systemic small molecule administration. Systemic treatments can cause significant side effects at the dosages required for efficacy by acting in other brain regions or organs/tissues^{48,49} because the receptor-binding sites targeted by drugs are almost always shared by multiple brain areas, making it extremely challenging to specifically modulate pathological networks. Current methods under development to target specific circuits such as, transcranial magnetic stimulation (TMS) or penetrating stimulation electrodes (i.e. deep-brain stimulation; DBS) either suffer from low spatial resolution, or lack of cellular and molecular specificity, or high invasiveness^{50,51}.

To address this challenge, we developed a unique combination of spatially- and molecularly- specific manipulations by focused ultrasound (FUS) and ultrasound-sensitive

drug carriers. First introduced in the 1940s⁵², FUS allows noninvasive delivery of mechanical energies deep into the tissue and even through the human skull with millimeter precision for a variety of purposes^{53,54}. FUS can also be used for neuromodulation with high or low spatial specificity (mm to cm), however, similar to TMS it lacks cellular and molecular specificity⁵³. FUS has also been combined with ultrasound-sensitive gas-filled-microbubble particles to open the blood-brain barrier (BBB) locally to deliver molecules that otherwise do not cross intact BBB, which has been studied by Hynynen, McDannold, Konofagou and colleagues⁵⁵⁻⁵⁸. This is a promising development for acute delivery of macromolecules and has significant potential in treatment of genetic disorders when used along with the pioneering FUS-mediated gene delivery approaches⁵⁹⁻⁶³. FUS technology's safety for controlled BBB opening was clinically tested by Hynynen and colleagues recently⁶⁴. While their results suggest opening BBB twice could be safe, future studies with larger populations (>5 participants), with repeated opening (>2 times), and with longer monitoring periods will provide confidence, as two patients showed signs of a microhemorrhage.

Despite considerable promise, FUS-mediated BBB opening might cause cellular damage, significant immune response, and blood cell infiltration to the brain^{65,66}, while other studies suggest that such damage depends on the choice of FUS parameters⁶⁶⁻⁷⁰. In many neurological and neuropsychiatric disorders, lifelong drug treatment is currently needed, and repeated (chronic) application of even transient and seemingly non-invasive BBB opening for delivery of drugs could have adverse consequences⁷¹. In many neurodegenerative diseases, compromise of BBB and vasculature seems to precede onset of disease⁷²⁻⁷⁵. Another significant concern is the strong effect of BBB opening on cell activity and certain behaviors in rodents and primates⁷⁶⁻⁷⁹, making its effect on circuit modulation significantly confounding. Hence, while FUS-mediated BBB opening might be acceptable for acute delivery of viral vectors or other macromolecules, it is currently unclear what long-term risks repeated BBB opening may pose for long-term treatment of neurological and neuropsychiatric disorders.

While FUS is currently used for delivery of large molecules that otherwise do not cross BBB, most clinically approved neurological and neuropsychiatric drugs are small molecules that readily cross BBB on their own. Thus, these drugs actually need to be prevented from crossing the BBB, except within the targeted brain area(s) to avoid

unacceptable off-target effects. Recently, FUS-mediated small molecule delivery has been accomplished in rodent and primate models, however, it either requires BBB opening or is highly inefficient^{57,77,80} (see Discussion). Here, we demonstrate a new approach to deliver small molecules locally with millimeter-precision, without opening BBB, by focally concentrating drugs by orders of magnitude higher with respect to systemic levels, and subsequently by uncaging them. To this end, we developed stable drug-loaded liposomes tethered to microbubbles (ultrasound-controlled drug carriers; UC-carriers) and a unique two-component aggregation-uncaging FUS (AU-FUS) sequence. We first systemically inject UC-carriers containing small-molecule drug into rats (Figure 2.1-A). These small molecule cargos can be existing FDA-approved neurological or neuropsychiatric drugs which are already capable of crossing BBB but remain in circulation while encapsulated in UC-carriers. We use ultrasound waves, to aggregate the UC-carriers (aggregation sequence, Figure 2.1-B) at desired regions in the brain. After local aggregation, we uncage drugs from the UC-carriers with a second ultrasound pulse (uncaging sequence, Figure 2.1-C), releasing these small molecules into the blood stream (Figure 2.1-D). The small molecules then cross the intact BBB within the focal area, to reach their cognate receptors.

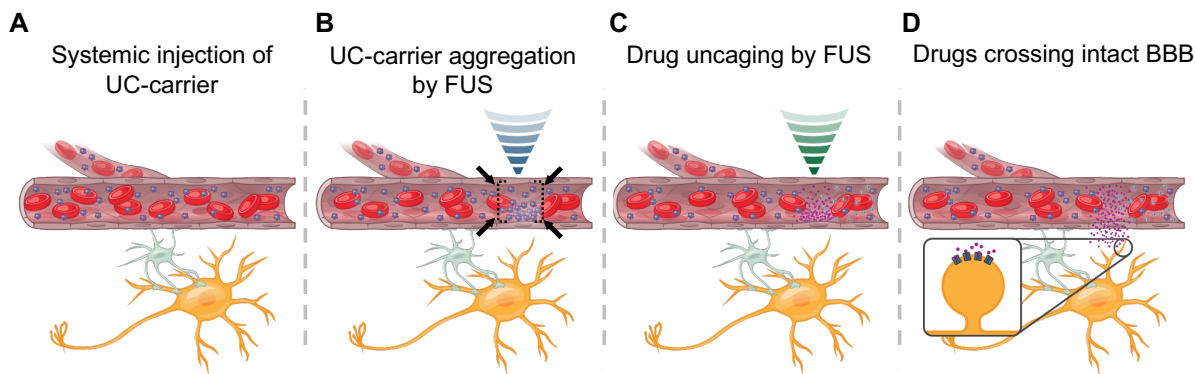


Figure 2.1 Concept of focal aggregation and uncaging of ultrasound-controlled drug carriers (UC-carriers).

(A) UC-carriers are continuously infused (blue particles within the capillary) intravenously which circulate stably.

(B) UC-carriers are first concentrated locally within the vasculature by an “aggregation” ultrasound pulse sequence (acoustic radiation force, blue).

(C) Following this, an “uncaging” ultrasound pulse sequence (acoustic fragmentation force, green) is applied for a brief duration which releases a locally concentrated amount of drug into the vasculature from the aggregated UC-carriers.

(D) Small molecules diffuse across the intact BBB reaching their cognate receptors.
(Ultrasound beam is not to scale.)

We developed and validated this novel approach by non-invasively modulating the propagation of evoked activity through a defined cortical circuit, specifically the rodent vibrissae sensory-motor pathway^{81,82}. We manipulated this circuit by focally inhibiting vibrissa sensory cortex, through ultrasound-mediated uncaging of the GABA_A receptor agonist, muscimol. We demonstrated that there is no detectable BBB opening or damage using sensitive techniques. Because UC-carriers are aggregated, our technology requires orders of magnitude lower quantity of drug to obtain a significant electrophysiological response, than required by systemic drug infusion.

2.2 Results

2.2.1 Ultrasound-controlled drug carriers, *in-vitro* characterization and optimization

We tethered drug-encapsulated liposomes to ultrasound-sensitive microbubbles (hydrophobic gas core) using thiol-maleimide chemistry (Figure 2.2-A) to create UC-carriers, modified from previous studies⁸³⁻⁸⁵ {*Aagam Shah*}. We used this configuration because tethering liposomes to microbubbles makes liposomes responsive to ultrasound, allowing better spatial control of drug deposition. The use of liposomes also allows encapsulation of diverse small molecules using either the hydrophilic liquid core or the lipophilic hydrocarbon shell of the liposomes. We prepared UC-carriers by loading either sodium fluorescein dye (model drug for *in-vitro* experiments) or muscimol (for *in-vivo* experiments) into the core of the liposomes.

To characterize the behavior of UC-carriers and to optimize FUS sequences, we built a custom *in-vitro* setup which consists of a microdialysis channel embedded in agarose^{86,87}. This channel was confocally aligned to an inverted microscope objective and FUS transducer. The entire setup was enclosed in a custom-built water tank, filled with deionized and degassed water (Figure 2.2-B, see Methods). Fluorescein-loaded UC-carriers flowed continuously through the dialysis tubing at speeds (10 μ L/min, equivalent to 5

mm/s) that mimicked the highest blood flow rates in brain capillaries⁸⁸. The carriers were then exposed to either Burst-FUS or AU-FUS sequences. We measured the model drug (fluorescein dye) release into the agarose both within the focus and out of focus of the FUS transducer.

We began with burst standard ultrasound sequences (one-component burst pulse sequence, Burst-FUS sequence) most commonly used for BBB opening, as well as two-component sequences adapted from Dr. Katherine Ferrara’s research group^{87,89,90}. In the latter case, the first component utilizes primary ultrasound radiation forces to push microbubble particles towards the edges of the capillary walls and enables greater deposition efficiency of drugs on the vascular endothelium *in-vitro*⁹¹ (albeit it would also open BBB *in-vivo*). After our first round of *in-vitro* optimizations we observed the first component of our AU-FUS sequence, a continuous wave, was able to first trap and aggregate the UC-carriers at the ultrasound focus in the capillary (Figure 2.2-C-blue, Figure 2.2-D-middle), while the second component, a fragmentation sequence (see for sequence parameters), was able to uncage the drug payload (Figure 2.2-C-green, Figure 2.2-D-right) {Nisheet Patel, Aagam Shah}. Importantly, our AU-FUS sequences not only deliver large amounts of small molecules, but also work exceptionally with several-fold lower power than both our Burst-FUS sequences and the reported fragmentation pressures of Ferrara and colleagues (Figure 2.2-E and Table 2-1). Even doubling the pressures of Burst-FUS sequences did not result in greater deposition (Figure 2.2-E), suggesting the acoustic radiation forces generated by the first component of our AU-FUS sequences are important for efficient uncaging {Aagam Shah}.

However, when tested *in-vivo* (with FUS-parameters adjusted to account for the attenuation of ultrasound waves by the skull; see section 3.3.4 in Chapter 3), even our best *in-vitro* optimized AU-FUS parameters [AU-FUS (1) and AU-FUS(2)], albeit at power levels below the inertial cavitation threshold of the UC-carriers used (a predictor of BBB opening), still caused weak BBB opening (Figure 2.3). Since neither *in-vitro* deposition nor artificial BBB models sufficiently mimic *in-vivo* BBB, capillaries, drug, and blood-plasma interactions, we further optimized our AU-FUS pulse sequence parameters by iterations between *in-vivo* and *in-vitro* experiments. We systematically varied many parameters including number of cycles, pulse-repetition frequency, amplitudes for each component of AU-FUS, pulse-to-pulse delays (FUS OFF period), UC-carrier

concentrations, and UC-carrier lipid chemistries/compositions. We finally identified a novel *in-vivo* AU-FUS sequence [AU-FUS (*in-vivo*)] that was able to deliver drugs with high efficiency to the targets which also completely avoided BBB damage (*in-vivo* experiments are discussed below in Figure 2.9 & Figure 2.10). Finally, we characterized the effects of our *in-vivo* optimized AU-FUS sequence on UC-carriers using our *in-vitro* setup. We observed that neither aggregation nor uncaging sequences alone were effective in releasing drug and that both components are required for low-pressure drug delivery (Figure 2.2-F) {*Agam Shah*}.

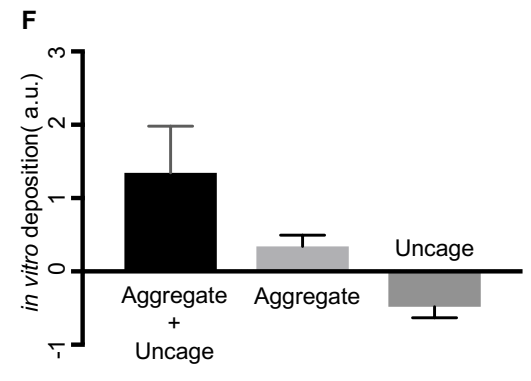
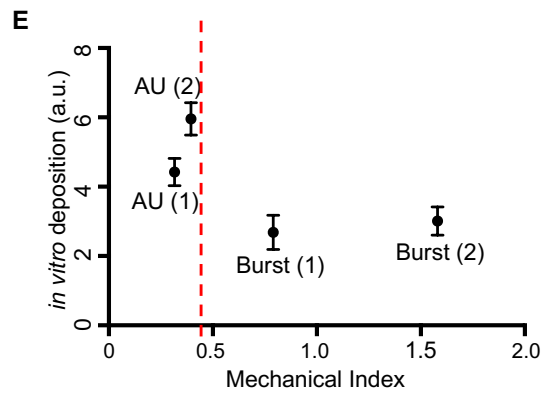
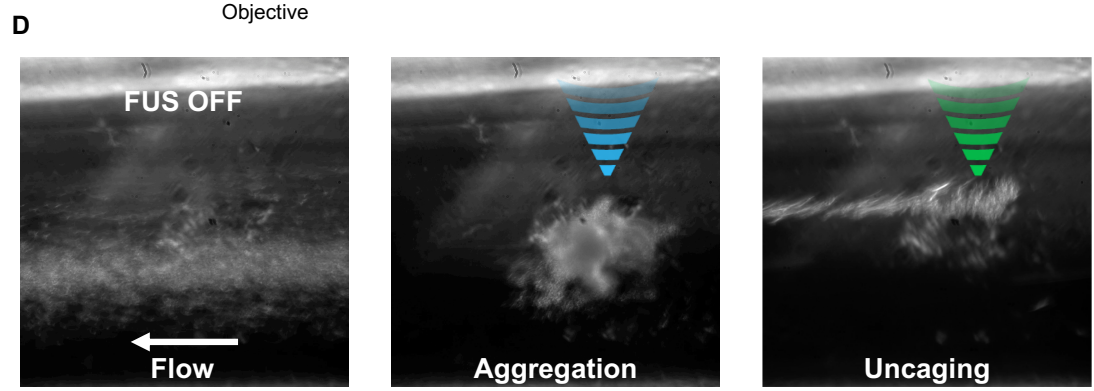
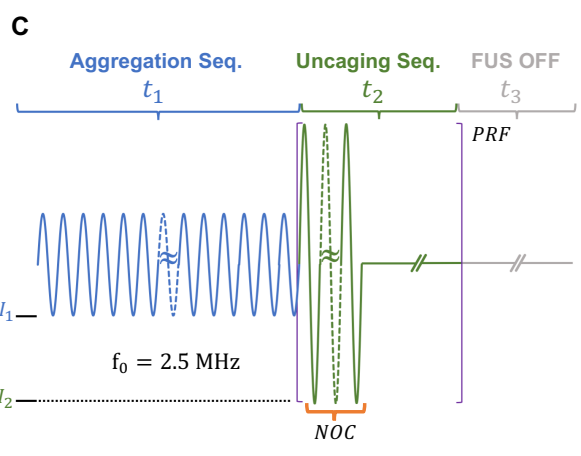
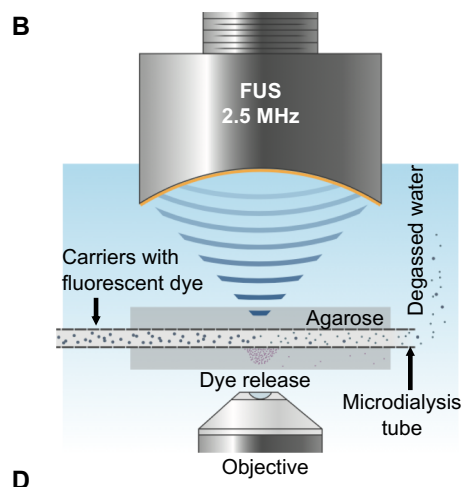
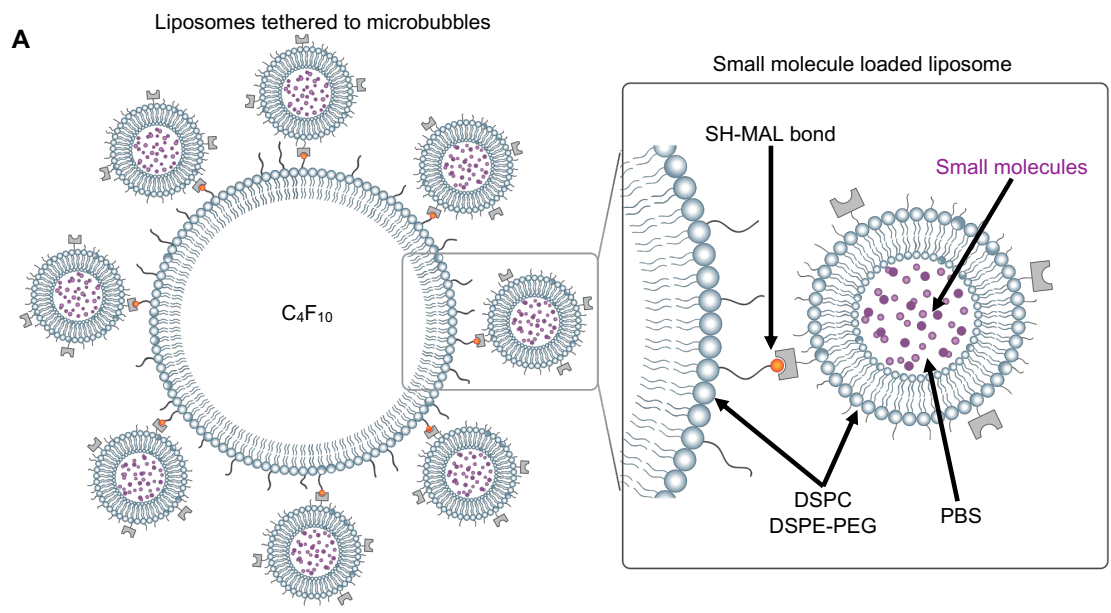


Figure 2.2 In-vitro characterization of focal aggregation and uncaging of drugs from ultrasound-controlled carriers (UC-carriers).

(A) DSPC and DSPE-PEG2k form the shells of the lipid microbubbles (monolayer) and liposomes (bilayer). The microbubbles (1.5 μm diameter) were stabilized with perfluorobutane (PFB, C_4F_{10}) gas core and had DSPE-PEG5k-Mal on the surface for conjugation with liposomes (116 nm diameter; conjugated UC-carriers had 1.7 μm diameter (Figure 2.4) which contained DSPE-PEG5k-SH on the surface, with a PBS core (illustration modified from⁹²). Small molecules were actively loaded into the liposomes using repeated freeze-thaw cycles, prior to conjugation (see Methods).

(B) The setup for *in-vitro* characterization FUS sequences consisted of dye-loaded UC-carriers flowing (single pass) through microdialysis tubing (13 kDa cut-off), embedded in low-melt agarose. This system was confocally aligned to an inverted water immersion 20x objective lens, and a 2.5 MHz FUS transducer. The entire setup was inside a custom-made water tank, filled with deionized, degassed water.

(C) The AU-FUS pulse sequence was optimized for drug delivery with mechanical indices (MI) significantly below the threshold for BBB opening (in situ $MI = 0.46$ ⁹³). First, the aggregation pulse sequence with mechanical index MI_1 and duration t_1 is applied. This is immediately followed by the uncaging pulse sequence with mechanical index MI_2 and with a fixed number of cycles (NOC) and pulse repetition frequency (PRF) for a total duration t_2 . A FUS-OFF period with duration t_3 permits reperfusion of UC-carriers within the capillary. The entire sequence is repeated for the duration of sonication.

(D) UC-carriers (white particles in the image) flow through microdialysis tubing (left) with no FUS. Aggregation (blue, middle) and uncaging (green, right) sequences UC-carriers and release drug, respectively.

(E) Deposition of drug (% total fluorescence; see Methods) using two-component AU-FUS [AU-FUS (1) (n=16), AU-FUS (2) (n=20)] and one component burst-FUS [Burst-FUS (1) (n=9), Burst-FUS (2) (n=9)]. See for parameters in Table 2-1. Red dashed line indicates inertial cavitation threshold of $MI = 0.46$. All data is represented as a box-and-whisker plot [min to max, showing all points (orange)].

(F) Deposition of drug (% total fluorescence; see Methods) using the final *in-vivo* optimized AU-FUS sequence components. The radiation and fragmentation pulses both are required for efficient drug release (see parameters in Table 2-1). All data is mean \pm s.e.m. (n=16 for aggregate + uncage, n=11 for aggregate only, n=16 for uncage only).

Condition	MI_1 [PNP]	t_1 (ms)	MI_2 [PNP]	t_2 (ms)	t_3 (ms)	PRF (Hz)	NOC
AU-FUS (1)	0.19 [0.3]	500	0.316 [0.5]	90	300	30	10000
AU-FUS (2)	0.237 [0.37]	500	0.395 [0.62]	90	300	50	10000
Burst-FUS (1)	0.79 [1.25]	-	-	-	-	1	25000
Burst-FUS (2)	1.58 [2.5]	-	-	-	-	1	25000
AU-FUS (in vivo)	0.158 [0.25]	1000	0.395 [0.62]	90	300	100	1000
LIFU	0.71 [1.12]	500	0.94 [1.5]	90	300	100	10000

Table 2-1 FUS Parameters used for *in-vivo* and *in-vitro* experiments.

MI – mechanical index, PNP – peak negative pressure in megapascal (MPa) (skull attenuation not accounted for; see section 3.3.4 in Chapter 3), t_1 – pulse duration (in milliseconds) of aggregation sequence, t_2 – duration (in milliseconds) of uncaging sequence, t_3 – duration (in milliseconds) of delay between uncaging sequence end and start of the following aggregation sequence, PRF – pulse repetition frequency in Hz, NOC – number of cycles. Skull attenuation not counted (See section 3.3.4 in Chapter 3).

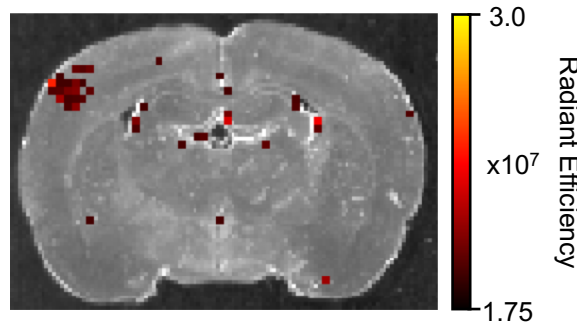


Figure 2.3 BBB Opening following sonication *in-vivo* using *in-vitro* AU-FUS (1) parameters.

IVIS spectrum imaging of Evans Blue dye extravasation following AU-FUS parameters optimized under *in-vitro* conditions. Mild but statistically significant opening is observed in vS1 in the left hemisphere where FUS sonication occurred. FUS parameters shown in [AU-FUS (1)]; MI_2 was slightly lower (0.284 vs 0.316 shown in Table 2-1). Heat map is shown as radiant efficiency (see Methods for details).

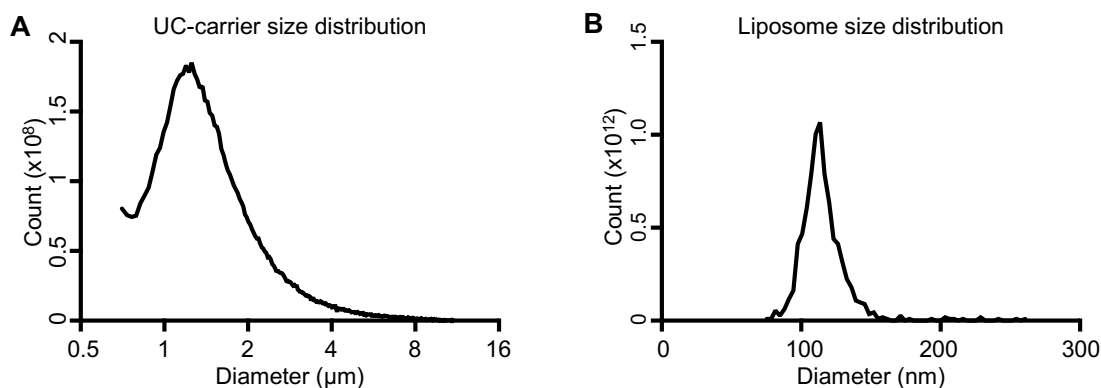


Figure 2.4 UC-carrier and liposome Size Distributions

(A) A representative example of size distribution of UC-carriers. These microbubble-liposome conjugates have a mean diameter of 1.713 μm. {Aagam Shah}

(B) A representative example of drug-loaded liposomes. The mean diameter is 116 nm. {Aagam Shah}

2.2.2 *In-vivo* modulation of a cortical circuit: vS1-vM1

We tested our AU-FUS sequence *in-vivo* [AU-FUS (*in-vivo*); see Table 2-1] by manipulating a specific cortical network without opening BBB. Rat vibrissa motor cortex (vM1) receives whisker sensory information (~80%) through projections from vibrissa sensory cortex (vS1, “Barrel cortex”)⁹⁴. When rodent whiskers are mechanically deflected, evoked activity propagates from brainstem, to thalamus, to vS1, and then to vM1. During simultaneous recordings of vS1 and vM1, we observed whisker evoked local field potentials (wEPs) following whisker deflection with a ~3.0 ms difference in peak latency (Figure 2.6-B), consistent with the spiking activity observed previously⁹⁴. We tested whether inhibiting vS1 by our technique would suppress the whisker-evoked responses in vM1 in anesthetized rats. We chose this paradigm due to multiple reasons: 1) Drug delivery without BBB disruption was key requirement of our method. 2) We wanted to use penetrating micro-electrode arrays to record both wEPs and multi-unit spikes from cortical layers in order to increase the sensitivity for drug delivery assessment, however probe insertion itself causes BBB opening⁹⁵, therefore this would create confounding effects in BBB opening assessment in the drug delivery site (vS1) [Figure 2.8]. 3) For high precision drug delivery, we chose to sonicate on a cortical circuit as targeting deeper regions would be highly affected by phase aberrations during transition from grey matter

to white matter or possible ventricles. Although these artifacts could be corrected with multi-element transducers, we were limited to a single element transducer which was designed for rat experiments. Hence, we decided to deliver drug to a well-studied brain region with sensory input capability (vS1), as evoked potentials are less sensitive to anesthesia depth and respiratory rate, and simultaneously measure the drug effect from a functionally connected but anatomically distant region (vM1) to eliminate the confounding effects due to probe insertion. 3) Moreover this circuitry has extensive scientific literature and the projections from vS1 to vM1 are extensively studied^{96,50,97} (Figure 2.5). We positioned the FUS transducer above the intact skull and focused it in vS1. Using multielectrode arrays, we measured wEPs in vM1 (Figure 2.7). In parallel, we intravenously injected muscimol-loaded UC-carriers (muscimol-UC-carriers), repeatedly aggregated and uncaged muscimol by applying our AU-FUS (*in-vivo*) sequence (Table 2-1) in vS1. Muscimol, is an agonist of ionotropic GABA_A receptors, the major receptor responsible for fast inhibitory transmission in the brain, which readily crosses the BBB⁹⁸. We showed that FUS-mediated delivery of muscimol inhibits vS1 and reduces evoked multi-unit spikes and wEPs in its projection target vM1 (Figure 2.9-A). Overall, after FUS-mediated inhibition of vS1, the amplitudes of wEPs in vM1 were strongly reduced by $56.02 \pm 3.37\%$ (“Muscimol”, black in Figure 2.9-B & Figure 2.9-C), and it took 50 mins on average to return to baseline activity. We performed several sets of control experiments in order to confirm the specificity of the approach and also verified that the combination of muscimol-UC-carriers with AU-FUS application results in local inhibition. These controls were 1) FUS application with vehicle-loaded UC-carriers (“Blank”, blue in Figure 2.9-B & Figure 2.9-C), 2) FUS application without UC-carrier injection (“FUS only”, green in Figure 2.9-B & Figure 2.9-C), 3) Systemically-injected muscimol-UC-carriers without FUS application (“Carriers only”, brown in Figure 2.9-B & Figure 2.9-C). We did not observe significant changes of the wEP responses in vM1 in any of these three control conditions (Figure 2.9-C). Furthermore, we tested the effect of systemically administered muscimol on the responses in vM1. A comparable reduction (by $57.4 \pm 0.25\%$) of responses was observable only after systemically administering at least 1300 times ($>260 \mu\text{g}$ & $<390 \mu\text{g}$) the estimated loading capacity of our UC-carriers [$\sim 200 \text{ ng}$, see Methods] (Figure 2.9-D). This is consistent with the amount of muscimol required for inactivation of brain which is at least 1.6 mg/kg ^{99–101}.

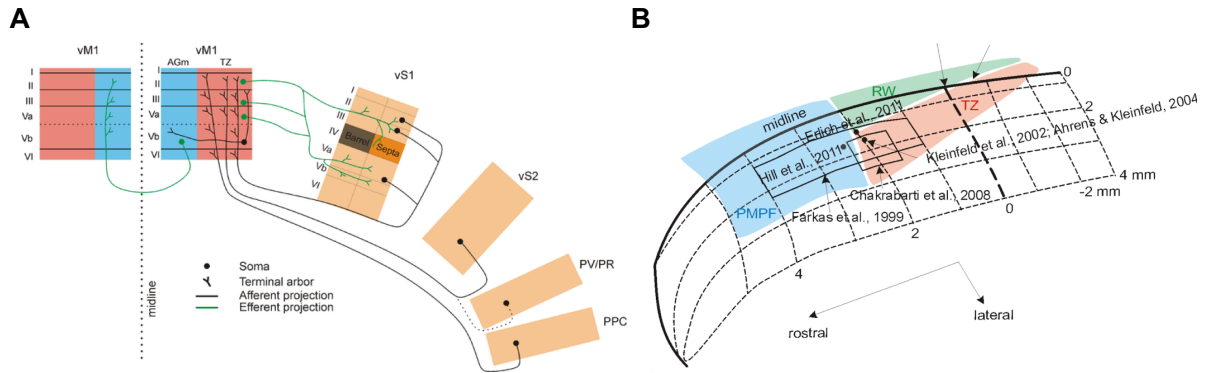


Figure 2.5 Projections from vS1 to vM1 (TZ region) and the map of TZ region on vM1 from top.

(A) The detailed laminar connectivity between vS1 and vM1 (TZ region). vS1 projections are mainly from L2/3 and L5a/b and to L2/3 and L5a in the vM1. Transitional Zone (TZ) is the region which gets direct synaptic projections from vS1 and vS2^{97,102}.

(B) The map of TZ region from the surface of cortex. See methods for coordinates.

vS1-vM1 (B) and TZ region (A) illustrations are used with permission of Chakrabarti and Schwarz¹⁰².

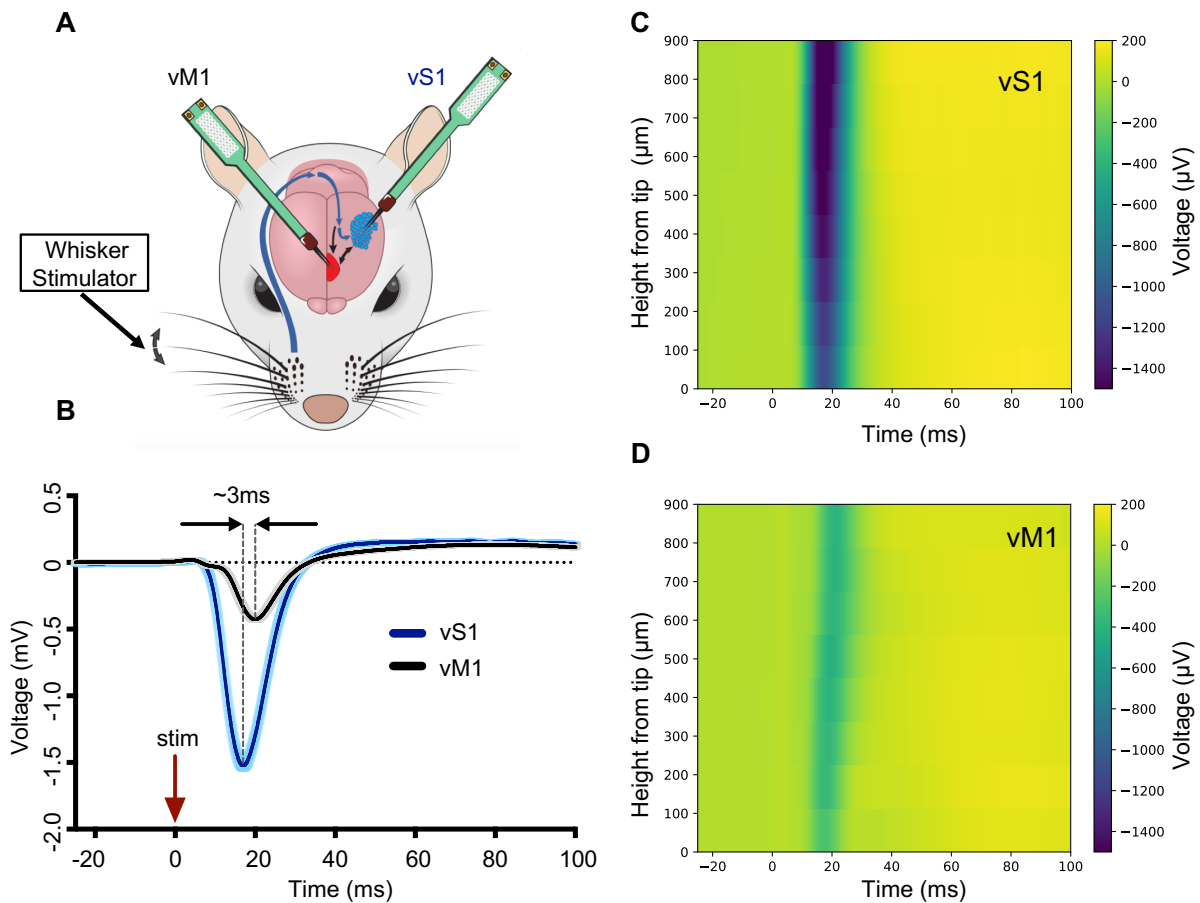


Figure 2.6 Functional and anatomical connectivity between vS1 and vM1

(A) Schematic illustration of experimental setup.

(B) The average of all wEPs (whisker deflection at 1 Hz for 8 mins, deflection at $t = 0$ ms) recorded simultaneously from vM1 (black) and vS1 (blue). Data shown is from best responding electrode in vM1 and vS1 in one animal however wEPs in vM1 can have much higher amplitudes, depending on target precision. Note ~ 3 ms difference in latency between the peaks of wEPs from vS1 and vM1, consistent with previous data⁹⁴. Data is mean \pm s.e.m.

(C) Heatmap for one shank of the probe in vS1 and, (D) one shank of the probe in vM1.

Heatmaps show the peak negative amplitude of the average of wEPs (μ V) for all 8 electrodes (100 μ m vertical spacing from tip-the most ventral electrode) in the probe shank following whisker deflection. See methods.

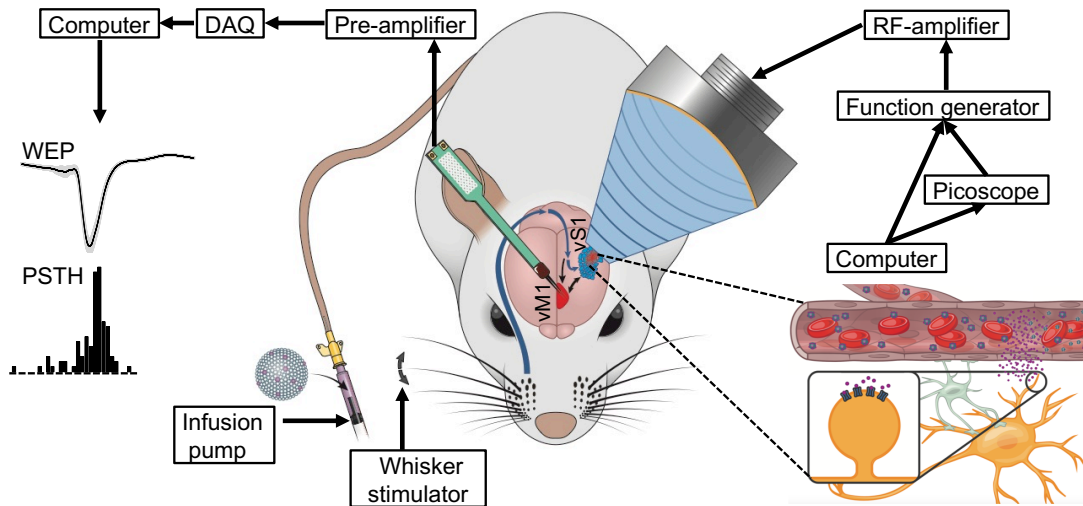


Figure 2.7 Experimental setup for *in-vivo* drug delivery in vS1-vM1 paradigm.

The animal was anesthetized, a small craniotomy was performed over vM1 (TZ region)^{82,94} for inserting recording probe, and the FUS transducer was positioned on the intact skull above vS1 with the help of stereotaxic coordinates and coupled with sterile ultrasound gel and water collimator. Whiskers were mechanically deflected at 0.3 Hz. Muscimol-UC-carriers were injected intravenously through the tail vein, the ultrasound sequence parameters are set from the computer. Upon sonication, drug is uncaged, mostly in capillaries, in focal area of the transducer. The delivery of drug is assessed by wEPs and PSTHs from vM1. See Methods for details of hardware configuration.

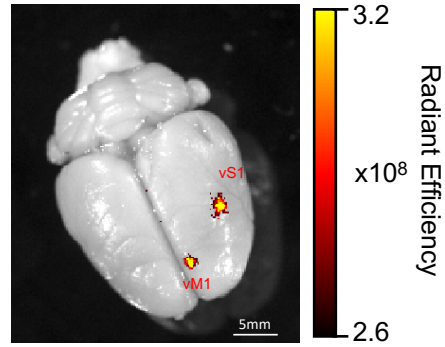


Figure 2.8 BBB opening in vS1 with FUS+MBs and BBB opening in vM1 due to probe insertion.

Burst-FUS (2), in Table 2-1, applied to vS1 following micro-bubble injection to measure the accuracy of targeting for FUS mediated drug delivery by intentional BBB opening. Micro-electrode array was inserted to vM1 and FUS was positioned on the skull such that the focal beam targets in vS1. Thirty mins post FUS application, 0.5% Evans Blue was injected then animal was perfused 1 hr post FUS. Whole brain surface was scanned with IVIS spectrum imaging, BBB opening was observed in both vS1 and vM1.

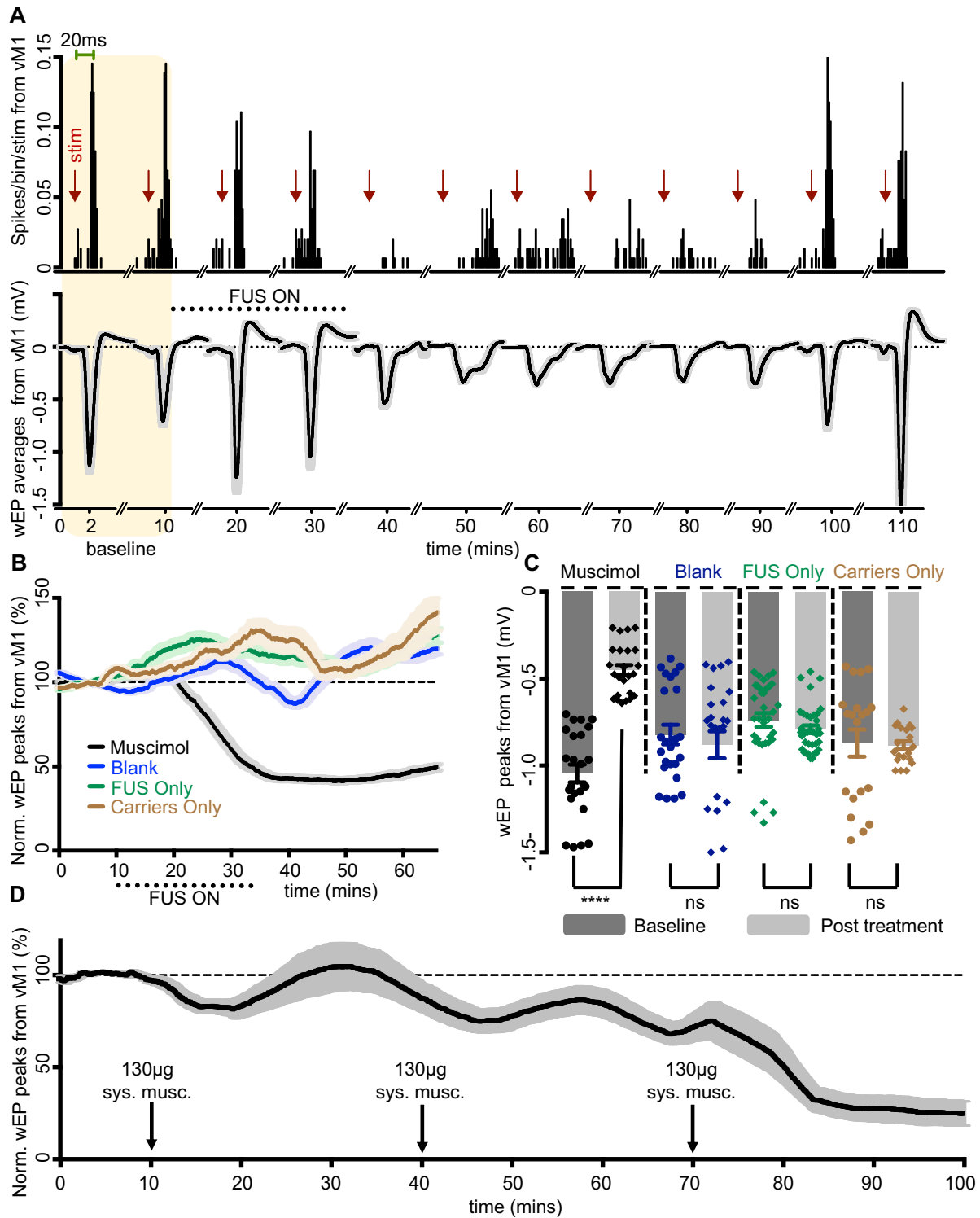


Figure 2.9 *In-vivo* receptor-specific and focal modulation of vS1-vM1 circuitry by AU-FUS sequence and UC-Carriers.

(A) Representative peri-stimulus time histogram (PSTH, top, bin size 2 ms) and wEP (bottom) responses upon focal aggregation of drug carriers (muscimol-UC-carriers) and uncaging of muscimol

from one experiment. Following 10 mins of baseline recording, the animal was injected with muscimol-UC-carriers, 30 s later FUS was turned on. We used the following parameters: $t_1 = 1000$ ms, $t_2 = 90$ ms, $MI_1 \approx 0.047$ [0.075 MPa], $t_3 = 300$ ms, $MI_2 \approx 0.118$ [0.188 MPa], $PRF = 100$ Hz, $NOC = 1000$ (MI values are estimated *in situ*, accounting for skull attenuation, See section 3.3.4 in Chapter 3). UC-carriers were injected over a period of ~ 25 mins with an infusion pump at 0.2 ml/min. FUS was turned off ~ 7 mins after the end of UC-carriers injection. wEPs were monitored online and we observed 62.62% inhibition (compared to baseline). PSTH and wEPs recovered completely ~ 75 mins after cessation of FUS. The wEP and PSTH responses were averaged over the 4 recording sites with the highest evoked responses over 2 mins window. The stimulus onset is indicated by red arrows.

(B) Time course of normalized wEP (negative peak) responses in vM1. FUS-triggered muscimol-UC-carriers delivery (“Muscimol”, $n = 6$ rats x 4 recording sites, black line), vehicle-UC-carriers were delivered with application of FUS (“Blank”, $n = 6$ rats x 4 recording sites, blue line), FUS application without UC-carrier injection [“FUS only”, $n = 9$ experiments (from 5 rats) x 4 recording sites, green line], muscimol-UC-carriers injection without FUS application (“Carriers only”, $n = 5$ rats x 4 recording sites, brown line). Evoked responses were averaged with moving window (Window Size = 180 whisker deflections). All data are mean \pm s.e.m.

(C) wEP responses (negative peak) plotted as baseline vs post-treatment. Baseline value is an average of 10 mins, and post-treatment value is an average of 30 mins (sampled randomly to match number of data points collected for baseline) following the completion of FUS application or injection of muscimol-UC-carriers. Statistical comparison was performed pairwise for baseline vs treatment (Wilcoxon matched-pairs signed rank test): “Muscimol” (black) **** $p < 0.0001$; “Blank” (blue): $p = 0.3902$; “FUS only” (green): $p = 0.2371$; “Carriers only” (brown): $p = 0.8695$. All data is mean \pm s.e.m.

(D) Time course of wEP responses (negative peak) in vM1 during systemic Muscimol (“Sys. Musc.”) injection (i.v.). Following 10 mins of baseline, 130 μ g of muscimol (~ 650 times single muscimol loaded UC-carrier injection dose) is manually injected over 1 min, every 30 mins (black arrows). Data is plotted as the moving average (Window Size = 180 whisker deflections). All data is mean \pm s.e.m. $n = 4$ rats x 4 recording sites.

2.2.3 Drug does not diffuse to off-target sites

To find further experimental evidence for drug delivery locality and that the inhibition observed in vM1 is not due to drug diffusing into electrode sites, we tested a different brain circuitry. This was not straightforward as many cortical regions are interconnected. We had to come up with a new circuitry which had the following properties: 1) The recording site should be a primary sensory area and evoked activity should be recorded as measuring spontaneous spike activity is highly sensitive to anesthesia depth and many other factors (e.g. respiration rate). 2) Drug delivery site and recording site should not be functionally connected. Thus, the local inhibition of drug delivery site should not change activity in the recording site, as this would create confounding effects. Considering these requirements, we decided to deliver drug to vS1 but measure visually evoked potentials (VEPs) from primary visual cortex (V1).

As opposed to vS1-vM1 circuitry, the functional connectivity from vS1 to V1 was less known, and there was no reported study which shows how local inhibition of vS1 affects VEPs in V1 under anesthesia. Therefore, we first aimed to inhibit vS1 locally with a different method. We used FUS at low intensity focused ultrasound (LIFU) regime where FUS sonication alone is able to induce inhibition or excitation depending on parameters and brain region^{103,104,105}. LIFU has extensive literature, however reported results have been contradicting each other^{40,106,107}. In our experience, when FUS is applied beyond a certain pressure and duration to somatosensory cortex, it induces local inhibition. LIFU can have wide range of parameters and the ratio of inhibition can increase as the duration and pressure of sonication increases¹⁰⁸ (consistent with unpublished studies of our own). We used parameters which we initially aimed for drug delivery, however this was disrupting the BBB (with MBs or UC-carriers) and also inducing local inhibition in the vM1 on its own (without MBs or UC-carriers). When we applied LIFU parameters (Table 2-1) in vS1 and recorded wEPs from vM1 (Figure 2.7), we observed significant transient inhibition (Figure 2.10-C-black). However when we recorded VEPs from V1 and applied LIFU parameters in vS1 (Figure 2.10-A), we did not observe any specific changes in the VEPs (Figure 2.10-C-purple). We therefore decided to test drug diffusion test in vS1-V1 circuitry. We positioned FUS transducer in vS1 and inserted micro-electrode array into V1 (Figure 2.10-A). After a baseline recording, we injected muscimol loaded UC-carriers through tail vein then applied AU-FUS (*in-vivo*) sequence in vS1. Although we injected even more muscimol loaded UC-Carriers and sonicated longer than we did for vS1-vM1 experiments, we did not observe any statistically significant changes in VEPs recorded from V1 (Figure 2.10-B & Figure 2.10-D, purple).

The hypothesis for the diffusion of uncaged muscimol from vS1 to vM1 can be ruled out theoretically as well. This could happen through two different means. Firstly, uncaged muscimol could perfuse through the capillaries to distant regions. Assuming the diffusion coefficient of a small molecule even in water as $D = 1.5 \times 10^{-5} \text{ cm}^2\text{s}^{-1}$, and a capillary radius of $r = 5 \text{ }\mu\text{m}$, small molecules would take $\tau = 16 \text{ ms}$ ($\tau = r^2/D$) on average to reach to the capillary wall from the anywhere in the capillary. Assuming an average blood flow speed in capillaries of $v = 1.5 \text{ mm/sec}$, we expect free muscimol to flow only $\sim 25 \text{ }\mu\text{m}$ ($\lambda = \tau \cdot v$) beyond its release site before it reaches the blood brain barrier. Even if free muscimol does not enter the brain tissue immediately and remains in the circulation, it cannot reach far away tissues before entry to veins because the maximal length of capillaries in the rat brain is only about $250 \text{ }\mu\text{m}$ ¹⁰⁹ and, drug uptake to the brain is mainly confined to the capillaries¹¹⁰. Importantly, muscimol concentration will be negligible after entering the vein and redistributing in the systemic circulation⁹⁸. Secondly, muscimol could diffuse within the interstitial space. The diffusion coefficient of muscimol in rat barrel cortex is $D = 8.7 \times 10^{-6} \text{ cm}^2\text{s}^{-1}$ ¹¹¹. Given that the maximum inhibition in vM1 occurs within 20 mins (Figure 2.9-B), muscimol can diffuse in tissue only up to $\sim 1 \text{ mm}$. This diffusion distance has been also confirmed by measuring the spread of fluorescent muscimol in the rat brain tissue¹¹². In deeper subcortical structures, the observed rostrocaudal spread of muscimol has been shown to be $\sim 1.7 \text{ mm}$ on timescales comparable to muscimol action in our work¹¹³. Since vM1 is $\sim 7 \text{ mm}$ away from vS1, muscimol diffusion in the tissue from the release site to the recording site cannot be the cause of observed neuronal inhibition. Additionally, radial diffusion of muscimol also rapidly dilutes muscimol ($\sim d^3$) with distance (d) from the delivery locus, thus making its concentration too low to cause physiological response.

Both theoretical estimations and experimental evidence showed that the uncaged drug is not likely to diffuse off-target sites at sufficient levels which can induce any physiological changes and therefore the drug delivery must likely be spatially confined to focal volume of the transducer ($\sim 1.5 \times 1.5 \times 3.5 \text{ mm}$; Figure 3.1, Chapter 3).

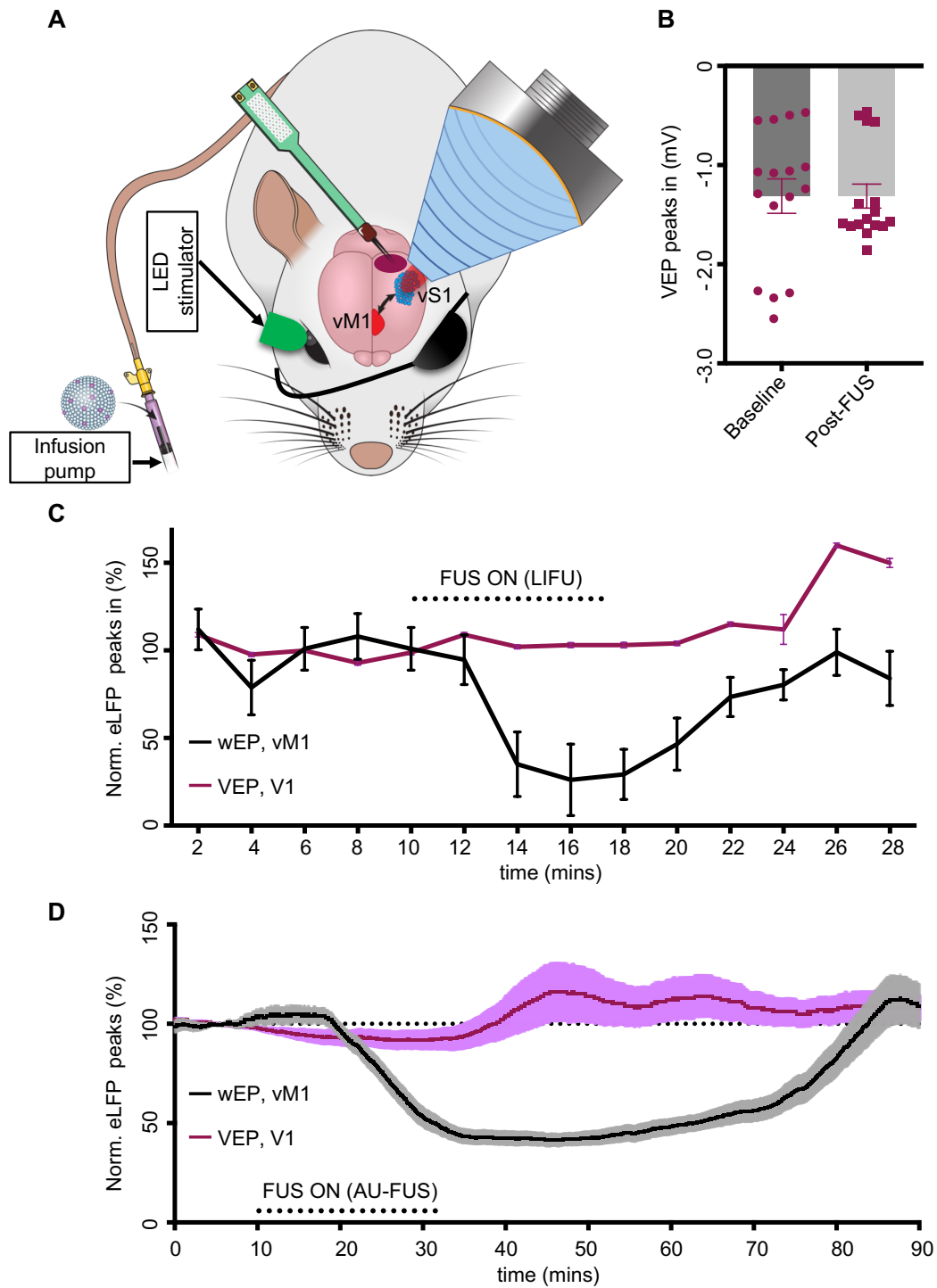


Figure 2.10 Drug doesn't diffuse to off-target sites.

(A) Experimental setup for vS1-V1 paradigm: the animal was anesthetized, a small craniotomy was performed over V1 (Coordinates: AP=-5.5-6.0 mm, ML= 3.2-3.5 mm, DV= 1.6-2.0 mm) for inserting recording probe, and the FUS transducer was positioned on the intact skull above vS1 (coordinates:

AP=-2.3 mm, ML=6.5 mm, DV=1.3 mm) with the help of stereotaxic coordinates and coupled with sterile ultrasound gel and water collimator. The contralateral eye was visually stimulated at 0.3 Hz with 10 ms TTL pulse with a 5 mm diameter green LED while ipsilateral eye was covered with a black cone. Muscimol-UC-carriers were injected through tail vein (see Methods). During whole recording session, the lights were turned off in the experiment room.

(B) LFP responses (negative peaks of VEPs) from V1 plotted as baseline vs post-treatment. Baseline value is an average of 10 mins, and post-treatment value is an average of 30 mins (sampled randomly to match number of data points collected for baseline) following the completion of FUS application or injection of muscimol-UC-carriers. Statistical comparison was performed pairwise for baseline vs treatment (Wilcoxon matched-pairs signed rank test): $p = 0.5199$, $n=4$ rats x 4 recording sites. All data is mean \pm s.e.m.

(C) Time course of normalized eLFP [negative peak] responses in vM1 (wEP) and in V1 (VEP). Following 10 mins of baseline recording, LIFU parameters applied in vS1 and eLFPs recorded from vM1 ($n = 1$ rats x 4 recording sites, black line) and V1 ($n = 1$ rats x 4 recording sites, purple line) in separate cohorts. We used the following FUS parameters for LIFU sonication: $t_1 = 500$ ms, $t_2 = 90$ ms, $MI_1 \approx 0.21$ [0.33 MPa], $t_3 = 300$ ms, $MI_2 \approx 0.28$ [0.45 MPa], PRF = 100 Hz, NOC = 10000. MI and PNP values are estimated in situ, accounting for skull attenuation (see section 3.3.4 in Chapter 3). Data is plotted as averages of 2 mins. All data are mean \pm s.e.m.

(D) Time course of normalized eLFP [negative peak] responses in vM1 (wEP) and in V1 (VEP). Following 10 mins of baseline recording, the animal was injected with muscimol-UC-carriers, 30 s later FUS was turned on. We used the following FUS parameters: $t_1 = 1000$ ms, $t_2 = 90$ ms, $MI_1 \approx 0.047$ [0.075 MPa], $t_3 = 300$ ms, $MI_2 \approx 0.118$ [0.188 MPa], PRF = 100 Hz, NOC = 1000 (see also Figure 2.2-C). MI and PNP values are estimated in situ, accounting for skull attenuation (see Section 3.3.4 in Chapter 3). UC-carriers were injected over a period of 25-30 mins with an infusion pump at 0.2 ml/min. FUS was turned off ~5 mins after the end of UC-carriers injection. wEPs were monitored online and we did not observe any statistically significant effect in V1 (B).

2.2.4 Blood-Brain Barrier integrity

We assessed BBB integrity to determine the safety of our sequence, as BBB-opening can be accompanied by inflammation and cell death. We evaluated BBB opening by measuring the extravasation of Evans Blue dye (EB) through IVIS spectrum epifluorescence imaging and Gadolinium (Gd)-enhanced T1-weighted magnetic resonance (MR) imaging, neither of which cross the intact BBB. We measured tracer (EB & Gd) extravasation in regions of interest (ROIs) ipsilateral and contralateral to FUS in vS1 to determine the BBB opening. There was no significant difference in extravasation of EB (Figure 2.11-A, Figure 2.11-B) or contrast enhancement in MR imaging (Figure 2.11-C, Figure 2.11-D) when comparing ROIs contralateral and ipsilateral to FUS sonication site for the animals undergoing AU-FUS [AU-FUS (*in-vivo*)]. In contrast, marked EB and Gd labelling demonstrated profound BBB opening with Burst-FUS parameters [Burst-FUS (2)] (Figure 2.11).

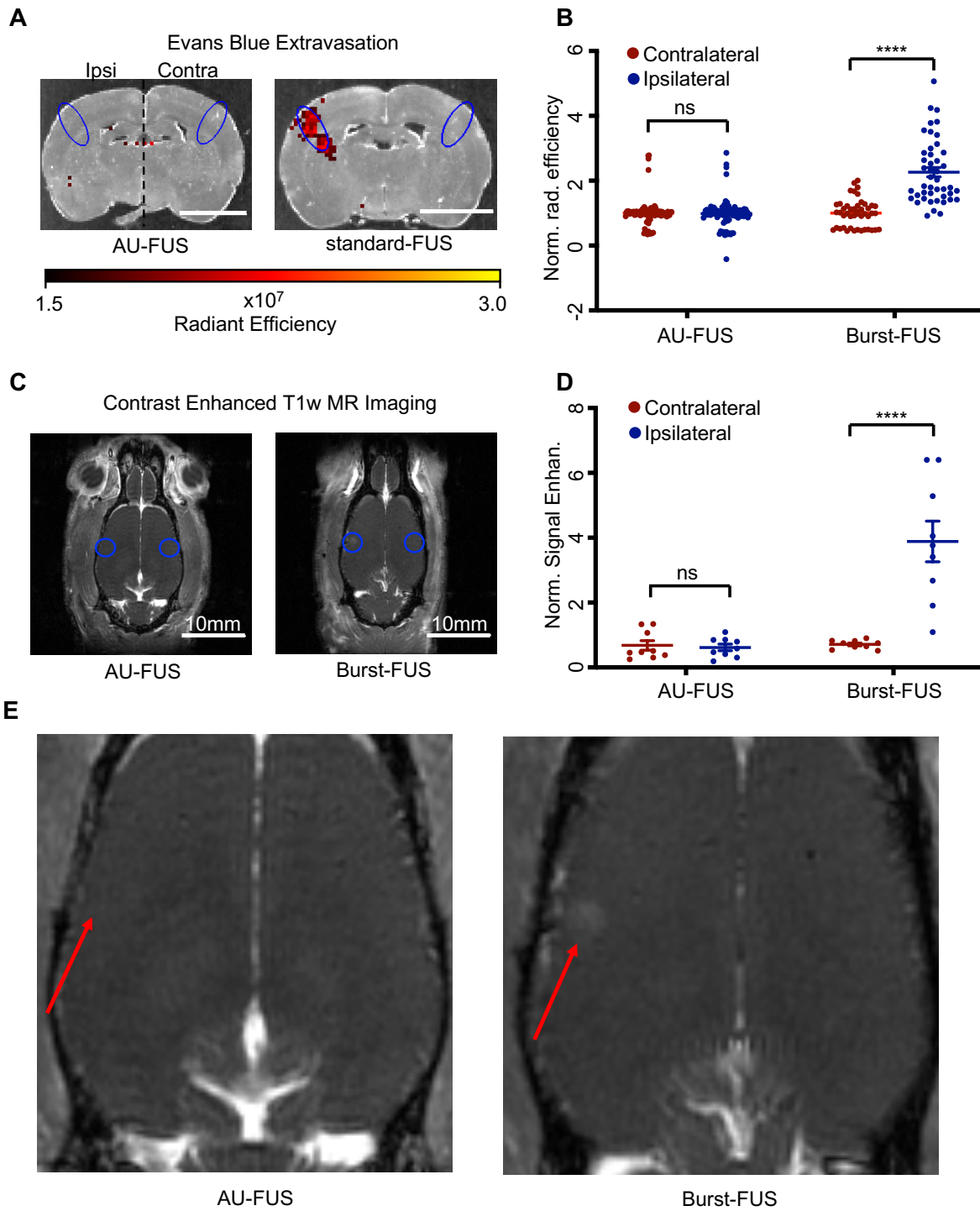


Figure 2.11 Blood-brain barrier integrity following our AU-FUS sequence and conventional Burst-FUS.

(A) Representative brain sections, imaged with IVIS spectrum, at the FUS target location of vS1 when AU-FUS (*in-vivo*) (left) was used for drug delivery as compared to Burst-FUS (2) sequence (right) for

BBB opening. ROIs (1.5 mm x 1.5 mm x 3.5 mm, blue) were measured as radiant efficiency [(photons/sec/cm²/sr) / (μW/cm²)] ipsilateral to FUS application and were compared to the contralateral vS1.

(B) Normalized radiant efficiency values within ROIs for AU-FUS and Burst-FUS sequences (n = 6 rats x 15 brain sections each for AU-FUS “Muscimol”, same rats as in Figure 2.9-B; n = 3 rats x 15 brain sections each for Burst-FUS). Pairwise Mann-Whitney rank sum test AU-FUS (Ipsilateral vs. Contralateral, p = 0.6577), Burst-FUS (Ipsilateral vs. contralateral, ****p < 0.0001)

(C) Representative brain sections, imaged with Bruker 7T MR scanner, at the FUS target location of vS1 when AU-FUS (*in-vivo*) (left) was used for drug delivery as compared to Burst-FUS (2) sequence (right) for BBB opening. ROIs (1 mm x 1 mm x 1.5 mm, blue, approximate ROI location) were measured as signal enhanced T1-weighted MR images, following Gd administration, ipsilateral to FUS application, which were compared to the contralateral vS1.

(D) Baseline-subtracted contrast enhanced T1-weighted MR image ROIs using AU-FUS and Burst-FUS sequences (n = 3 rats x 3 brain sections each for AU-FUS and Burst-FUS). Pairwise Mann-Whitney rank sum test, AU-FUS (Ipsilateral vs. Contralateral, P = 0.9494), Burst-FUS (Ipsilateral vs. contralateral, ****P < 0.0001)

(E) Zoomed images from (C). Enhanced contrast in vS1 is observed following Burst-FUS (right; red arrow) but not AU-FUS (left; red arrow).

2.3 Methods

2.3.1 Ultrasound controlled-drug carriers

We created ultrasound controlled-drug carriers (UC-carriers) as shown schematically in Figure 2.2-A. The UC-carriers contained a backbone of 1,2-distearoyl-sn-glycero-3-phosphocholine (DSPC) (Avanti Polar Lipids) and 1,2-distearoyl-sn-glycero-3-phosphoethanolamine (DSPE)-polyethylene glycol (PEG)2000 (Corden Pharma) in 90:5 molar ratio. The remaining 5% was DSPE-PEG5000-Thiol (SH) for liposomes and DSPE-PEG5000-Maleimide (MAL) (both from Nanocs) for the bubbles. The lipids were dissolved in chloroform and mixed in appropriate volumes to achieve a total concentration of 2mg/mL for the bubbles and 10mg/mL for liposomes. Chloroform was then evaporated under nitrogen and kept overnight under vacuum. The resultant lipid films were stored in -20°C till further use. For the bubbles, the lipid films were rehydrated with 1x PBS containing 10% propylene glycol and 10% glycerol. The solution was then heated at 70°C for at least 30 mins, and bath sonicated for at least 20 mins or until the solution was clear. The headspace in the vial was filled with perfluorobutane (PFB; SynQuest Laboratories), and microbubbles were formed through a probe tip sonicator (70% power; Branson SLPe with 3 mm tip). The microbubble solution was then size isolated by centrifugation at 300 x g for 3 mins, 3 times. After each centrifugation the wash solution was discarded, and the remaining bubbles were resuspended in PBS:EDTA (1 mM EDTA; pH 6.5). The liposome lipid films were rehydrated with 1x PBS, heated at 70°C for at least 30 mins, and bath sonicated for 3 hrs. Drug was added at a drug/lipid ratio of 0.3 and 15 freeze-thaw cycles were performed in liquid nitrogen and 37°C water bath, for 2.5 mins each (all steps performed in the dark for fluorescein). The liposomes yielded a mean size of ~116nm (Figure 2.4-B). The resultant bubbles and liposomes were mixed and allowed to conjugate overnight at 4°C. Next day the solution was washed 2 times by centrifugation at 300 x g for 3 mins. The concentration and size distribution were analyzed in triplicate using Multisizer 3 (Beckman Coulter). The mean size of the UC-carriers was ~1.7 μm (Figure 2.4-A).

2.3.2 Animal preparation

Female Long Evans Rats (200-300 g, Charles Rivers Laboratories, Research Models and Service, Germany) were used. The animals were housed in groups in standard Individually ventilated cages (IVC) (Allentown), and had *ad libitum* access to food and water, and were on an inverted light cycle (12 hrs dark/12 hrs light). All procedures were approved by the Veterinary Office, Canton Zürich, Switzerland.

2.3.3 Surgery

Animals were anesthetized in an induction chamber with 4-5% oxygenated isoflurane for 3-4 mins. They were then moved to a preparation area where the tail vein was catheterized with a winged 27G catheter (Terumo), and the head was shaved. 2 mg/kg Meloxicam (Metacam) and 7 mL/kg warmed Lactated Ringers solution (Fresenius Kabi, AG) were subcutaneously injected. The rat was moved to a stereotaxic frame (David Kopf), eye cream was put on both eyes and after making sure the animal is in deep anesthesia, then an incision was performed on scalp to expose skull surface. A craniotomy was performed with a micro-drill above vM1 (Coordinates AP: 0-2.5 mm and ML: 0-2 mm, with respect to bregma), and dura was carefully opened. During the craniotomy, the skull was frequently flushed with Ringers solution (B. Braun) to prevent heating. After dura removal, a piece of gel foam (Pfizer) was put on brain and Ringers solution was regularly applied to keep the brain moisturized until electrode insertion.

2.3.4 Whisker stimulation

Whiskers were cut to around 15 mm length. The 8-12 largest whiskers were inserted into a glass capillary tube which was attached to a piezo actuator (T223-H4CL-503X, Piezo Systems). The piezo actuator was shielded with a custom-made copper cover. The whiskers were deflected with 120 Hz cosine pulses (292 mm/s velocity, displaced 2.34 mm in 8 ms) which were generated in LabView (National Instruments) and converted into an analogue signal (DAC NI, USB-6211) which then drove the piezo actuator, adapted from Musall *et al.*¹¹⁴. Stimulus presentation was synchronized with the electrophysiological recordings with a TTL signal at stimulus onset. Whiskers were continuously stimulated at a repetition rate of 0.3 Hz to avoid adaptation.

2.3.5 FUS sequences

The aggregation sequence (acoustic radiation force) was a continuous wave, at a particular amplitude (MI_1 [PNP]), applied for a given duration (t_1). The uncaging sequence (acoustic fragmentation force) was an ultrasound pulse, at amplitude (MI_2 [PNP]), consisting of a fixed number of cycles (NOC) which were repeated at a given pulse repetition frequency (PRF), for a fixed duration (t_2). These sequences were combined with no delay between the aggregation and uncaging sequences, but there was a 300 ms delay between the end of uncaging sequence and start of the next aggregation sequence. See Table 2-1 for all parameters.

2.3.6 Electrophysiology and FUS drug delivery for vS1-vM1

All electrophysiological data were recorded with a RHD2000 system (Intan Technologies) with 30 kS/s sampling rate. All stereotaxic coordinates were determined with respect to bregma. A 32 channel Neuronexus probe (A2x16-10mm-100-500-177-A32, 50 μ m thick) attached to a motorized 3D arm (StereoDrive-960HD, Neurostar), fixed outside the of the stereotaxic frame, was inserted into the vM1 (Coordinates AP: 1-2 mm, ML: 0.5-1 mm, depending on the vasculature, DV: 1.5-2 mm from pia) at 50° to the coronal plane (see Figure 2.7). The probe was initially inserted 250-500 μ m below the cortical surface. The FUS transducer was integrated with an acoustic collimator which was filled with degassed and deionized water and contained a polystyrene film (McMaster-Carr) at the end. The collimator's shape was designed according to the FUS transducer's geometry so that it would not interfere with the FUS beam. This assembly was stereotaxically positioned in vS1 (Coordinates AP: -2.3 mm, ML: 6 mm, DV: 3.3 mm from skull surface) at a 30° angle with respect to the sagittal plane such that the focal volume of FUS beam targeted cortical layers of vS1. A sufficient amount of warmed sterile ultrasound gel (Parker Laboratories) was put on the skull over vS1 for acoustic coupling. After positioning the FUS transducer, the recording probe was further inserted below cortical surface to reach a final DV position of 1.5-2 mm (tip). Following this, there was a period of about 1-2 hrs during which the wEPs amplitude stabilized. Baseline wEP responses were acquired for 10 mins, followed by the intravenous injection of UC-carriers (muscimol or PBS vehicle; 2 - 2.5 x 10⁹ total UC-carriers per animal) injection intravenously with an injector (Genie Touch Syringe Pump, Kent Scientific) at a speed of 0.2 mL/min. 30 seconds after the start of injection, FUS sonication was done for 25-30 mins (period of i.v. drug delivery). Electrophysiological

data were recorded until at least 1 hr after the end of sonication to see the complete drug effect and recovery. Within half an hr of sonication, the animals receiving muscimol-UC-carriers (“Muscimol” group) were injected i.v. with 1mL of 0.5% Evans Blue (EB) dye to check for BBB integrity. EB dye was allowed to circulate for at least 30 mins before transcardial perfusion and brain excision. Isoflurane was kept around 2.5-3% during all surgical procedures. During electrophysiological recordings and drug delivery it was maintained at around 1.5-2% to keep the anesthesia minimally low throughout the experiment. The anesthesia was regularly monitored visually with breathing rate and spontaneous wEP activity.

2.3.7 Electrophysiology and FUS drug delivery for vS1-V1

The protocol used for vS1-V1 was the same as vS1-vM1 paradigm with the following exceptions: FUS sonication coordinates were changed to AP: -2.3 mm, ML: 6.5 mm, DV: 3.3 mm from skull surface and FUS angle was changed from 30° to 34°. The reason for changing the angle was to create space for electrode insertion into V1 and a more lateral region of vS1 was sonicated to achieve better coupling with skull. Electrode insertion coordinates were changed for V1 recording to AP: -5.5-6.0 mm, ML: 3.2-3.5 mm, DV: 1.6-2.0 mm to ensure that recording is done from cortical layers of V1. The angle of the recording probe insertion was kept the same as in vM1 recording. Instead of wEPs, VEPs were recorded by visual stimulation (see section 2.3.8, Visual stimulation). The amount of muscimol UC-carriers per animal was changed from 2 - 2.5 x 10⁹ to 3.0 x 10⁹ and sonication period was changed from 20-25 to 30-35 mins to show that even excessive muscimol delivery does not diffuse off-target brain circuits.

2.3.8 Visual stimulation

A thin layer of eye cream was put on the contralateral eye. A 5 mm green LED was inserted in a custom black rubber cone. The cone was positioned on the eye such that the LED illuminates on the eye 3-4 mm away from cornea. This configuration allowed high intensity light stimulation to the eye as cone covered around the eye and prevented any light source from outside except the LED light. The LED was triggered with a 10 ms TTL pulses which were generated in LabView (National Instruments) and buffered to the LED through NI-USB-6211 (National Instruments) board. Stimulus presentation was

synchronized with the electrophysiological recordings with the same TTL signal used for stimulation. The eye was continuously stimulated at a repetition rate of 0.3 Hz. The ipsilateral eye was covered with a black rubber after putting sufficient amount of eye cream. The whole recording session was done while all the lights in the room were turned off.

2.3.9 Electrophysiology and LIFU

The Procedure in “Electrophysiology and FUS Drug Delivery for vS1-vM1”, “Electrophysiology and FUS Drug Delivery for vS1-V1” were repeated except that FUS parameters were changed to LIFU parameters: $t_1 = 500$ ms, $t_2 = 90$ ms, $MI_1 \approx 0.71$ [1.12 MPa], $t_3 = 300$ ms, $MI_2 \approx 0.94$ [1.5 MPa], $PRF = 100$ Hz, $NOC = 10000$, skull attenuation not counted. Total sonication duration was kept as 7 mins and no drug or UC-carriers were administered.

2.3.10 Simultaneous vS1 and vM1 recordings

Animals were prepared for craniotomy as indicated above and stereotaxic coordinates were determined with respect to bregma. An incision was made on the scalp and craniotomies were performed on vS1 (Coordinates AP: -2.3 mm, ML: 6 mm, DV: 1.1 mm from pia) then on vM1 (Coordinates AP: 1.5 mm, ML: 1 mm, DV: 0.8 mm from pia). vS1 was covered with gel foam, and continuously supplied with Ringers solution to keep the brain fresh until the vM1 craniotomy was completed. 8-12 whiskers were inserted into a capillary tube attached to a piezo stimulator. The first probe was inserted into vS1 with a 30° angle to the sagittal plane, 5 mins later the second electrode was inserted into vM1 parallel to the sagittal plane. Neuronexus, A4x8-5mm-100-200-177 probes were used for both recordings in the experiment. Once both probes were inserted, whiskers were continuously stimulated at 1 Hz, wEPs were allowed around 2 hrs to stabilize and responses were subsequently recorded for 8 mins.

2.3.11 *In-vitro* FUS characterization

UC-carriers (5×10^8 /ml) flowed through a porous (13 kDa pore-size, 200 μ m ID) microdialysis tube (132294, Spectra/Por) which was surrounded by agarose gel (0.6% in DI water + 0.9% NaCl, 16500500, UltraPure Invitrogen) in a custom-built channel. The

custom-built channel that held the agarose gel had five marked sites, each of which was sequentially brought in the confocal alignment of a water immersion objective (CFI APO NIR 60X W, Nikon) and the FUS transducer in a water tank containing degassed and deionized water. The first four of the five sites in direction of flow were sonicated with the test FUS pulse sequences and the last site served as a control site. For either one-component or two-component sequence characterization, each site was sonicated for the same amount of time (5 mins), similar to Shortencarier *et. al*⁸⁷. The capillary was then retracted from the agarose gel and each of the five agarose-gel sites were cut out and melted in heated (80°C) deionized water, and fluorescence was measured with a plate reader (the control site was subtracted from all readings) (Gen5 Microplate Reader, BioTek).

2.3.12 Electrophysiology data analysis

All electrophysiological data analysis was done in Python, version 3.6, using custom scripts. For evoked potential analysis, the raw data was low pass filtered (3rd order Butterworth filter) at 300 Hz. The wEPs and VEPs were extracted based on the time stamp of the whisker/visual stimulus. The waveforms were then corrected for amplitude offset by taking the mean of a 25 ms time-window preceding the stimulus onset. The peak negative value for the wEP and VEP was considered to be the amplitude of the wEP and VEP response and used for analysis and data visualization. The four recording sites (i.e. electrodes) with the highest response amplitudes were then automatically selected for each experiment. Extracellular spike detection and sorting was done with Klustakwik, an open source software¹¹⁵. PSTHs were then extracted through a custom code in Python. For wEP and VEP analysis, moving averages were calculated for a window step size of 180 whisker deflections/ visual stimuli (moving step size is 1 deflection/visual stimulus). Responses were normalized for each electrode to the average response of the 10 min window preceding FUS. For statistical analysis, in order to keep the number of data points for baseline (10 mins, 152 peaks) and Post treatment (30 mins, 457 peaks) same, we randomly selected 152 peak values from Post treatment.

2.3.13 Histology and IVIS spectrum imaging

At the end of the experiment, animals were anesthetized with ketamine (100 mg/kg) and xylazine (10 mg/kg) prior to transcardial perfusion. Blood was cleared with phosphate-buffered saline (PBS) solution and animals were perfused with 4% paraformaldehyde solution (PFA; in PBS at pH 7). Brains were removed and placed in 4% PFA for at least 72-hrs before sectioning with a compresstome. Sections were cut at 100 μm thickness into a PBS bath and mounted onto microscope slides in Milli-Q water. Sections were dried in the dark and subsequently imaged using the IVIS Spectrum (Living Image). The following parameters were used: Epi-Illumination, FOV: 6.6, FSTOP: 2, Binning: (M) 8, Exposure time: 1 s, Excitation: 465 nm, Emission: 680 nm, and scales are presented as radiant efficiency. Slides were imaged from bregma -2.28 ± 0.7 mm (AP) and ROI analysis was employed using dimensions slightly larger than the theoretical FUS focal volume (3.5 mm DV x 1.5 mm ML oval angled at 30°; see Figure 3.1 in Chapter 3) at locations 6 mm (to top of ROI) from midline. Radiant efficiency values ($(\text{photons}/\text{sec}/\text{cm}^2/\text{sr}) / (\mu\text{W}/\text{cm}^2)$) for ROIs in vS1 for regions ipsilateral and contralateral to FUS were measured and values were normalized to the mean value of the contralateral side.

2.3.14 MRI imaging

Contrast enhanced T1-weighted imaging was employed to visualize BBB disruption, similar to a previous study¹¹⁶. Two groups of animals were compared (AU-FUS vs Burst-FUS, $n = 3$ each). After sonication animals were transferred into the MR scanner (Bruker 7T PharmaScan). Pre-Contrast T1-weighted images were acquired (TE / TR: 4.5 ms / 146 ms; NEX = 3; FOV: 35 mm x 35 mm; matrix = 256 x 256; slice thickness: 0.5 mm; Flip Angle = 82°). These images were repeated (post-contrast) after injecting a bolus of the MRI contrast-agent Gd-DTPA (Omniscan) at 0.3 mL/kg. Additionally, TurboRARE anatomical images were acquired as a reference (TE / TR: 24 ms / 4095 ms; NEX = 10; echo spacing factor = 8; rare factor = 8; slice thickness = 0.45 mm; matrix: 180 x 120; FOV 20 mm x 12 mm). The animals were kept at a constant anesthesia level of 2.5% and sacrificed at the end of the experiment. The signal enhancement analysis was done similar Kobus *et al.*¹¹⁷. A region of interest (ROI) (1 mm x 1 mm) was drawn around 3 adjacent post-contrast T1-weighted slices, based on the FUS reference stereotactic coordinates, while excluding ventricles from the ROI. The difference in pre- and post-sonication T1-weighted images was calculated for ipsilateral and contralateral to FUS sites. The values for each group were pooled across animals, subsequently plotted and compared.

2.3.15 Extraction of muscimol from muscimol loaded UC-carriers for LC-HR-MS/MS quantification

Muscimol loaded UC-Carriers were prepared as stated above. After overnight conjugation of the microbubbles and liposomes, the solution was centrifuged 2 times at 300 g for 3 mins. The final microbubble cake was resuspended in PBS:EDTA (1 mM EDTA; pH 6.5) and the concentration and size distribution were analyzed in triplicates using Multisizer 3 (Beckman Coulter). The total volume was also noted. 1mL of absolute ethanol was added to the UC-carriers to dissolve the lipids and uncage the muscimol, and the solution was split in two. Following this, 2.5 mL running buffer (95% acetonitrile, 5% water, 0.1% Formic acid; RB) used in LC-HR-MS/MS detection was added. The solution was then allowed to sit at either room temperature for 30 mins, or bath sonicated at 70°C. After this, 1.5 mL of the solution was centrifuged at 13300 rpm for 10 mins, and the resultant supernatant was aliquoted in triplicate (400 µL) and frozen at -80°C until LC-HR-MS/MS detection. The dilutions were noted and factored in while calculating the total amount of muscimol.

2.3.16 Quantification of muscimol with LC-HR-MS/MS

The stock solutions of muscimol (HelloBio) and internal standard (methanamine hydrochloride, Sigma-Aldrich, ISTD) were prepared in a mixture of acetonitrile/H₂O 1:1 (v/v) (ULC-MS grade, Biosolve BV) at a concentration of 200 and 100 µg/mL, respectively. The stock solutions were stored at 4°C until use. The solutions used for the quantification calibration curve were prepared as a dilution series at the concentrations of 1000, 500, 250, 50, 10, 2, and 0.5 ng/mL in acetonitrile/H₂O 1:1 (v/v) supplemented with ISTD at a final concentration of 200 ng/mL. The effective weighted values are listed in Appendix, Table 6-1. The muscimol loaded UC-carrier samples were diluted with acetonitrile/H₂O 1:1 (v/v) by a factor of 1:50. A volume of 5 µL was injected for quantification.

LC-HR-MS/MS procedure was adapted from the method developed by Gonmori et al¹¹⁸. Liquid chromatography was performed on an UltiMate 3000 UHPLC (Thermo Fisher, Waltham, MA, USA) build from a binary RS pump, an XRS open autosampler, a temperature-controllable RS column department and a diode array detector, all from the series Dionex UltiMate 3000. Compound separation was achieved at 25°C on an ACQUITY UPLC Amide Column (100 Å, 1.7 µm, 2.1 x 100 mm; Waters, Milford, MA, USA). Eluent A consisted of H₂O and eluent B was acetonitrile, both acidified with 0.1% formic acid (VWR International bvba). The following conditions were applied for elution

at a constant flow rate of 0.3 mL: (i) linear decrease starting from 90% to 50% B during 3.5 min; (ii) switch to 10% B from 3.5 to 3.7 mins (iii) holding 10% B until 7.0 min (iv) change until 7.2 mins to the starting conditions of 90% B; (v) equilibration for 2.8 mins until the next measurement run.

Mass spectrometry was conducted on a QExactive quadrupole-Orbitrap mass spectrometer (Thermo Fisher Scientific, Waltham, MA, USA) equipped with a heated ESI source operating under following conditions: needle voltage of 3.5 kV, sheath, auxiliary and sweep gas (N₂) flow rates of 30, 15 and 0 (arbitrary units), respectively. The capillary and the auxiliary gas heater temperature amounted 280°C and 250°C, respectively. The data independent MS/MS mode (DIA) in positive ionization mode was selected including an inclusion list of the precursor ion corresponding to protonated molecules of muscimol (m/z 115.05020, 62 CE [collision energy], tR = 2.25-5.00 min) and ISTD (m/z 113.07094, 20 CE, tR = 0-2.25 min). A precursor ion isolation window of 3.0 m/z and a resolution of 70'000 at full width at half maximum (FWMH) were selected together with a maximum IT of 400 ms and an AGC target of 2×10^5 . The ion chromatograms corresponding to the signals of the fragment ions of muscimol and the ISTD were extracted at m/z 98.02-98.03 and 96.04-96.05, respectively (see Appendix

Figure 6.1. Xcalibur 4.1 and QuanBrowser 4.1 (Thermo Fisher Scientific) software were employed for data acquisition, and for peak-area integration and quantitation, respectively. The recovery was estimated by first adding the standard solution containing 4.86 ng/mL muscimol in a 50x diluted sample containing 1.527 ng/mL. A spiked concentration of 6.32 ng/mL was obtained (98.6% recovery). In the second standard addition, 19.44 ng/mL were added to another sample containing 1.589 ng/mL. A spiked concentration of 22.212 ng/mL was obtained in this case (106.1% recovery).

Quantification was performed with the addition of the internal standard and the calibration curves were constructed by least-squares linear regression analysis. Thereby, peak area ratios of the signals from the analyte and the internal standard were plotted against the concentration of the analyte. The set of calibrators at 0.5, 2, 10, 50, 250, 500, and 1000 ng/mL concentration were measured to determine the dynamic range and the linearity of the quantification method. The quadratic fitting and the weighting function of $1/X^2$ were selected and correlation coefficient values $R^2 > 0.999$ was obtained (see Appendix Figure 6.2). A deviation below 5% was obtained by comparing the weighted and the measured concentrations (see Appendix Table 6-2).

2.3.17 Statistical analysis

Non-parametric statistical tests (pairwise Mann-Whitney rank sum test, or Wilcoxon matched-pairs signed rank test) were performed for electrophysiological data and imaging data. All statistical analysis was performed using GraphPad Prism version 7.0.0 for MacBook, GraphPad Software, San Diego, California USA.

2.4 Discussion

Technological advancements that enable safe and robust manipulation of specific neural circuits involved in disease pathology can address both efficacy and molecular specificity challenges of existing treatments. In this paper, we successfully demonstrate a novel technique that allows efficacious and non-invasive modulation of specific brain circuits by using the receptor-specificity of small molecules and spatially targeted delivery. We overcame several fundamental challenges to make this possible: 1) Devising a means to trap and concentrate sufficiently high numbers of UC-carriers in circulation, 2) Uncaging ample amounts of drug that induce physiological response with minimal ultrasound energies, 3) Avoiding opening/damaging BBB, 4) Producing stable enough microbubble-liposome complexes suitable for use with two-component FUS which can carry large payloads with diverse physical properties (in contrast to drug-loaded microbubbles alone¹¹⁹⁻¹²²), and 5) Identifying FUS sequences that do not cause nonspecific neuronal responses (i.e. without molecular specificity) due to FUS alone (i.e. in the absence of UC-carriers).

Interestingly, our AU-FUS two-component sequences seem to concentrate the drug carriers not only along the radial axis of the capillaries (primary radiation forces), but also along the longitudinal axis of the capillaries (secondary radiation forces). The aggregation component of our AU-FUS sequence utilizes secondary radiation forces, known as “Bjerknes forces”, to drive bubbles into close proximity to each other at low-amplitudes of pressure^{123,124}. The dynamics of aggregated bubbles in a cluster are complex as they continue to volumetrically oscillate, coalesce, break up, and re-form repeatedly under continuous low-intensity ultrasound¹²⁵. While this physical response of microbubbles could lead to enhanced drug delivery (as liposomes may be de-stabilized in

this process), the exact mechanisms responsible for facilitating drug release from conjugated liposomes are difficult to elucidate due to the complex nature of microbubble aggregation, which is highly dependent on microbubble sizes, concentration, ultrasound frequency, and pressure. Additionally, the application of the higher intensity fragmentation pulse in the second part of AU-FUS sequence, as the microbubble shells destabilize, may promote better drug release from liposomes in microbubble clusters compared to individual bubbles, as gas from the bubbles would leak out at high velocities, as suggested by Klivanov *et al.*¹²⁶, causing shear effects on liposomal bilayer, thereby releasing its contents, as shown by Marmottant *et al.*¹²⁷.

The vS1-vM1 circuit is a good model for *in-vivo* validation of FUS-mediated delivery of drugs. First, the functional and anatomical connectivity between vS1-vM1 is well described^{81,128}. This enabled us to demonstrate the spatial specificity of FUS application, and receptor specificity of drug loaded UC-carriers. Second, multiple studies demonstrate that inhibiting vS1, results in the attenuation of evoked responses in vM1 as well^{94,129}.

A major challenge in the chronic use of ultrasound-mediated drug release is that previous approaches either required or caused unavoidable BBB opening^{57,77}. More recently, it has been shown that BBB opening can induce sterile inflammation⁶⁵ under certain conditions, has strong effects on cell activity and behavior⁷⁶⁻⁷⁹, and is implicated in neurodegenerative diseases as well⁷¹⁻⁷⁵. It is therefore vital to achieve FUS-mediated drug release without compromising the BBB, especially for use in chronic treatments of many brain disorders. We use multiple measures to demonstrate BBB integrity: Evans Blue dye and Gadolinium extravasation through IVIS spectrum and MR imaging, respectively. Both Evans Blue dye and Gadolinium do not cross the intact BBB, remaining in circulation, and are considered sensitive and reliable measures of BBB integrity¹³⁰.

Recent studies by Airan and colleagues^{131,132} suggest that FUS-sensitive PFP nanoemulsions (instead of the microbubbles with liposomes used here) might be used to deliver compounds to the brain without opening BBB. While potentially interesting, their method requires extremely large amounts of encapsulated drug to be injected to observe effects (nanoemulsions needed to be injected at 1 mg/kg propofol to show similar effects to the systemic injection of only 2 mg/kg Propofol). As the local propofol concentration required for inhibition is miniscule (tens of nanograms¹³³), this suggests that most of the

propofol content of the nanoemulsions could be released nonspecifically to the rest of the body, which is indeed a large quantity. Since our UC-carriers need to be loaded with at least 1300 times less drug than that required through systemic delivery to yield significant effects, even if their content were completely released systemically, there would be little or no side effects (Figure 2.9). Interestingly, their method of FUS-mediated drug delivery and inhibition shows extremely transient effects (that lasts 8-14 secs), reminiscent of the transient effects observed with FUS alone (without any nanoparticles)¹³⁴. Another future challenge in the use of nanoemulsions is that unlike the gas-filled microbubbles we engineered, they cannot be spatially concentrated due to their significantly lower responsiveness to acoustic radiation forces, making further improvements in their efficacy and specificity unlikely.

Our *in-vitro* studies were performed using commercially available microdialysis tubing, which is larger than the diameter of brain capillaries. Due to the large size of ultrasound transducers and the optical objective lenses, it is currently infeasible to image our microparticles in brain capillaries during the application of ultrasound. However, our *in-vivo* results are completely consistent with our *in-vitro* results, and our sequences are optimized *in-vivo*.

While our mechanistic understanding of psychiatric and neurological disease pathologies has significantly advanced in the preceding decades, there has been little translation of our knowledge to viable treatments. This has been in part due to the vast complexity and heterogeneity of the brain and an inability to selectively target regions and circuits of interest. Circuit-selective neuromodulation in humans may offer a more realistic path towards effectively treating CNS disorders. Moreover, targeted delivery may offer a new avenue for small molecules that have failed due to toxicity or lack of efficacy, by allowing drugs to be delivered only to a desired region and possibly at higher concentrations than achievable through systemic delivery. Approved drugs should also benefit from focal delivery as it can likely eliminate, many if not all, side effects.

Existing clinical ultrasound systems for targeting brain are expensive and bulky, which would make chronic treatments challenging. However, they can be significantly scaled down with the use of integrated MEMS ultrasound transducers^{83,84}, which are capable of generating sufficient ultrasound power and can also be chronically implanted under the scalp or in the skull. Use of such technologies beneath the skull can also allow the use of

higher frequency ultrasound waves (e.g. 2.5 MHz) with higher spatial resolution in clinical applications. The other option would be to use drugs with long lasting effects such as the NMDAR antagonist ketamine (recently approved as a rapid-onset antidepressant for patients with treatment resistant depression) which is efficacious for weeks following acute administration¹³⁷. Targeted delivery of ketamine could reduce its side-effects (such as psychotomimetic and perceptual disturbances, in addition to heart rate and blood pressure complications¹³⁸), while enhancing its therapeutic index. While further refinement of our technology can advance it to the clinic, our approach has a viable path forward, as individual chemical and ultrasound components of our technology are already FDA approved. Regardless, the technology we present enables the most efficacious form of non-invasive, receptor-specific, millimeter-precise manipulation of brain circuits which is safe.

Chapter 3

Parts of this chapter are from the following manuscript in preparation.

“Automated 3D-scanning system for fast characterization of transcranial focused ultrasound fields in rodent skull”

Mehmet Sirin Ozdas¹, Hazael Montanaro², Paul M. Johnson¹, Aagam S. Shah¹, Esra Neufeld², Niels Kuster² and Mehmet Fatih Yanik¹

¹Institute of Neuroinformatics, D-ITET, ETH Zürich, Switzerland

²IT’IS Foundation, ETH Zurich, Switzerland

Automated 3D-scanning system for fast characterization of transcranial focused ultrasound fields in rodent skull

3.1 Introduction

Focused Ultrasound (FUS) is becoming an increasingly common tool for therapeutic intervention of various brain disorders in many different modalities¹³⁹. It has been extensively studied for disrupting the Blood-Brain Barrier (BBB) in distinct brain regions^{140,141} when combined with microbubbles (FUS+MB). It has been used for the delivery of both large and small molecules ranging from adeno-associative viruses¹⁴², anticancer compounds¹⁴³ to neuromodulators¹⁴⁴ to the brain which normally cannot reach the extra-cellular space. FUS has also been used to induce tissue necrosis in deep brain regions in a highly focused manner without instigating adverse effects in surrounding tissue when applied at high intensity (HIFU)¹⁴⁵. It has been used for ablation of intracranial tumors¹⁴⁶, treatment of essential tremors¹⁴⁷ and chronic neuropathic pain¹⁴⁸. FUS can also be used at Low Intensity mode (LIFU) to excite or inhibit, depending on target site and sonication parameters, neuronal activity in brain without tissue damage¹⁰³. In this regime FUS does not induce thermal effects, the neuromodulation is believed to be induced by activating ion channels¹⁴⁹. However the exact mechanism is not well understood and contradicting studies have been reported¹⁵⁰. No matter in what modality FUS is used, the precision of sonication area in brain and thereby the success of the therapy is severely limited by the skull due to its physical properties such as variable thickness, high acoustic impedance in comparison with brain, heterogeneity, high ultrasound absorption and inter subject variability¹⁵¹. Successful therapies must therefore compensate for these skull related effects.

Multi-element transducers have been proposed to correct skull induced artifacts^{152,153}. Although this approach brings improved clinical outcomes for certain applications¹⁴⁷, it requires bulky and highly expensive electronic components as well as MRI guidance for target determination¹⁵⁴, which makes it inaccessible for many patients in need. Another approach has been proposed based on chirp-coded ultrasonic excitation¹⁵⁵. Although this method is effective for reducing energy concentration in standing waves and side lobes, it does not help for correcting the phase aberrations or deformations in the main focal beam¹⁵¹. More recently, 3D-printed acoustic lenses and holograms have been proposed to correct skull induced artifacts with single element transducers^{156,157}. This approach is very promising, and manufacturing of these lenses does not have major limitations due to advanced printing technologies. However, the bottleneck of this approach is the requirement of a successful numerical skull model¹⁵¹ which may be improved by validation with an experimental platform. We believe that 3D scanning of transcranial FUS beam profiles may provide further insights for understanding how physical properties of the skull affect FUS beam and help validate numerical models on *ex-vivo* real skulls in a fast, affordable and reliable manner.

We present a fast and affordable 3D scanning system for analyzing rodent skull effect. We show detailed methodology for degassing skulls and measuring skull attenuation. Finally, we show 3D pressure distribution fields in water with and without the skull. The experimental results in this chapter were used to determine FUS intensity parameters for AU-FUS (*in-vivo*) or Burst (BBB opening) sequences discussed in Chapter 2 and Chapter 4.

3.2 Results

3.2.1 Scanning FUS beam with and without skull *ex-vivo*.

To visualize how the skull attenuates and aberrates the focal beam of the FUS transducer for a given target, we scanned the pressure distribution of the FUS transducer (see Methods) in a water chamber with and without a rat skull (Figure 3.1). In the case with the rat skull, we observed secondary side lobes along with the main focal beam. We found out that the rat skull causes a 65% attenuation at the peak focal point with respect to the peak in just water for the given sonication target (4 mm posterior to bregma, 7 mm ventral) below the skull. Moreover, we observed that the skull shifted the focal point towards dorsal direction by 0.57 mm while the shift in medio-lateral and anterior-posterior axis were much smaller (0.14 and 0.015 mm). As expected, the shift and the attenuation ratio depended on the sonication area (skull thickness and geometry). When we sonicated more anterior regions below the skull (7 mm below the bregma), the dorsal shift changed by up to 1 mm.

To demonstrate how our *ex-vivo* skull scans can help validate the exposure predictions (targeting accuracy, attenuation, shift in the peak location and shape of FUS beam, secondary foci), we scanned the whole skull with micro-computerized tomography (μ CT) from which a detailed skull model was reconstructed complete with CT based heterogeneous acoustic properties. We then applied simulation algorithms developed by the IT'IS Foundation as part of the Sim4Life computational life sciences platform (ZMT Zurich MedTech, Zurich, Switzerland) [Figure 3.2].

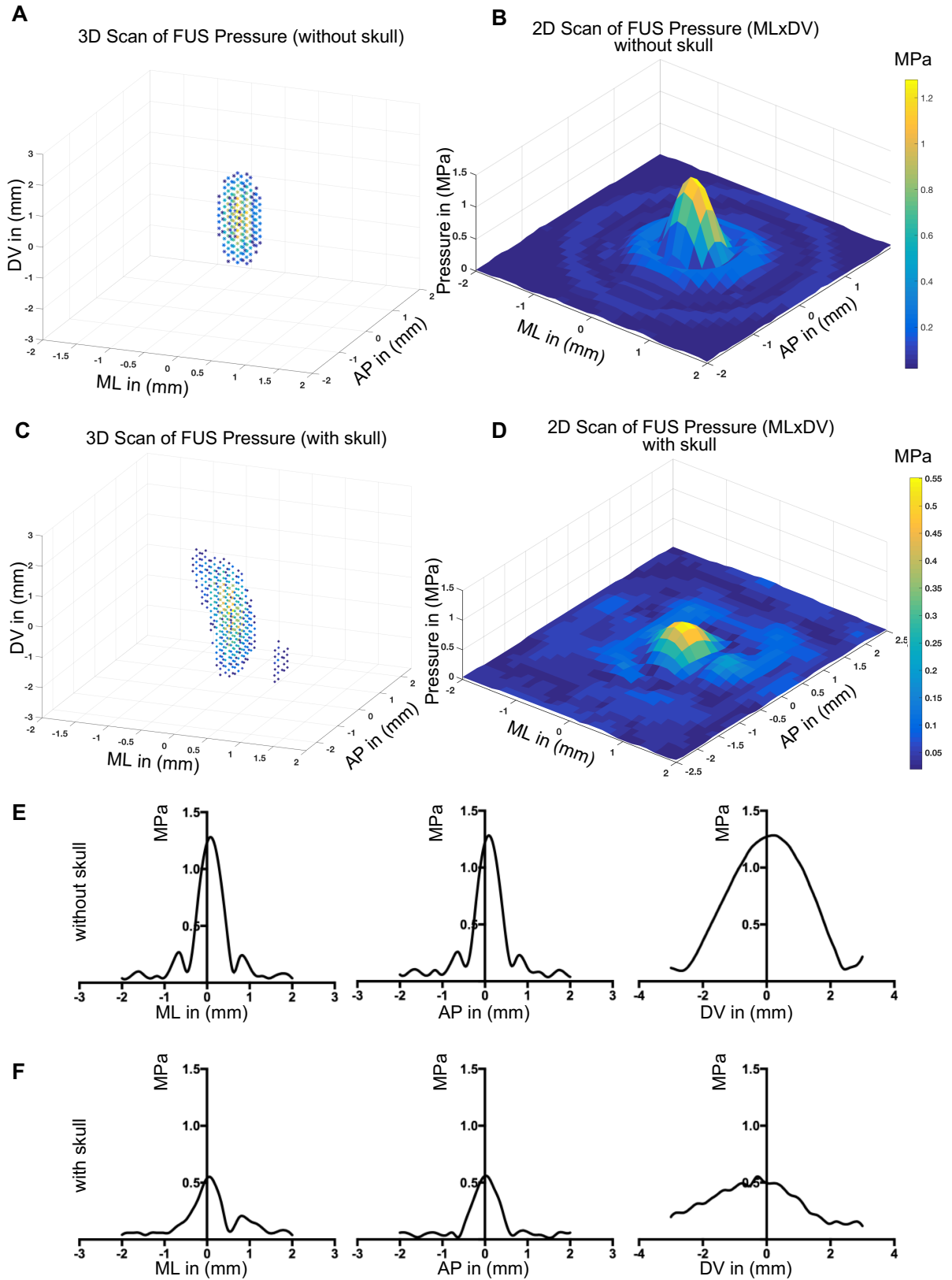


Figure 3.1 3D, 2D and 1D Scan of FUS intensity with and without skull.

The skull is extracted from a rat, degassed and attached on the manual 3D system as shown in Figure 3.3A metal pointer (Figure 3.4-A) was attached on the stereotaxic arm and used to point to the bregma on the skull and set as reference. The metal pointer was then replaced with the FUS transducer which was attached to a custom adapter such that the focal point of the FUS transducer precisely matches with the tip of the metal pointer. The stereotaxic arm was positioned to AP=-4 mm, DV=7 mm, ML=0 mm in reference to bregma. The hydrophone was positioned below the skull and controlled with a motorized 3D system to find the focal point of the transducer. For both with and without skull scans the hydrophone was repositioned to find the focal point as the skull changed the coordinates of focal point. Intensity profile of FUS transducer at the focal plane (AP-ML) (B) without skull and (D) and with skull. Intensity profiles of FUS transducer at three directions (ML, AP, DV) (E) without skull and (F) and with skull. 3D visualization of the focal volume of FUS pressure intensity (A) without skull and (C) and with skull.

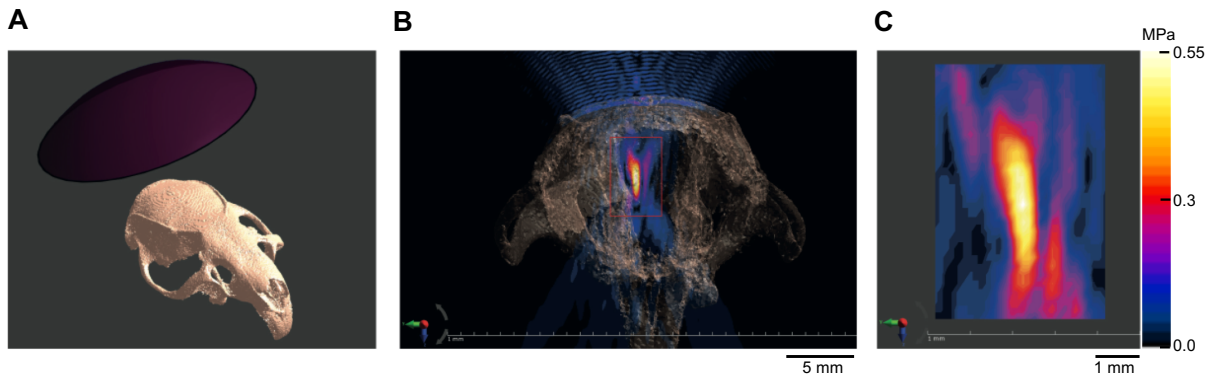


Figure 3.2 Validation of a numerical model with experimental data collected with our method.

- (A) Experimental setup, single element curved focused transducer positioned orthogonal to the skull surface, generated and discretized according to micro CT data.
- (B) Simulated pressure wave distribution in slice containing maximum through skull model.
- (C) Experimental pressure distribution in slice corresponding to area delineated in (B).

3.3 Methods

3.3.1 Experimental setup and FUS pressure distribution measurement protocol

The skull was extracted from a deceased female Lewis rat weighing 200 g (Charles River Laboratories). Tissue was removed from the surface of the skull, then the skull was placed in a vacuum chamber filled by half with degassed Milli-Q water for 60 mins to remove any trapped air inside the skull (Figure 3.5-B). The degassed skull was then positioned inside a degassed Milli-Q water chamber and controlled manually by mounting on a 3D system (PT3/M, Thorlabs) [Figure 3.4-C]. The water chamber was at the base of a stereotaxic system (Neurostar). A metal pointer¹⁵⁸ was mounted on the motorized arm of the stereotaxic system to find the bregma (Figure 3.4-A). The FUS transducer subsequently replaced the metal pointer on the stereotaxic arm such that the focal point matched precisely with the tip of the metal pointer (Figure 3.4-B). The FUS transducer was then positioned such that the focus of the ultrasound was aligned at 4 mm rostral to the bregma and 7 mm ventral from the skull surface. A needle hydrophone (9 μm thick gold electrode PVDF film; 0.2 mm tip size, Precision Acoustics) was mounted on a motorized system (PT3/M-Z8), and then moved to find the focal point of the transducer (Figure 3.4-C). The hydrophone scanned a volume of 4 mm x 6 mm x 5 mm in 3D with the skull and 4 mm x 6 mm x 4 mm without it. Since the presence of the skull extended focal area in the DV axis, DV scan range was higher than ML and AP. The scanning volume is manually determined based on maximum distance that the hydrophone can move under the skull surface without touching the skull. Once the scanning volume is determined, the optical distance sensor is calibrated (See Calibration of optical distance sensor), then the automated 3D scanning is initiated. The motors were moved with 100 μm step sizes to scan the AP and DV axes, and ML axis moved continuously to decrease time required for scanning, while data was collected with 14 μm resolution. ML values were then sampled every 100 μm . An optical displacement sensor (SICK, OD Mini) was used to find the position of the ML motor, and an analogue-to-digital-converter (ADC) (NI 6009) was used to gather sensor data to the computer. Hydrophone pressure readings were collected with a PicoScope (3205B), and the entire setup was controlled with a custom MATLAB script (Figure 3.3). The whole volume of 4 mm x 6 mm x 5 mm was

scanned in around 2.5 hrs. This would take around 33 hrs if all the motors were moved at 100 μm steps as each step was completed in around one second.

3.3.2 Calibration of optical distance sensor

Once the scanning volume was determined, the optical distance sensor was calibrated for the ML axis. The transducer was first positioned to the focal point. If scanning length for ML was determined as 4 mm, the distance sensor was set to 0 Volt at 0 mm (the right most side) and 10 Volts at 4 mm (the left most side) at the focal plane. A graphical user interface (GUI) was developed to guide the user step by step. The whole calibration procedure takes around 4-5 mins. The calibration output, which shows voltage value per distance, is saved in a text file then used for data analysis and visualization.

3.3.3 FUS setup and transducer calibration

A custom-made transducer (Sonic Concepts) with 2.5 MHz center frequency, 40 mm diameter, 30 mm working distance/20.65 mm focal depth, and 0.5 x 0.5 x 2.5 mm theoretical focus was used, along with a custom impedance matching network for the transducer (Sonic Concepts). Calibration was done in a degassed and deionized water filled chamber with a 0.2 mm needle hydrophone (Acoustic Precision). The ultrasound pulses were generated with a function generator (Agilent 33210A, Keysight technologies) and PicoScope (3205B) and controlled by a custom MATLAB script. The signal was amplified by 50 dB through a power amplifier (E&I 325LA). The pulses generated by the function generator can be in burst mode (e.g. 4 Cycles, with 100Hz PRF) or continuous mode. We excited the FUS transducer with a continuous mode sinusoidal signal and at 1MPa peak negative pressure (PNP).

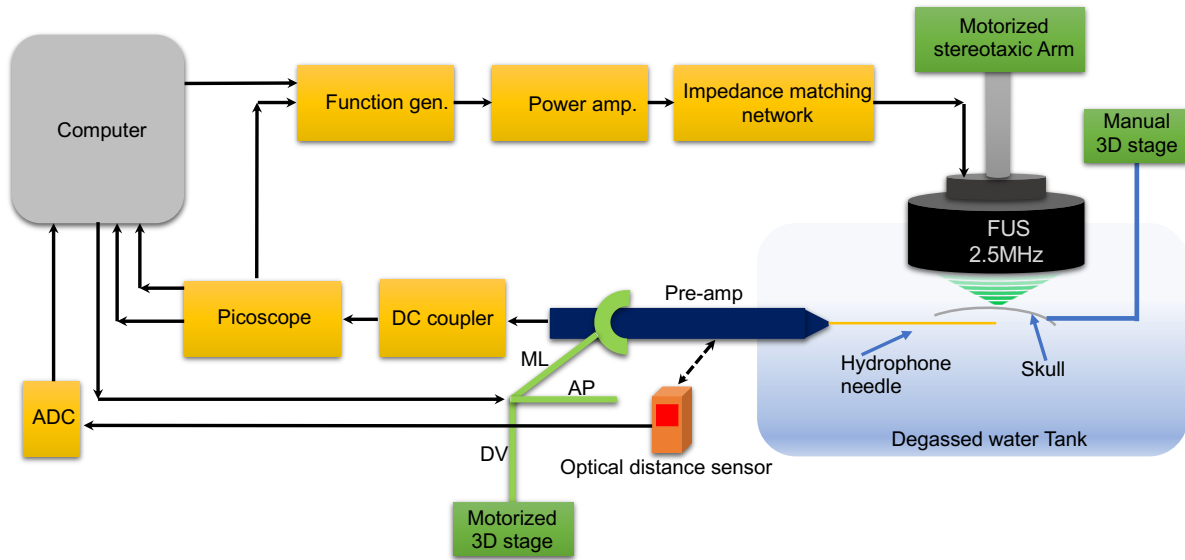


Figure 3.3 Schematic for automated pressure mapping system of skull effects on FUS.

Schematic illustration of automated hydrophone scan to determine pressure changes caused by rat skull. See Methods for description.

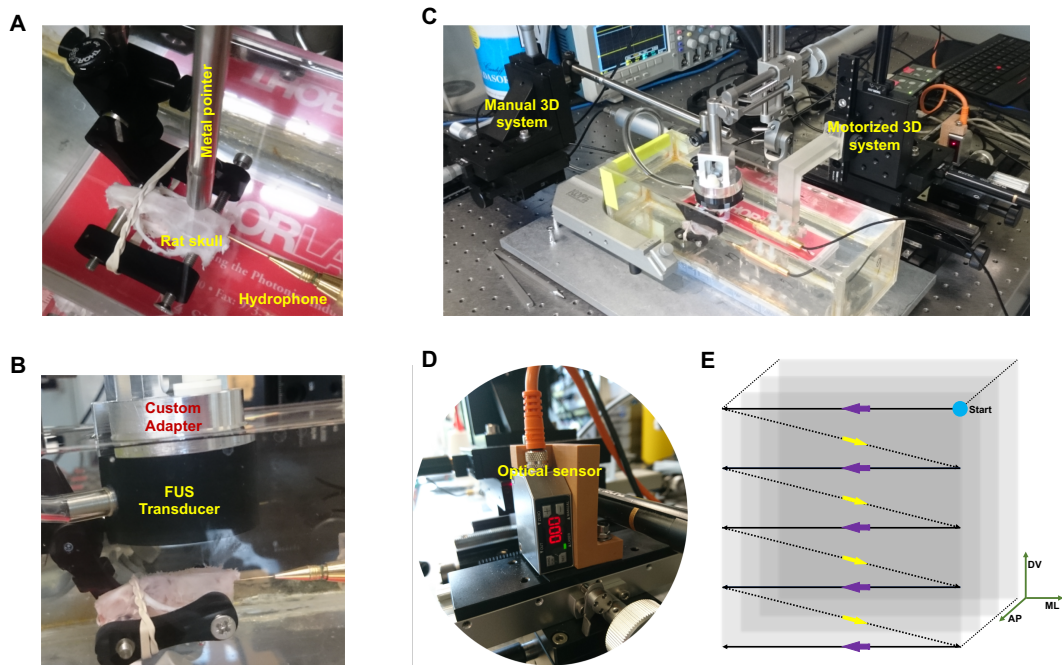


Figure 3.4 Real setup images and scanning protocol.

(A) The skull is positioned flat with the help of a manually controlled 3D system (Figure 3.4-C, left). The tip of the metal pointer is positioned on the bregma with a motorized stereotaxic arm.

(B) The pointer is replaced with the FUS transducer which is attached to a custom designed metal adapter such that the focal point of the transducer coincides with the tip of the metal pointer.

(C) The complete system during scanning. The manual 3D system is positioned on the back of the stereotaxic system and controls the skull with the aid of a number of posts and optomechanical kits.

(D) The scanning algorithm: The focal volume is determined manually with a hydrophone. After determining the scanning volume, the hydrophone is positioned to focal point and a custom MATLAB script is run. The algorithm moves the hydrophone to the right-top of the most anterior side (blue dot). The scanning starts from the blue point, takes one continuous movement to the left and during this time hydrophone continuously samples pressure values and saves into a file. Then the hydrophone is moved down 100 μm by the DV motor, then the ML motor starts another run from the right to left until one layer is completed. Then the AP motor moves 100 μm forward, the second layer is also scanned in the same way until all the layers are completed. After completion, the hydrophone is moved to the initial position.

3.3.4 Calculation of skull transmission factor

To measure the transmission factor of the skull, the peak negative pressure was measured with the hydrophone at the focal point of the transducer (P1), then the skull was moved in between the transducer and the hydrophone. Because the skull acts as a lens, the focal area shifts in the dorsal direction (depending on the incident skull region, thickness and target depth). For coordinates used in this study (4 mm rostral to bregma and 7 mm ventral from skull surface), the focal point shifted up around 0.6 mm. However, as targets move more anterior, the skull shape becomes more concave thus the shift in the DV increases. Hence, the hydrophone was repositioned to find the new focal area and peak negative pressure was measured again (P2). The transmission factor is calculated as $P2/P1 \times 100$. For the brain region 4 mm rostral and 7 mm ventral to bregma, the transmission factor was 0.35 (65% loss; Figure 3.1), however for skull region above vS1 (used in Chapter 2) we expect ~70% loss due to greater skull thickness. Our data is in consistent with previous findings¹⁵⁹.

3.3.5 Degassing water

Milli-Q water was degassed with a Liqui-Cel membrane contactor (1.7x5.5 MiniModule, 3M Deutschland GmbH). The contractor was positioned vertically (Figure 3.5-A), the input takes water from the water chamber positioned above (filled with DI water) and

the output delivers the degassed water to a chamber positioned below. The two inputs on the side are connected to a vacuum line. When the vacuum machine is turned on water starts flowing from input to output. The degassed water was then tested with a water testing kit (CHEMetrics, K-7512, Fisherscientific) which measures the dissolved oxygen gas level in water. 1.5-2 ppm (mg/L) was considered suitable for ultrasound experiments¹⁶⁰.

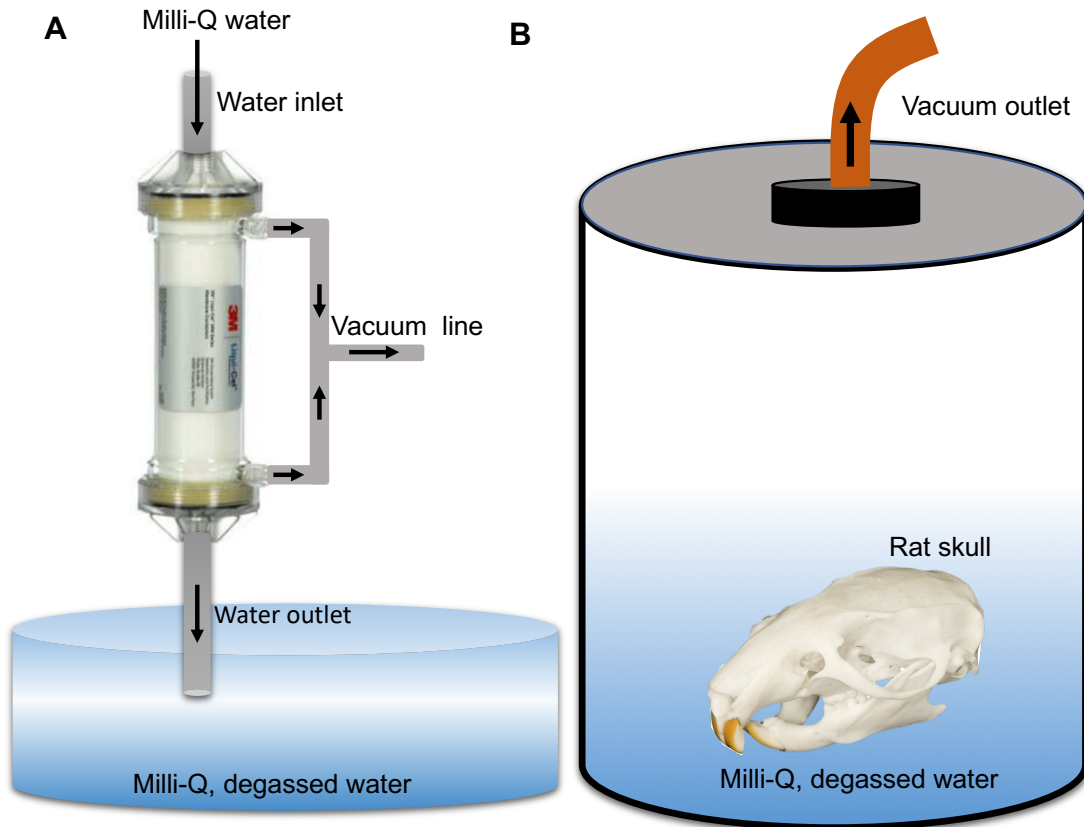


Figure 3.5 Demonstration of water and skull degassing setups.

(A) A membrane contractor is positioned vertically the water is sucked with a vacuum line which allows travelling water through the membrane.

(B) The skull is vacuumed in degassed water in the vacuum chamber. Skull image is used with permission of “Skulls Unlimited” (<https://www.skullsunlimited.com>)

3.3.6 μ CT imaging and 3D image reconstruction

The skull surface model was generated from the μ CT image by thresholding the normalized CT images to 500 Hounsfield Units (HU) within the open source iSeg (ZMT

Zurich MedTech AG, Zurich, Switzerland) software platform. Skull heterogeneity and its acoustic properties were derived from the HU according to the approach of Pichardo and colleagues¹⁶¹ where HU linearly maps to density, and density nonlinearly maps to the speed of sound and attenuation in skull.

3.4 Discussion

The skull is a key parameter when we consider FUS for therapeutic intervention of brain disorders. Due to its multilayered complex structure, skull causes significant phase aberrations and attenuation thereby limiting targeting and efficiency of FUS treatments. Currently, the only clinically viable solution for correcting phase aberrations is based on multi-element transducers. However, as this system is not practical with current treatment settings, more affordable solutions are in great need. A better understanding of the physical properties of the skull will likely lead to more novel solutions and/or help improving recently proposed methods^{155,156}. To help this endeavor, we presented a fast and affordable automated 3D scanning system for characterizing skull related distortions on FUS beam in rodents. We provide a full protocol for skull experiments and visualize the effect the skull on the FUS beam in rats. We show that integrating an optical distance sensor to a standard motorized 3D system by Thorlabs helped increasing the speed of 3D pressure distribution measurement by at least 10-fold. Moreover, we have shown that the 3D scanning results could help developing and validating numerical skull models.

Chapter 4

Parts of this chapter are from the following manuscript in preparation.

“Transient seizures followed by Focused Ultrasound induced Blood-Brain Barrier opening”

Mehmet Sirin Ozdas, Aagam S. Shah, Paul M. Johnson and Mehmet Fatih Yanik

Institute of Neuroinformatics, D-ITET, ETH Zürich, Switzerland

Transient seizures followed by FUS induced BBB opening

4.1 Introduction

The Blood-Brain Barrier (BBB) is a multi-cell complex structure which prevents neurotoxic plasma, blood cells, immune cells and pathogens from entering brain^{162,163}. The BBB also helps maintaining the homeostasis of brain by trafficking ions and molecules in and out of brain¹⁶⁴. The integrity of the BBB is essential for proper communication between neural circuits as fluctuations in concentrations of ions or neurotransmitters in the extracellular space could cause random excitatory or inhibitory activity in brain which might ultimately lead to uncontrolled or undesired behavior. While the BBB plays an important role for maintenance of homeostasis and safety of brain, it prevents many therapeutic agents from entering brain thereby severely limiting the range for pharmaceutical interventions for CNS disorders¹⁶⁵. For a drug to cross the BBB it must have the following characteristics; high lipophilicity, forming maximum 8-10 hydrogen bonds with solvent water, partition coefficient (Log P) values between of 1.5-2.7, being non-ionized and having molecular mass below 400-500 Dalton (Da)^{165,166}. It has been estimated that at 98% of all small molecules and all large molecules do not have these characteristics therefore cannot be used for therapeutic intervention of CNS disorders¹⁶⁵. The remaining small molecules which cross the BBB can only be used for treatment of affective disorders (e.g. depression, anxiety), epilepsy and chronic pain while there is no or only weak treatments for the majority of nondegenerative and neuro-oncological disorders¹⁶⁵.

Several strategies have been proposed to overcome the impermeability of the BBB. Perhaps the most obvious approach would be considering transcranial drug delivery approaches such as intracerebral implantation, convection enhanced diffusion (CED) and

intracerebroventricular (ICV) injection. These methods can be promising for treatment of a range CNS disorders such as diffuse intrinsic pontine glioma (DPIG) and Parkinson's Disease^{167,168}. However they are expensive and require invasive procedures among other limitations¹⁶⁹. Trans-nasal drug delivery is another proposed method, however there is no pharmacokinetic evidence which supports higher efficiency of this method compared to intravenous administration of the same drug at the same dose¹⁷⁰. Moreover side effects such as irritation in the nasal mucosa cannot be avoided¹⁶⁹. Endogenous BBB transporters and receptor-mediated transcytosis have also been used to circumvent BBB. Although these are potentially very promising techniques and there have been many preclinical studies, so far only few drugs (e.g. L-Dopa) have been successfully used for treatment of a specific CNS disorder¹⁷¹. The solvent and immune adjuvant-based BBB disruption methods have also been proposed to mediate delivering large and small molecules which do not otherwise cross the BBB. While they are non-invasive, these approaches do not open the BBB in a controlled and targeted manner, therefore are considered to be clinically unsafe¹⁷².

Focused ultrasound and microbubbles (FUS+MBs) assisted BBB opening is a promising method for targeted delivery of large and small molecules which do not cross the BBB. The basic mechanism behind FUS+MB BBB opening is believed that when systemically injected microbubbles (usually with 1-2 μ m diameter) coincide with FUS in the capillaries, they expand and collapse thereby disrupt the tight junctions formed by endothelial cells¹⁷². It has been claimed that the BBB can be transiently and repeatedly disrupted in rodents¹⁷³, non-human primates¹⁷⁴, and in humans in safe manner¹⁷⁵. However the safety claims for BBB opening are currently unsubstantiated and recent studies have shown that FUS+MBs BBB opening may not indeed be safe as claimed, as it causes sterile inflammation at similar level that is observed in traumatic brain injury and ischemia²⁵. While counterclaims suggest that inflammation and cell death can be prevented by injecting less concentration of microbubbles, there is still an ongoing debate between FUS experts²²⁻²⁶. Moreover, beside sterile inflammation, recently it has been shown that FUS+MBs BBB opening can suppress sensory evoked potentials²⁸ and even induce behavioral changes¹⁷⁶. While the exact mechanism behind this neuromodulation remains elusive, we provide further evidence of FUS+MBs BBB opening-induced neuromodulation by performing *in-vivo* electrophysiology directly from extracellular space of brain with simultaneous FUS+MBs application. We positioned focused ultrasound on vibrissae sensory cortex (vS1), inserted a penetrating multi-electrode array into vibrissae motor cortex (vM1) and injected microbubbles from tail vein (Figure 4.1). We observed that FUS+MBs BBB opening cause transient and repeated seizures at gamma-band frequency range in vM1. Moreover, we found out that the seizures start from deep cortical layers

(L5A of vM1, recording site) and propagate to upper layers (L1 of vM1) in 13 seconds on average. Interestingly, following cessation of seizures, we observed a complete silencing of activity (evoked and spontaneous) in relevant brain regions for several mins. Following this silent period, the spontaneous extracellular spikes return to baseline rates. However, following the first seizure, which occurs after the BBB opening in vM1, a long-term inhibition in sensory-evoked potentials was observed. While it requires further investigations to understand these physiological changes, our findings provide more insight into the physiological effects of BBB opening, which may ultimately aid in a better understanding of the safety of FUS+MBs BBB opening.

4.2 Results

To show real-time electrophysiological response of FUS+MBs BBB opening, we used the vS1-vM1 paradigm (Figure 4.1), introduced in Chapter 2. Opening the BBB in vS1 and recording from vM1 allowed us to evaluate Evans Blue (EB) extravasation without confounding effects from probe insertion⁹⁵. Since the Transitional Zone (TZ) of vM1 receives direct excitatory synaptic projections from vS1¹⁰², we likely observe the seizures which are originally induced in vS1 but propagate to vM1 through direct synaptic projections in TZ region. Since the whisker evoked potentials in vS1 propagate to vM1 with 3 ms delay and at a lower amplitude (Figure 2.6-B in Chapter 2), we anticipate that the seizures as well first appear in vS1 then propagate to vM1 with 3 ms delay and at smaller amplitudes. We injected either UC-Carriers (Chapter 2) or standard microbubbles (without liposomes attached) and applied either burst FUS sequence or variations of AU-FUS sequences (see Table 4-1). FUS+MBs BBB opening-induced seizures have been observed in all animals robustly as long as we sonicated circulating microbubbles in the brain region of interest (vS1) with sufficient pressure (MI=0.33-0.47, *on-situ*) and/or duration. The BBB opening was assessed with EB and in most animals EB extravasation was observed in vS1.

Unlike other methods used for measuring electrophysiological response of FUS+MBs BBB opening, we used penetrating micro-electrode arrays to directly assess extracellular neural activity. This allowed us to measure spike activity from different cortical layers affected by BBB opening, and more specific local field potentials directly from vM1 (Figure 4.2-A) rather than measuring evoked-fMRI and EEG responses which either suffer from low temporal or spatial resolution. Measuring LFPs and multi-unit spikes we observed that

FUS+MBs BBB opening can elicit multiple seizures (Figure 4.2-B), which propagate from deep layers (L5A) to superficial layers (L1)[Figure 4.2-E], and is followed by inhibition in the evoked LFPs (Figure 4.2-C), consistent with other reports²⁸. Moreover, we also observed a refractory period following seizures in vM1, where high-frequency spiking is followed by brief periods of silence (Figure 4.2-B), and this repeated burst-silence pattern continues for prolonged periods of time. Intriguingly, whisker evoked-LFPs in vM1 are significantly reduced following the first seizure and remain nearly absent despite ongoing repeated seizures and subsequent silent periods in spiking activity. Finally, the power spectrum density analysis showed that seizures occurred at 73 Hz on average (Figure 4.2-D), which is considered in high gamma range.

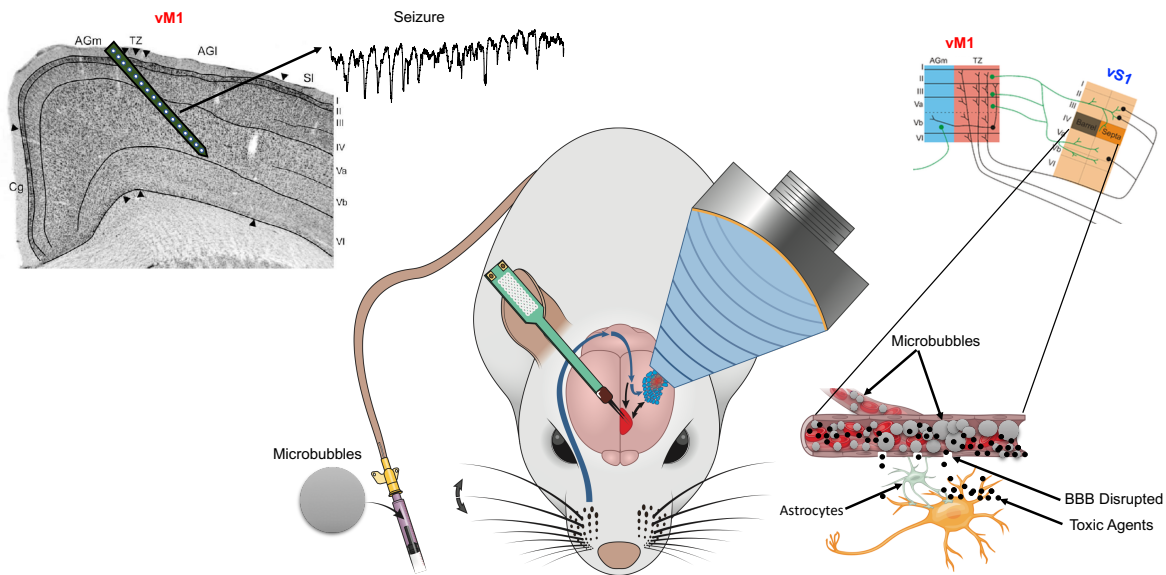


Figure 4.1 Graphical abstract of the experimental setup.

The animal was anesthetized, a small craniotomy was performed over vM1 (TZ region)^{82,94} for inserting the recording probe, and the FUS transducer was positioned on the intact skull above vS1 using stereotaxic coordinates and coupled with sterile ultrasound gel and water collimator. Whiskers were mechanically deflected at 0.3 Hz. Microbubbles were injected intravenously through the tail vein; the ultrasound sequence parameters are set from the computer. Upon sonication, microbubbles expand and collapse. This process transiently disrupts BBB and likely allows toxic agents diffuse into extracellular space. The effect of BBB disruption in vS1 is measured from a functionally connected but anatomically distant region, vM1. vM1 coronal section (top-left) and vS1-vM1 projections illustration (top-right) are modified with permission of Chakrabarti and Schwarz¹⁰².

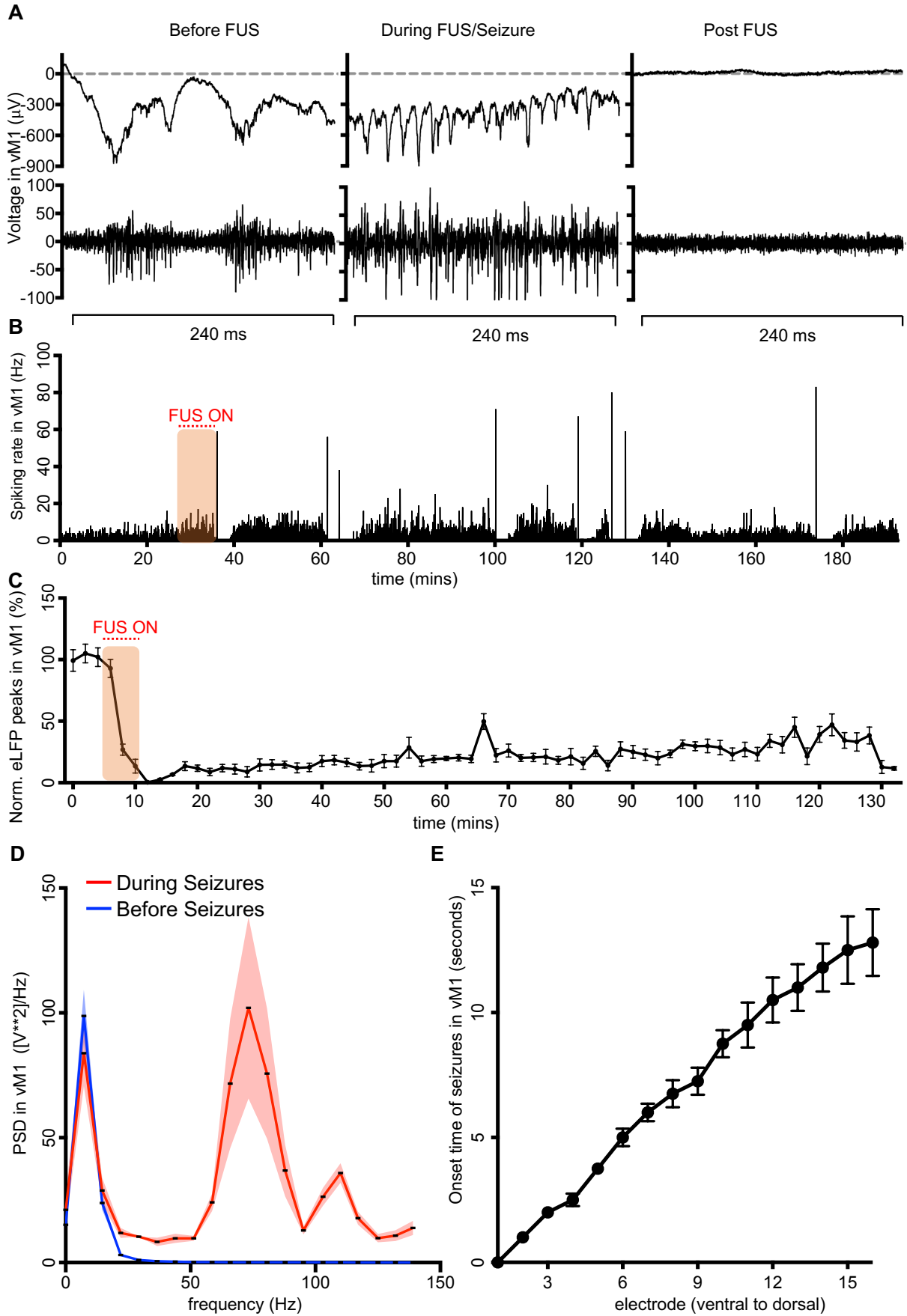


Figure 4.2 FUS induced cortical seizure characterization.

(A) Example of raw (top) and high pass filtered (bottom) recordings before, during, and post FUS. Each window has a 240 ms duration. “Before FUS” represents at least 5-10 mins before microbubble injection and FUS sonication (left), “During Seizures” represents high frequency oscillations during or immediately after BBB opening during FUS sonication on circulating microbubbles. The “Post FUS” window represents one minute after the seizure detection.

(B) Example of multi-unit spiking rate in vM1, from one electrode in one animal with one second bin size. Each peak represents a high number of extra-cellular spikes during seizures.

(C) Evoked LFPs before and after FUS-induced BBB opening in one animal. Seizures can be detected very soon after FUS sonication depending on bubble concentration and FUS pressures. Lower bubble concentration or FUS pressure would delay seizure or BBB opening onset time or not induce opening. Inhibition of evoked LFPs in vM1 begins with BBB opening and can last more than 2 hrs depending on FUS sequence pressures and microbubble concentration.

(D) Power spectral density of raw data in vM1 before and during seizures, n=4. The peak mean power is detected at 73.2 Hz, Power=102± 36.4 in (V**2/Hz). All data are mean ± s.e.m.

(E) Propagation of seizures through cortical layers of vM1, n=4 animals. Seizures first occur in the deep layers of vM1 then propagate to upper layers. All data are mean ± s.e.m.

Condition	MI_1 [PNP]	t_1 (ms)	MI_2 [PNP]	t_2 (ms)	t_3 (ms)	PRF (Hz)	NOC
AU-FUS	0.63 [1]	500	1.1 [1.75]	90	200	100	10000
Burst-FUS	1.58 [2.5]					1	25000

Table 4-1 Example of Ultrasound sequences for BBB opening.

MI – mechanical index, PNP – peak negative pressure in megapascal (MPa) (skull attenuation not accounted for; see Section 3.3.4 in Chapter 3), t_1 – pulse duration (in milliseconds) of radiation sequence, t_2 – duration (in milliseconds) of fragmentation sequence, t_3 – duration (in milliseconds) of delay between uncaging sequence end and start of the following aggregation sequence, PRF – pulse repetition frequency in Hz, NOC – number of cycles. All the 4 animals were (Figure 4.2-D & Figure 4.2-E) treated with very similar AU-FUS sequences presented in the table. EB extravasation was observed in all animals at FUS spot, however the concentration changed depending on parameters. Note that aggregation and uncaging sequence names introduced in Chapter 2 were replaced with radiation and fragmentation names here as the main mechanism was BBB opening unlike drug aggregation and uncaging with AU-FUS (*in-vivo*).

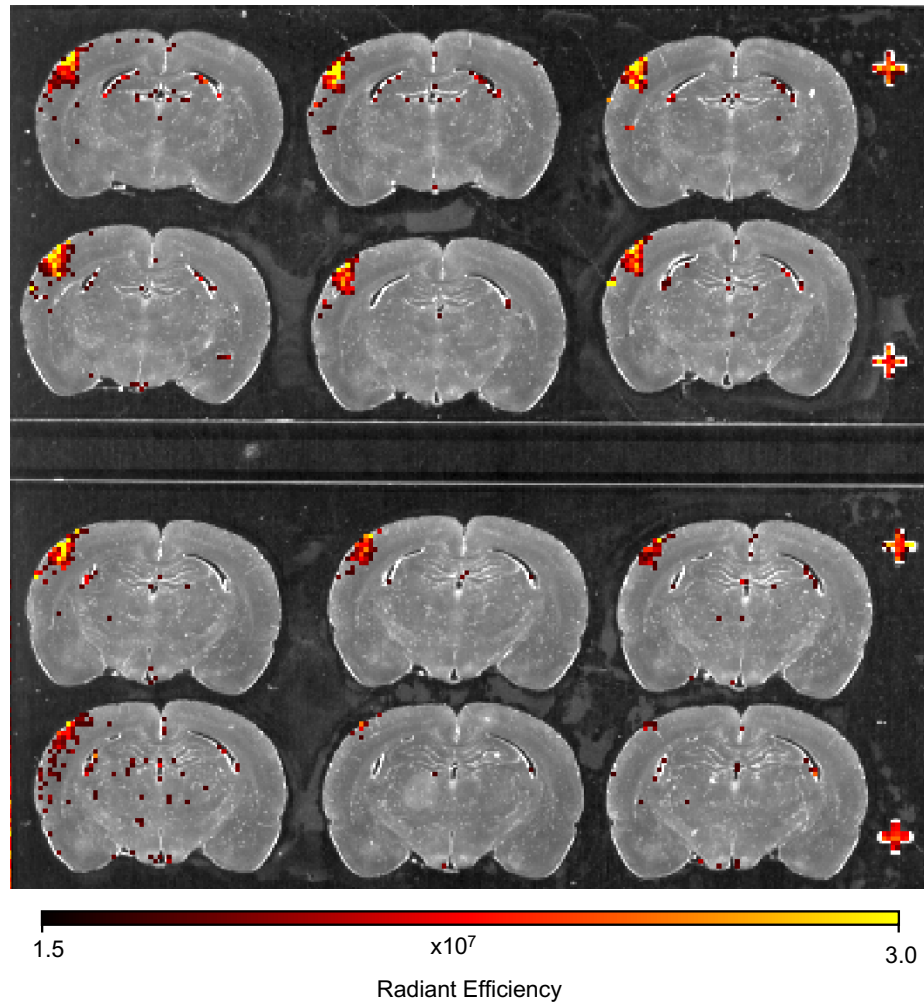


Figure 4.3 BBB opening following FUS sonication.

An example IVIS spectrum imaging of Evans Blue dye extravasation following AU-FUS parameters that opens BBB. Evans Blue extravasation is observed in vS1 of the left hemisphere where FUS sonication occurred. Following FUS parameters were used for 7 mins with 1×10^9 bubble concentration: $t_1 = 500$ ms, $t_2 = 90$ ms, $MI_1 \approx 0.71$ [1.12 MPa], $t_3 = 300$ ms, $MI_2 \approx 0.94$ [1.5 MPa], $PRF = 100$ Hz, $NOC = 10000$. The skull attenuation not counted (see section 3.3.4 in Chapter 3).

4.3 Methods

As explained in the Chapter 2, we systematically changed many FUS sequence parameters to achieve local drug concentration without BBB opening. The data presented in this chapter is part of the parameter tuning experiments where we were testing different ultrasound sequences to understand which parameters would cause local drug concentration without BBB opening. Although it is not a common practice to use liposomes attached microbubbles for BBB opening, mechanistically it is the same except that this combination required higher ultrasound pressures to open BBB compared to microbubbles alone. This is probably due to increased mass of bubbles with liposomes. All the methods used in this chapter are the same as the ones in Chapter 2 (FUS with simultaneous electrophysiology) and Chapter 3 (for skull attenuation measurements) except the following changes.

4.3.1 Focused Ultrasound

1) The collimator geometry was changed such that the focal point of the FUS transducer targets 2.5 mm below the skull surface instead of 3.3 mm used in the Chapter 2. This change was done to target in the center of the vS1. The seizures were observed with 3.3 mm collimator as well although this data is not presented in this chapter.

2) FUS sonication duration was 7 mins, bubble concentration was 1×10^9 in 1 mL saline. Liposomes had 10% cholesterol.

4.3.2 Electrophysiology data analysis

All electrophysiological data analysis was done in Python, version 3.6, using custom scripts. For eLFP analysis, the raw data was low pass filtered (3rd order Butterworth filter) at 300 Hz. The eLFP peaks were extracted based on the time stamp of the whisker stimulus, were averaged over 2 mins then normalized to the average response of the baseline. Extracellular spike detection and sorting was done with Klustakwik, an open source software¹¹⁵. Multi-unit activity (spiking rates) were then extracted through a custom code in Python. Data is mean \pm s.e.m. For high pass filtering, a 3rd order Butterworth filter with cut-off frequency of 300 Hz was used.

For power spectral density, the Welch method was used with python SciPy package, the number of segments (nspereg) was 4096 (~7 Hz resolution), default values were used for

the rest of parameters. To calculate the timing of seizures (first seizure in each electrode) through cortical layers, the whole recording session was divided into bins of 1 seconds and assigned into arrays. For each bin, the number of all multi-unit spikes detected in one electrode were counted. The electrode which showed the first seizure was considered as reference and the timing of seizures in other electrodes were subtracted from the reference electrode. During seizures high firing rates were observed in most of the electrodes but not all electrodes showed spiking activity. The time bin which seizures occurred in each electrode were found automatically with a python script. However, as few electrodes did not show any activity, the automated function showed misleading numbers for the timing of seizures. These few bins were replaced with the nearest preceding bins manually. The recording probe used was 2 shanks Neuronexus, A2x16-100mm-100-200-177. Always the shank which had the highest activity was considered for data analysis.

4.4 Discussion

The Blood-Brain Barrier is a major bottle neck for delivery of all large as well as 98% of the small molecules¹⁶⁵. Although some drugs are effective for treatment of brain tumors and neurological disorders using *in-vitro* assays, they cannot be used for clinical treatments due to their low penetration rates through the BBB. Therefore, increasing drug uptake across the BBB by any safe means could bring tremendous benefit to healthcare. Focused Ultrasound has been proposed to address this challenge due to its capability to open the BBB in local brain regions transiently and noninvasively. Although an increasing number of studies claim the safety of FUS+MBs BBB opening, many questions remain unanswered and the reliability of safety assessments are challenged by serious concerns²⁵. Therefore, the claims supporting the safety of BBB opening remain unsubstantiated. In addition to previously published reports where local inhibition of sensory evoked activity with fMRI and EEG has been reported^{28,177}, we provide further insight into the consequences of BBB opening by *in-vivo* electrophysiology with penetrating electrodes for the first time. This method allowed us to observe repeated transient seizures post BBB opening and propagation of seizures through cortical layers, which is not observable using BOLD imaging or EEG alone. Although the presented results cannot address the exact cellular and molecular mechanism behind FUS+MBs BBB opening induced seizures and inhibition followed by seizures on the evoked potentials, our findings and methods can form a starting point for future studies.

Perhaps such repeated seizures and subsequent silencing could help gain insight into Alzheimer's disease as BBB dysfunction is commonly observed in Alzheimer as well as other neurodegenerative disorders¹⁷⁸, and as seizures are also commonly observed in Alzheimer's patients along with dementia¹⁷⁹. Recently BBB dysfunction has been suggested as an early biomarker for human cognitive dysfunction independent of A β or tau biomarkers of Alzheimer's Disease¹⁸⁰. However, any causal link between Alzheimer's and BBB dysfunction remains unclear¹⁸¹. Since the FUS+MBs can open BBB repeatedly in local brain areas, this technique might be useful to study the causality between Alzheimer and BBB dysfunction by repeated BBB opening in the same area, possibly in hippocampus, or multiple areas over extended periods. Extensive analysis of molecular

and behavioral changes, as well as functional connectivity changes between different brain regions, could shed light on the causality between BBB dysfunction and Alzheimer's disease. If repeated BBB opening over long-time results in other molecular and behavioral biomarkers of Alzheimer's, such as $A\beta$, tau and memory problems, FUS+MBs BBB opening might be useful to create new Alzheimer animal models which could be used for developing new therapeutic interventions.

We assessed the BBB opening with Evans Blue (EB) dye and in most of the animals which showed seizures EB was detected in the sonication region (all four animals analyzed for this chapter showed EB extravasation). Perhaps the absence of EB in some brains could suggest that seizures could be considered a more sensitive electrophysiological biomarker for BBB opening. Although these results, especially detection of multiple seizures even long time after FUS application was completed, suggest that seizures occurred upon BBB opening, further evidence can be derived by simultaneous electrophysiology and passive cavitation detector (PCD) monitoring which is commonly used to assess BBB opening by measuring stable and inertial cavitation¹⁸². In the presented methodology, it was infeasible to perform simultaneous PCD monitoring and electrophysiology as using the FUS collimator was severely limiting the PCD signals due to the small contact area with brain (through skull). However, having multiple seizure activity was strongly indicating the BBB opening, perhaps triggered by the entry of systemic neurotransmitters or other agents to the brain from the blood vasculature.

Chapter 5

Concluding Remarks

In this thesis, we introduced a new method of neuromodulation which has potential to be used for treatment of brain disorders. The method achieves non-invasive, receptor specific neuromodulation with high spatial precision by employing ultrasound-sensitive drug carriers and focused ultrasound. All the individual ingredients of our microparticles (microbubbles and liposomes) have been previously approved by FDA for clinical use, and the ultrasound sequence was uniquely designed such that a high concentration of drug in small brain regions can be achieved without BBB opening at ultrasound intensities much below clinical safety levels.

The thesis has three chapters, each with its own introduction and conclusion, therefore the reader should refer to the dedicated conclusion of each chapter. Here, we will give a general conclusion about the experiments performed and discuss potential use of the proposed technologies in treatment of psychiatric disorders. We will also discuss possible strategies for improving the efficiency of our technologies.

The drug delivery method was designed as a proof of concept study and tested on rats and is therefore not yet ready to be used for humans at its current stage. The transducer geometry and the center frequency were chosen considering trade-offs between ultrasound penetration through the skull and the spatial resolution of the focal volume. When the center frequency is increased, the resolution of the focal volume also increases, however the skull causes significantly more absorption and phase aberrations. Considering the brain size, the skull thickness of rats, and the spatial resolution required for targeting cortical and sub-cortical circuits (e.g. sensory cortex, orbito-frontal cortex, dorsolateral striatum), we decided to use 2.5 MHz transducer with 40 mm diameter and 20 mm focal depth to achieve sufficiently high pressures in order to uncage the drug content of ultrasound-controlled drug carriers in the target brain area.

Our ultrasound sequence design is based on the chemistry and physical properties of drug carriers and tuned such that it achieves high concentration of small molecules without BBB opening and with millimeter precision *in-vivo*. This was highly challenging; all the parameters in the AU-FUS (*in-vivo*) sequence required systematic optimization. The chemistry of the liposomes, the size of microbubbles, the fat percentage in the shell of the liposomes were all carefully designed to find a regime where the particles were stable

enough to circulate in the blood stream but sensitive enough to uncage the drug in the target when exposed to low ultrasound pressures. For example, the too short duration of aggregation sequence would not allow enough aggregation of particles in the capillary thereby not having enough drug concentration in the desired duration. Excessive application of the aggregation sequence could theoretically lead to saturation of the volume of the aggregate. Considering capillary size and focal volume of the transducer, a limited number of particles could be aggregated, therefore longer duration would not increase drug concentration. Increasing the number of cycles, pulse repetition frequency and duration of uncaging sequence would increase the chance of the BBB opening. We therefore systematically tested many different parameters until we found the sequence and the drug carrier's parameters to achieve the aim of the project, which was locally concentrated drug release without opening the BBB.

Using our current parameters, we slowly infuse the drug carriers over 20-30 mins, as increasing the concentration of the bubbles too rapidly would increase the chances of BBB opening. Thus, the drug delivery process is also slow. We can likely shorten the duration of the FUS by increasing the bubble concentration but lowering the FUS pressures. There is still a room for this optimization because we didn't have chance to test lower pressures for aggregation and uncaging pulses due to limited time and resources. Our drug carriers could also be further modified; one interesting strategy could be increasing the liposome size such that more drug is capsulated on each bubble, this might also make the bubbles less violent as it would also increase their mass when conjugated with bigger liposomes.

If the method is proven to be safe enough to translate to humans, a possible way would be using commercially available multi-element transducers with MRI guidance (i.e. the ultrasound focal volume position can be changed with the aid of MRI). Such systems would allow precise targeting with FUS, theoretically, in any brain region with sub-millimeter precision. Although multi element transducers (e.g. Insightec) are approved for tumor/tissue ablations, they are very bulky and expensive. It would not be an accessible tool which many patients could benefit. They would most likely be used if a drug, such as ketamine which can induce long term therapeutic benefits with a single treatment, is delivered. However, as the FUS applications are getting more attention, new approaches are being proposed. Maimbourg and colleagues^{156,151} proposed that 3D-printed acoustic lenses can be used to correct phase aberrations induced by the skull. More recently holographic lenses have been introduced to focus arbitrary ultrasound fields intracranially with a single element transducer¹⁵⁷. These new approaches and possible future advancements (e.g. MEMS based transducers) may reduce the cost and increase the practicality of the ultrasound applications for the treatment of brain disorders.

The effectiveness of FUS depends on the ability to know the dimensions of the focal area and the pressures within this area. However, skull properties vary regionally in both rodents and humans, and this can cause different levels of attenuation of pressure as well as phase aberrations, altering the shape and intensity of FUS at the target region. We have developed a system which allows one to determine targeting accuracy and intensity. Since the skull causes significant challenges for the practical use of FUS in the treatment of brain disorders, we provide a full chapter about skull experiments we present a fast, reliable and affordable 3D scanning system. The system is explained, the effect of the skull is visualized in 3D and the data was tested on a numerical skull model. Moreover, we also provide the most comprehensive report about performing skull experiments with detailed protocol. This work has potential implications for clinical translation by improving modeling that corrects problems of skull-induced distortions.

As far as the safety is concerned, we tested mainly the BBB opening with Evans Blue (EB) dye and an MRI contrast agent (Gadolinium). Although these important metrics are used commonly for assessment of the BBB opening in the FUS field, further histology such as glial fibrillary acidic protein (GFAP) and Tunnel staining would likely give more information (e.g. cell death, inflammation) for the safety of the method. Further safety evaluations about the bubble amount that can be injected to the body and the cavitation detection with passive cavitation detector (PCD) is the work under progress.

Intriguingly, we discovered that when we intentionally open the BBB with FUS+MBs in vS1, repeated seizures occurred in vM1 and they propagate from deep cortical layers (L2/3-L5A) to upper cortical layers (L1). This is likely an electrophysiological biomarker of the BBB opening which was never reported previously *in-vivo* and substantiates the concerns regarding the safety of the BBB opening. Although the presented data suggest that the seizures occurred due to BBB opening, simultaneous PCD monitoring with electrophysiology could further support the claim.

We assessed the drug delivery only with evoked electrophysiological responses, which is acceptable for assessment of pharmaceutical effects of drugs in pre-clinical studies, however measuring the drug concentration directly with implanted micro dialysis probes would give us more direct information about the amount of the delivered drug in the target and off-target sites. This work is currently underway.

As discussed in the motivation, due to major differences between rodent and human brain, it is unlikely to create perfect animal models to understand the mechanisms behind

psychiatric disorders in humans and to find strategies for treatment. In future, advanced non-invasive imaging techniques could reveal circuit dysfunctions more precisely and thereby allow objective electrophysiological patterns to create accurate computational models of psychiatric disorders. If the presented method can be safely used for targeted drug delivery in humans (e.g. SRRIs, ketamine), it could pave way for personalized treatments where FUS mediated drug delivery could be employed based on computational models of psychiatric disorders.

In summary, in this thesis we presented very likely the most advanced ultrasound-based technologies for targeted non-invasive drug delivery to brain circuits. We reported for the first time that FUS+MBs assisted BBB opening causes repeated seizures in brain. And we presented an affordable and high speed 3D scanning system for characterization of skull induced artifacts on FUS beam with highly precise methodologies.

Chapter 6

Appendix

Initial weight					
	Volume [mL]	calc. [mg]	eff. [mg]	ng/ml calc.	ng/ml eff.
Muscimol	10	2.00000	2.185	200'000	218'500
(3-methyl-1,2-oxazol-5-yl)methanamin ISTD	2	0.20000	0.232	100'000	116'000

Muscimol					
Solutions	Conc. calc. [ng/mL]	Conc. eff. [ng/mL]	Volume [mL]	Volume aliquot	
SL_ (Muscimol)	200'000	218'500			
WS1_ (Muscimol)	10'000	10'925	1	50 µL SL_ (Muscimol)	
WS2_ (Muscimol)	500	546	1	50 µL WS1_ (Muscimol)	
WS3_ (Muscimol)	25	27.3	1	50 µL WS2_ (Muscimol)	
STD 1	0.50	0.546	1	20 µL WS3_ (Muscimol)	
STD 2	2.00	2.185	1	80 µL WS3_ (Muscimol)	
STD 3	10.00	10.925	1	20 µL WS2_ (Muscimol)	
STD 4	50.00	54.625	1	100 µL WS2_ (Muscimol)	
STD 5	250.00	273.125	1	25 µL WS1_ (Muscimol)	
STD 6	500.00	546.250	1	50 µL WS1_ (Muscimol)	
STD 7	1'000.00	1'092.500	1	100 µL WS1_ (Muscimol)	

ISTD					
Solutions	Conc. calc. [ng/mL]	Conc. eff. [ng/mL]	Volume [mL]	Volume aliquot	
SL_ (ISTD)	100'000	116'000			
WS1_ (ISTD)	4'000	4'640.00	10	400 µL SL_ (ISTD)	
STD 1	200.0	232.00	1	50 µL WS1_ (ISTD)	
	200.0	232.00	3	150 µL WS1_ (ISTD)	

Table 6-1 Preparation of the standard and ISTD solutions used for quantification.

Weighted concentration [ng/mL]	Measured concentration [ng/mL]	% Diff
0.546	0.548	0%
2.19	2.16	-1%
10.9	10.6	-3%
54.6	54.9	1%
273	276	1%
546	569	4%
1093	1068	-2%

Table 6-2 Weighted and measured concentrations.

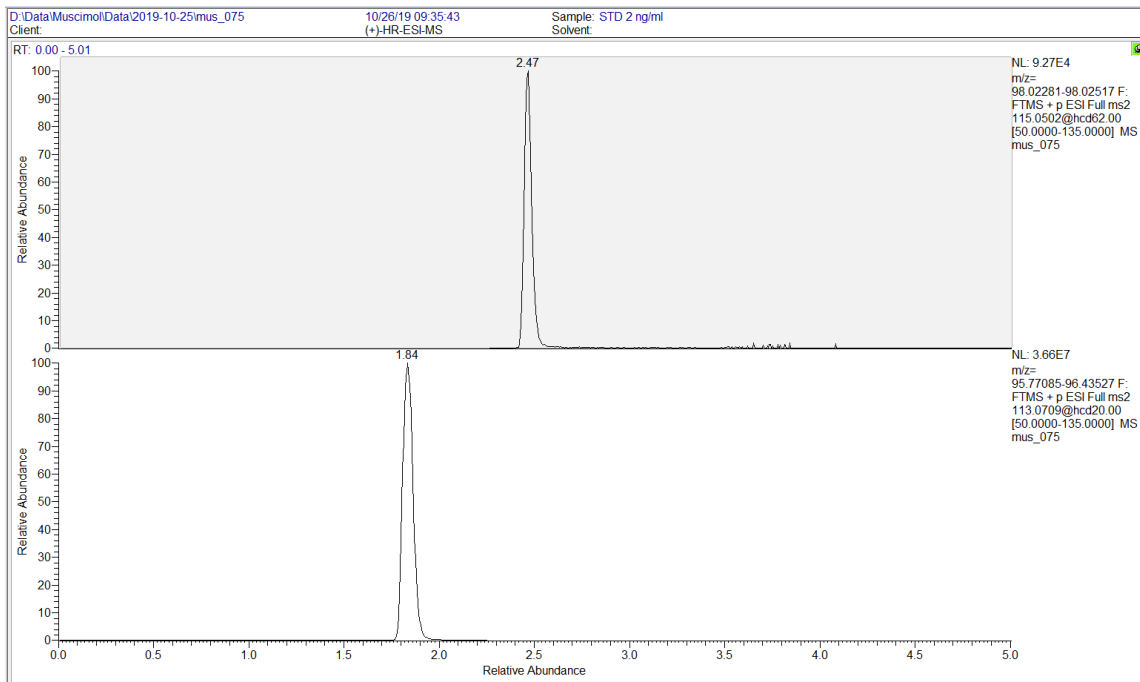


Figure 6.1 Chromatograms of ISTD at 200 ng/mL (top) and muscimol standard solution at 2 ng/mL (bottom) concentration measured with LC-HR-MS/MS.

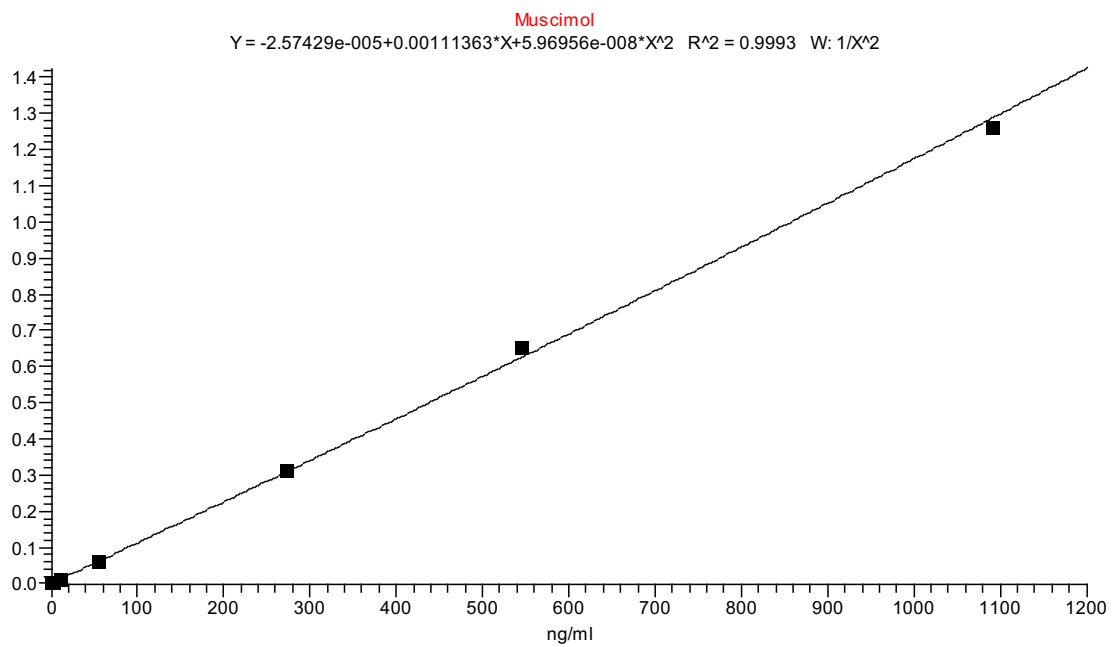


Figure 6.2 Calibration curve of muscimol standard solutions used for quantification.

References

1. Foucault, M. & Khalfa, J. *History of madness*. New York: Routledge. (2006).
2. Hyman, S. E. Revitalizing Psychiatric Therapeutics. *Neuropsychopharmacology* **39**, 220–229 (2014).
3. Cade, J. F. Lithium salts in the treatment of psychotic excitement. 1949. *Bull. World Health Organ.* **78**, 518–520 (2000).
4. Krystal, J. H. & State, M. W. Psychiatric Disorders: Diagnosis to Therapy. *Cell* **157**, 201–214 (2014).
5. Leucht, S. *et al.* Second-generation versus first-generation antipsychotic drugs for schizophrenia: a meta-analysis. *The Lancet* **373**, 31–41 (2009).
6. Wilkinson, S. T. & Sanacora, G. Considerations on the Off-label Use of Ketamine as a Treatment for Mood Disorders. *JAMA* **318**, 793–794 (2017).
7. Grady, S. E., Marsh, T. A., Tenhouse, A. & Klein, K. Ketamine for the treatment of major depressive disorder and bipolar depression: A review of the literature. *Ment Health Clin* **7**, 16–23 (2017).
8. Stephan, K. E. & Mathys, C. Computational approaches to psychiatry. *Curr. Opin. Neurobiol.* **25**, 85–92 (2014).
9. History of neuroscience: Paul Broca,
<https://www.neuroscientificallychallenged.com/blog/history-of-neuroscience-paul-broca>.
<https://neuroscientificallychallenged.com/blog/history-of-neuroscience-paul-broca> (2014).
10. Sandrone, S. *et al.* Weighing brain activity with the balance: Angelo Mosso’s original manuscripts come to light. *Brain* **137**, 621–633 (2014).

11. Athalye, V. R., Santos, F. J., Carmena, J. M. & Costa, R. M. Evidence for a neural law of effect. *Science* **359**, 1024–1029 (2018).
12. Johnson, P. M. & Kenny, P. J. Dopamine D2 receptors in addiction-like reward dysfunction and compulsive eating in obese rats. *Nature Neuroscience* **13**, 635–641 (2010).
13. Lüscher, C. & Malenka, R. C. Drug-evoked synaptic plasticity in addiction: from molecular changes to circuit remodeling. *Neuron* **69**, 650–663 (2011).
14. Dembrow, N. & Johnston, D. Subcircuit-specific neuromodulation in the prefrontal cortex. *Frontiers in Neural Circuits* **8**, (2014).
15. Sawaguchi, T. & Goldman-Rakic, P. D1 dopamine receptors in prefrontal cortex: involvement in working memory. **251**, 947–50 (1991).
16. Sawaguchi, T. & Goldman-Rakic, P. S. D1 dopamine receptors in prefrontal cortex: involvement in working memory. *Science* **251**, 947–950 (1991).
17. Zhao, W., Luo, L., Li, Q. & Kendrick, K. M. What Can Psychiatric Disorders Tell Us about Neural Processing of the Self? *Front Hum Neurosci* **7**, (2013).
18. Drevets, MD, W. C. FUNCTIONAL NEUROIMAGING STUDIES OF DEPRESSION: The Anatomy of Melancholia. *Annual Review of Medicine* **49**, 341–361 (1998).
19. Boyden, E. S., Zhang, F., Bamberg, E., Nagel, G. & Deisseroth, K. Millisecond-timescale, genetically targeted optical control of neural activity. *Nat. Neurosci.* **8**, 1263–1268 (2005).
20. Deisseroth, K. Circuit dynamics of adaptive and maladaptive behaviour. *Nature* **505**, 309–317 (2014).
21. Deisseroth, K., Etkin, A. & Malenka, R. C. Optogenetics and the Circuit Dynamics of Psychiatric Disease. *JAMA* **313**, 2019 (2015).

22. Monahan, P. E. & Samulski, R. J. Adeno-associated virus vectors for gene therapy: more pros than cons? *Mol Med Today* **6**, 433–440 (2000).
23. Kim, G. U., Kim, H.-I. & Chung, E. Towards human clinical application of emerging optogenetics technology. *Biomedical Engineering Letters* **1**, 207–212 (2011).
24. Wang, S. *et al.* Non-invasive, Focused Ultrasound-Facilitated Gene Delivery for Optogenetics. *Scientific Reports* **7**, 39955 (2017).
25. Kovacs, Z. I. *et al.* Disrupting the blood–brain barrier by focused ultrasound induces sterile inflammation. *Proceedings of the National Academy of Sciences* **114**, E75–E84 (2017).
26. Yang, F.-Y., Huang, S.-F. & Cheng, I. H.-J. Behavioral alterations following blood-brain barrier disruption stimulated by focused ultrasound. *Oncotarget* **7**, 27916–27925 (2016).
27. Mooney, S. J., Nobrega, J. N., Levitt, A. J. & Hynynen, K. Antidepressant effects of focused ultrasound induced blood-brain-barrier opening. *Behav. Brain Res.* **342**, 57–61 (2018).
28. Chu, P.-C. *et al.* Neuromodulation accompanying focused ultrasound-induced blood-brain barrier opening. *Scientific Reports* **5**, (2015).
29. Lozano, A. M. *et al.* Deep brain stimulation: current challenges and future directions. *Nature Reviews Neurology* **15**, 148–160 (2019).
30. Dandekar, M. P., Fenoy, A. J., Carvalho, A. F., Soares, J. C. & Quevedo, J. Deep brain stimulation for treatment-resistant depression: an integrative review of preclinical and clinical findings and translational implications. *Mol. Psychiatry* **23**, 1094–1112 (2018).
31. Nuttin, B., Cosyns P, Demeulemeester H, Gybels J & Meyerson B. Electrical stimulation in anterior limbs of internal capsules in patients with obsessive-compulsive disorder. *Lancet* **354**, (1999).

32. Lim, L. W. *et al.* Electrical stimulation alleviates depressive-like behaviors of rats: investigation of brain targets and potential mechanisms. *Transl Psychiatry* **5**, e535 (2015).
33. Lozano, A. M. *et al.* Deep brain stimulation: current challenges and future directions. *Nat Rev Neurol* **15**, 148–160 (2019).
34. Clair, A.-H., Haynes, W. & Mallet, L. Recent advances in deep brain stimulation in psychiatric disorders. *F1000Research* **7**, 699 (2018).
35. Kubanek, J. Neuromodulation with transcranial focused ultrasound. *Neurosurg Focus* **44**, E14 (2018).
36. Lee, W. *et al.* Transcranial focused ultrasound stimulation of motor cortical areas in freely-moving awake rats. *BMC Neurosci* **19**, 57 (2018).
37. Kubanek, J. *et al.* Transcranial ultrasound selectively biases decision-making in primates. *bioRxiv* (2019) doi:10.1101/486134.
38. Legon, W. *et al.* Transcranial focused ultrasound modulates the activity of primary somatosensory cortex in humans. *Nature Neuroscience* **17**, 322–329 (2014).
39. Guo, H. *et al.* Ultrasound Produces Extensive Brain Activation via a Cochlear Pathway. *Neuron* **98**, 1020-1030.e4 (2018).
40. Sato, T., Shapiro, M. G. & Tsao, D. Y. Ultrasonic Neuromodulation Causes Widespread Cortical Activation via an Indirect Auditory Mechanism. *Neuron* **98**, 1031-1041.e5 (2018).
41. Airan, R. D. & Butts Pauly, K. Hearing out Ultrasound Neuromodulation. *Neuron* **98**, 875–877 (2018).
42. Kim, H., Chiu, A., Lee, S. D., Fischer, K. & Yoo, S.-S. Focused ultrasound-mediated non-invasive brain stimulation: examination of sonication parameters. *Brain Stimul* **7**, 748–756 (2014).

43. King, R. L., Brown, J. R., Newsome, W. T. & Pauly, K. B. Effective parameters for ultrasound-induced in vivo neurostimulation. *Ultrasound Med Biol* **39**, 312–331 (2013).
44. Blackmore, J., Shrivastava, S., Sallet, J., Butler, C. R. & Cleveland, R. O. Ultrasound Neuromodulation: A Review of Results, Mechanisms and Safety. *Ultrasound in Medicine & Biology* **45**, 1509–1536 (2019).
45. Plaksin, M., Kimmel, E. & Shoham, S. Cell-Type-Selective Effects of Intramembrane Cavitation as a Unifying Theoretical Framework for Ultrasonic Neuromodulation. *eNeuro* **3**, (2016).
46. Gordon, J. A. On being a circuit psychiatrist. *Nat. Neurosci.* **19**, 1385–1386 (2016).
47. Tye, K. M. Neural circuit reprogramming: a new paradigm for treating neuropsychiatric disease? *Neuron* **83**, 1259–1261 (2014).
48. Perucca, P. & Gilliam, F. G. Adverse effects of antiepileptic drugs. *Lancet Neurol* **11**, 792–802 (2012).
49. De Hert, M., Detraux, J., van Winkel, R., Yu, W. & Correll, C. U. Metabolic and cardiovascular adverse effects associated with antipsychotic drugs. *Nat Rev Endocrinol* **8**, 114–126 (2011).
50. Bolognini, N. & Ro, T. Transcranial magnetic stimulation: disrupting neural activity to alter and assess brain function. *J. Neurosci.* **30**, 9647–9650 (2010).
51. Lozano, A. M. & Lipsman, N. Probing and regulating dysfunctional circuits using deep brain stimulation. *Neuron* **77**, 406–424 (2013).
52. Lynn, J. G., Zwemer, R. L., Chick, A. J. & Miller, A. E. A NEW METHOD FOR THE GENERATION AND USE OF FOCUSED ULTRASOUND IN EXPERIMENTAL BIOLOGY. *J Gen Physiol* **26**, 179–193 (1942).

53. Tyler, W. J., Lani, S. W. & Hwang, G. M. Ultrasonic modulation of neural circuit activity. *Curr. Opin. Neurobiol.* **50**, 222–231 (2018).
54. Lee, W. *et al.* Transcranial focused ultrasound stimulation of human primary visual cortex. *Scientific Reports* **6**, 34026 (2016).
55. Hynynen, K., McDannold, N., Vykhodtseva, N. & Jolesz, F. A. Noninvasive MR Imaging-guided Focal Opening of the Blood-Brain Barrier in Rabbits. *Radiology* **220**, 640–646 (2001).
56. Munoz, F., Aurup, C., Konofagou, E. E. & Ferrera, V. P. Modulation of Brain Function and Behavior by Focused Ultrasound. *Curr Behav Neurosci Rep* **5**, 153–164 (2018).
57. McDannold, N. *et al.* Targeted, noninvasive blockade of cortical neuronal activity. *Scientific Reports* **5**, (2015).
58. Raymond, S. B. *et al.* Ultrasound Enhanced Delivery of Molecular Imaging and Therapeutic Agents in Alzheimer’s Disease Mouse Models. *PLoS ONE* **3**, e2175 (2008).
59. Szablowski, J. O., Lue, B., Lee-Gosselin, A., Malounda, D. & Shapiro, Mi. G. Acoustically Targeted Chemogenetics for Noninvasive Control of Neural Circuits. (2018)
doi:10.1101/241406.
60. Wang, S., Olumolade, O. O., Sun, T., Samiotaki, G. & Konofagou, E. E. Noninvasive, neuron-specific gene therapy can be facilitated by focused ultrasound and recombinant adeno-associated virus. *Gene Therapy* **22**, 104–110 (2015).
61. Thévenot, E. *et al.* Targeted delivery of self-complementary adeno-associated virus serotype 9 to the brain, using magnetic resonance imaging-guided focused ultrasound. *Hum. Gene Ther.* **23**, 1144–1155 (2012).

62. Alonso, A. *et al.* Focal Delivery of AAV2/1-transgenes Into the Rat Brain by Localized Ultrasound-induced BBB Opening. *Mol Ther Nucleic Acids* **2**, e73 (2013).
63. Hsu, P.-H. *et al.* Noninvasive and Targeted Gene Delivery into the Brain Using Microbubble-Facilitated Focused Ultrasound. *PLoS ONE* **8**, e57682 (2013).
64. Lipsman, N. *et al.* Blood–brain barrier opening in Alzheimer’s disease using MR-guided focused ultrasound. *Nature Communications* **9**, 2336 (2018).
65. Kovacs, Z. I. *et al.* Disrupting the blood–brain barrier by focused ultrasound induces sterile inflammation. *PNAS* **114**, E75–E84 (2017).
66. McMahon, D. & Hynynen, K. Acute Inflammatory Response Following Increased Blood-Brain Barrier Permeability Induced by Focused Ultrasound is Dependent on Microbubble Dose. *Theranostics* **7**, 3989–4000 (2017).
67. Kovacs, Z. I., Burks, S. R. & Frank, J. A. Focused ultrasound with microbubbles induces sterile inflammatory response proportional to the blood brain barrier opening: Attention to experimental conditions. *Theranostics* **8**, 2245–2248 (2018).
68. Kovacs, Z. I. *et al.* MRI and histological evaluation of pulsed focused ultrasound and microbubbles treatment effects in the brain. *Theranostics* **8**, 4837–4855 (2018).
69. Kovacs, Z. I., Burks, S. R. & Frank, J. A. Reply to Silburt *et al.*: Concerning sterile inflammation following focused ultrasound and microbubbles in the brain. *Proc. Natl. Acad. Sci. U.S.A.* (2017) doi:10.1073/pnas.1711544114.
70. McMahon, D. & Hynynen, K. Reply to Kovacs *et al.*: Concerning acute inflammatory response following focused ultrasound and microbubbles in the brain. *Theranostics* **8**, 2249–2250 (2018).

71. Sweeney, M. D., Sagare, A. P. & Zlokovic, B. V. Blood-brain barrier breakdown in Alzheimer disease and other neurodegenerative disorders. *Nat Rev Neurol* **14**, 133–150 (2018).
72. Sweeney, M. D., Kisler, K., Montagne, A., Toga, A. W. & Zlokovic, B. V. The role of brain vasculature in neurodegenerative disorders. *Nature Neuroscience* **21**, 1318 (2018).
73. Nation, D. A. *et al.* Blood-brain barrier breakdown is an early biomarker of human cognitive dysfunction. *Nat. Med.* **25**, 270–276 (2019).
74. Palmer, A. M. The role of the blood brain barrier in neurodegenerative disorders and their treatment. *J. Alzheimers Dis.* **24**, 643–656 (2011).
75. Iturria-Medina, Y. *et al.* Early role of vascular dysregulation on late-onset Alzheimer’s disease based on multifactorial data-driven analysis. *Nat Commun* **7**, 11934 (2016).
76. Chu, P.-C. *et al.* Neuromodulation accompanying focused ultrasound-induced blood-brain barrier opening. *Scientific Reports* **5**, (2015).
77. Todd, N. *et al.* Modulation of brain function by targeted delivery of GABA through the disrupted blood-brain barrier. *Neuroimage* **189**, 267–275 (2019).
78. Mooney, S. J., Nobrega, J. N., Levitt, A. J. & Hynynen, K. Antidepressant effects of focused ultrasound induced blood-brain-barrier opening. *Behavioural Brain Research* **342**, 57–61 (2018).
79. Yang, F.-Y., Huang, S.-F. & Cheng, I. H.-J. Behavioral alterations following blood-brain barrier disruption stimulated by focused ultrasound. *Oncotarget* **7**, 27916–27925 (2016).
80. Airan, R. D. *et al.* Noninvasive Targeted Transcranial Neuromodulation via Focused Ultrasound Gated Drug Release from Nanoemulsions. *Nano Letters* **17**, 652–659 (2017).

81. Mao, T. *et al.* Long-Range Neuronal Circuits Underlying the Interaction between Sensory and Motor Cortex. *Neuron* **72**, 111–123 (2011).
82. Smith, J. B. & Alloway, K. D. Rat whisker motor cortex is subdivided into sensory-input and motor-output areas. *Frontiers in Neural Circuits* **7**, (2013).
83. Geers, B. *et al.* Self-assembled liposome-loaded microbubbles: The missing link for safe and efficient ultrasound triggered drug-delivery. *Journal of Controlled Release* **152**, 249–256 (2011).
84. Luan, Y. *et al.* Acoustical Properties of Individual Liposome-Loaded Microbubbles. *Ultrasound in Medicine & Biology* **38**, 2174–2185 (2012).
85. Sirsi, S. R. *et al.* Polyplex-microbubble hybrids for ultrasound-guided plasmid DNA delivery to solid tumors. *Journal of Controlled Release* **157**, 224–234 (2012).
86. Zhao, S., Ferrara, K. W. & Dayton, P. A. Asymmetric oscillation of adherent targeted ultrasound contrast agents. *Appl Phys Lett* **87**, 1341031–1341033 (2005).
87. Shortencarier, M. J. *et al.* A method for radiation-force localized drug delivery using gas-filled lipospheres. *IEEE Transactions on Ultrasonics, Ferroelectrics and Frequency Control* **51**, 822–831 (2004).
88. Unekawa, M. *et al.* RBC velocities in single capillaries of mouse and rat brains are the same, despite 10-fold difference in body size. *Brain Research* **1320**, 69–73 (2010).
89. Lum, A. F. H. *et al.* Ultrasound Radiation Force Enables Targeted Deposition of Model Drug Carriers loaded on Microbubbles. *J Control Release* **111**, 128–134 (2006).
90. Tartis, M. S. *et al.* Therapeutic effects of paclitaxel-containing ultrasound contrast agents. *Ultrasound in Medicine & Biology* **32**, 1771–1780 (2006).

91. Sirsi, S. R. *et al.* Lung Surfactant Microbubbles Increase Lipophilic Drug Payload for Ultrasound-Targeted Delivery. *Theranostics* **3**, 409–419 (2013).
92. Wang, Y. & Kohane, D. S. External triggering and triggered targeting strategies for drug delivery. *Nature Reviews Materials* **2**, 17020 (2017).
93. McDannold, N., Vykhodtseva, N. & Hynynen, K. Blood-brain barrier disruption induced by focused ultrasound and circulating preformed microbubbles appears to be characterized by the mechanical index. *Ultrasound Med Biol* **34**, 834–840 (2008).
94. Chakrabarti, S., Zhang, M. & Alloway, K. D. MI Neuronal Responses to Peripheral Whisker Stimulation: Relationship to Neuronal Activity in SI Barrels and Septa. *Journal of Neurophysiology* **100**, 50–63 (2008).
95. Wellman, S. M., Li, L., Yaxiaer, Y., McNamara, I. & Kozai, T. D. Y. Revealing Spatial and Temporal Patterns of Cell Death, Glial Proliferation, and Blood-Brain Barrier Dysfunction Around Implanted Intracortical Neural Interfaces. *Frontiers in Neuroscience* **13**, (2019).
96. Chakrabarti, S., Zhang, M. & Alloway, K. D. MI Neuronal Responses to Peripheral Whisker Stimulation: Relationship to Neuronal Activity in SI Barrels and Septa. *Journal of Neurophysiology* **100**, 50–63 (2008).
97. Smith, J. B. & Alloway, K. D. Rat whisker motor cortex is subdivided into sensory-input and motor-output areas. *Frontiers in Neural Circuits* **7**, (2013).
98. Baraldi, M., Grandison, L. & Guidotti, A. Distribution and metabolism of muscimol in the brain and other tissues of the rat. *Neuropharmacology* **18**, 57–62 (1979).
99. Helén, P. & London, E. D. Muscimol-scopolamine interactions in the rat brain: a study with 2-deoxy-D-[1-14C]glucose. *J. Neurosci.* **4**, 1405–1413 (1984).

100. Matthews, W. D., Intoccia, A. P., Osborne, V. L. & McCafferty, G. P. Correlation of [14C]muscimol concentration in rat brain with anticonvulsant activity. *Eur. J. Pharmacol.* **69**, 249–254 (1981).
101. Kelly, P. A. & McCulloch, J. Effects of the putative GABAergic agonists, muscimol and THIP, upon local cerebral glucose utilisation. *J. Neurochem.* **39**, 613–624 (1982).
102. Cornelius Schwarz and Shubhodeep Chakrabarti (2015) Whisking control by motor cortex. *Scholarpedia*, 10(3):7466.
103. Baek, H., Pahk, K. J. & Kim, H. A review of low-intensity focused ultrasound for neuromodulation. *Biomedical Engineering Letters* **7**, 135–142 (2017).
104. Tufail, Y. *et al.* Transcranial Pulsed Ultrasound Stimulates Intact Brain Circuits. *Neuron* **66**, 681–694 (2010).
105. Lee, W. *et al.* Transcranial focused ultrasound stimulation of human primary visual cortex. *Scientific Reports* **6**, 34026 (2016).
106. Guo, H. *et al.* Ultrasound Produces Extensive Brain Activation via a Cochlear Pathway. *Neuron* **98**, 1020–1030.e4 (2018).
107. Mohammadjavadi, M. *et al.* Elimination of peripheral auditory pathway activation does not affect motor responses from ultrasound neuromodulation. *Brain Stimulation* **12**, 901–910 (2019).
108. Kim, H. *et al.* Suppression of EEG visual-evoked potentials in rats through neuromodulatory focused ultrasound: *NeuroReport* **26**, 211–215 (2015).
109. Mironov, V., Hritz, M. A., LaManna, J. C., Hudetz, A. G. & Harik, S. I. Architectural alterations in rat cerebral microvessels after hypobaric hypoxia. *Brain Research* **660**, 73–80 (1994).

110. Upton, R. N. Cerebral Uptake of Drugs in Humans. *Clinical and Experimental Pharmacology and Physiology* **34**, 695–701 (2007).
111. Wallace, H., Glazewski, S., Liming, K. & Fox, K. The Role of Cortical Activity in Experience-Dependent Potentiation and Depression of Sensory Responses in Rat Barrel Cortex. *J. Neurosci.* **21**, 3881–3894 (2001).
112. Allen, T. A. *et al.* Imaging the spread of reversible brain inactivations using fluorescent muscimol. *J Neurosci Methods* **171**, 30–38 (2008).
113. Edeline, J.-M., Hars, B., Hennevin, E. & Cotillon, N. Muscimol Diffusion after Intracerebral Microinjections: A Reevaluation Based on Electrophysiological and Autoradiographic Quantifications. *Neurobiology of Learning and Memory* **78**, 100–124 (2002).
114. Musall, S. *et al.* Tactile frequency discrimination is enhanced by circumventing neocortical adaptation. *Nat. Neurosci.* **17**, 1567–1573 (2014).
115. Rossant, C. *et al.* Spike sorting for large, dense electrode arrays. *Nature Neuroscience* **19**, 634 (2016).
116. Arvanitis, C. D., Livingstone, M. S., Vykhodtseva, N. & McDannold, N. Controlled ultrasound-induced blood-brain barrier disruption using passive acoustic emissions monitoring. *PLoS ONE* **7**, e45783 (2012).
117. Kobus, T., Vykhodtseva, N., Pilatou, M., Zhang, Y. & McDannold, N. Safety Validation of Repeated Blood-Brain Barrier Disruption Using Focused Ultrasound. *Ultrasound Med Biol* **42**, 481–492 (2016).
118. Gonmori, K. *et al.* Analysis of ibotenic acid and muscimol in Amanita mushrooms by hydrophilic interaction liquid chromatography–tandem mass spectrometry. *Forensic Toxicology* **30**, 168–172 (2012).

119. Sirsi, S. R. & Borden, M. A. State-of-the-art materials for ultrasound-triggered drug delivery. *Advanced Drug Delivery Reviews* **72**, 3–14 (2014).
120. Kohane, D. S. *et al.* Effectiveness of Muscimol-containing Microparticles against Pilocarpine-induced Focal Seizures. *Epilepsia* **43**, 1462–1468 (2002).
121. Yang, T. *et al.* Enhanced solubility and stability of PEGylated liposomal paclitaxel: In vitro and in vivo evaluation. *International Journal of Pharmaceutics* **338**, 317–326 (2007).
122. Zylberberg, C. & Matosevic, S. Pharmaceutical liposomal drug delivery: a review of new delivery systems and a look at the regulatory landscape. *Drug Delivery* **23**, 3319–3329 (2016).
123. Lanoy, M., Derec, C., Tourin, A. & Leroy, V. Manipulating bubbles with secondary Bjerknes forces. *Applied Physics Letters* **107**, 214101 (2015).
124. Zhang, Y., Zhang, Y. & Li, S. The secondary Bjerknes force between two gas bubbles under dual-frequency acoustic excitation. *Ultrasonics Sonochemistry* **29**, 129–145 (2016).
125. Chen, X., Wang, J., Pacella, J. J. & Villanueva, F. S. Dynamic Behavior of Microbubbles during Long Ultrasound Tone-Burst Excitation: Mechanistic Insights into Ultrasound-Microbubble Mediated Therapeutics Using High-Speed Imaging and Cavitation Detection. *Ultrasound Med Biol* **42**, 528–538 (2016).
126. Klibanov, A. L., Shevchenko, T. I., Raju, B. I., Seip, R. & Chin, C. T. Ultrasound-triggered release of materials entrapped in microbubble–liposome constructs: A tool for targeted drug delivery. *Journal of Controlled Release* **148**, 13–17 (2010).
127. Marmottant, P. & Hilgenfeldt, S. Controlled vesicle deformation and lysis by single oscillating bubbles. *Nature* **423**, 153–156 (2003).

128. Reig, R. & Silberberg, G. Distinct Corticostriatal and Intracortical Pathways Mediate Bilateral Sensory Responses in the Striatum. *Cerebral Cortex* **26**, 4405–4415 (2016).
129. Farkas, T., Kis, Z., Toldi, J. & Wolff, J. R. Activation of the primary motor cortex by somatosensory stimulation in adult rats is mediated mainly by associational connections from the somatosensory cortex. *Neuroscience* **90**, 353–361 (1999).
130. Wunder, A., Schoknecht, K., Stanimirovic, D. B., Prager, O. & Chassidim, Y. Imaging blood-brain barrier dysfunction in animal disease models. *Epilepsia* **53 Suppl 6**, 14–21 (2012).
131. Airan, R. D. *et al.* Noninvasive Targeted Transcranial Neuromodulation via Focused Ultrasound Gated Drug Release from Nanoemulsions. *Nano Letters* **17**, 652–659 (2017).
132. Wang, J. B., Aryal, M., Zhong, Q., Vyas, D. B. & Airan, R. D. Noninvasive Ultrasonic Drug Uncaging Maps Whole-Brain Functional Networks. *Neuron* **100**, 728–738.e7 (2018).
133. Gamou, S., Fukuda, S., Ogura, M., Sakamoto, H. & Morita, S. Microinjection of propofol into the perifornical area induces sedation with decreasing cortical acetylcholine release in rats. *Anesthesia and Analgesia* **111**, 395–402 (2010).
134. Bystritsky, A. *et al.* A review of low-intensity focused ultrasound pulsation. *Brain Stimulation* **4**, 125–136 (2011).
135. Khuri-Yakub, B. T. & Oralkan, Ö. Capacitive micromachined ultrasonic transducers for medical imaging and therapy. *J Micromech Microeng* **21**, 054004–054014 (2011).
136. Yoon, H.-S. *et al.* Ex-vivo HIFU experiments using a 32×32 -element CMUT array. *IEEE Trans Ultrason Ferroelectr Freq Control* **63**, 2150–2158 (2016).
137. Murrough, J. W. *et al.* Rapid and longer-term antidepressant effects of repeated ketamine infusions in treatment-resistant major depression. *Biol. Psychiatry* **74**, 250–256 (2013).

138. Serafini, G., Howland, R. H., Rovedi, F., Girardi, P. & Amore, M. The role of ketamine in treatment-resistant depression: a systematic review. *Curr Neuropharmacol* **12**, 444–461 (2014).
139. Krishna, V., Sammartino, F. & Rezai, A. A Review of the Current Therapies, Challenges, and Future Directions of Transcranial Focused Ultrasound Technology: Advances in Diagnosis and Treatment. *JAMA Neurology* **75**, 246 (2018).
140. Hynynen, K. & Jolesz, F. A. Demonstration of Potential Noninvasive Ultrasound Brain Therapy Through an Intact Skull. *Ultrasound in Medicine & Biology* **24**, 275–283 (1998).
141. Poon, C., McMahon, D. & Hynynen, K. Noninvasive and targeted delivery of therapeutics to the brain using focused ultrasound. *Neuropharmacology* **120**, 20–37 (2017).
142. Szablowski, J. O., Lue, B., Lee-Gosselin, A., Malounda, D. & Shapiro, Mi. G. Acoustically Targeted Chemogenetics for Noninvasive Control of Neural Circuits. (2018)
doi:10.1101/241406.
143. Kinoshita, M., McDannold, N., Jolesz, F. A. & Hynynen, K. Noninvasive localized delivery of Herceptin to the mouse brain by MRI-guided focused ultrasound-induced blood-brain barrier disruption. *Proceedings of the National Academy of Sciences* **103**, 11719–11723 (2006).
144. McDannold, N. *et al.* Targeted, noninvasive blockade of cortical neuronal activity. *Scientific Reports* **5**, (2015).
145. Quadri, S. A. *et al.* High-intensity focused ultrasound: past, present, and future in neurosurgery. *Neurosurgical Focus* **44**, E16 (2018).
146. Zhou, Y.-F. High intensity focused ultrasound in clinical tumor ablation. *World Journal of Clinical Oncology* **2**, 8 (2011).

147. Chang, J. W., Min, B.-K., Kim, B.-S., Chang, W. S. & Lee, Y.-H. Neurophysiologic Correlates of Sonication Treatment in Patients with Essential Tremor. *Ultrasound in Medicine & Biology* **41**, 124–131 (2015).
148. Martin, E., Jeanmonod, D., Morel, A., Zadicario, E. & Werner, B. High-intensity focused ultrasound for noninvasive functional neurosurgery. *Annals of Neurology* **66**, 858–861 (2009).
149. Tyler, W. J., Lani, S. W. & Hwang, G. M. Ultrasonic modulation of neural circuit activity. *Current Opinion in Neurobiology* **50**, 222–231 (2018).
150. Kubanek, J. *et al.* Ultrasound modulates ion channel currents. *Scientific Reports* **6**, (2016).
151. Ferri, M., Bravo, J. M., Redondo, J. & Sánchez-Pérez, J. V. Enhanced Numerical Method for the Design of 3-D-Printed Holographic Acoustic Lenses for Aberration Correction of Single-Element Transcranial Focused Ultrasound. *Ultrasound in Medicine & Biology* **45**, 867–884 (2019).
152. Clement, G. T. & Hynynen, K. A non-invasive method for focusing ultrasound through the human skull. *Physics in Medicine and Biology* **47**, 1219–1236 (2002).
153. Hughes, A. & Hynynen, K. Design of patient-specific focused ultrasound arrays for non-invasive brain therapy with increased trans-skull transmission and steering range. *Physics in Medicine & Biology* **62**, L9–L19 (2017).
154. Jolesz, F. A. MRI-guided focused ultrasound surgery. *Annu. Rev. Med.* **60**, 417–430 (2009).
155. Kamimura, H. A. S. *et al.* Chirp- and random-based coded ultrasonic excitation for localized blood-brain barrier opening. *Physics in Medicine and Biology* **60**, 7695–7712 (2015).

156. Maimbourg, G., Houdouin, A., Deffieux, T., Tanter, M. & Aubry, J.-F. 3D-printed adaptive acoustic lens as a disruptive technology for transcranial ultrasound therapy using single-element transducers. *Physics in Medicine & Biology* **63**, 025026 (2018).
157. Jiménez-Gambín, S., Jiménez, N., Benlloch, J. M. & Camarena, F. Holograms to Focus Arbitrary Ultrasonic Fields through the Skull. *Physical Review Applied* **12**, (2019).
158. Bing, C. *et al.* Trans-cranial opening of the blood-brain barrier in targeted regions using a stereotaxic brain atlas and focused ultrasound energy. *Journal of Therapeutic Ultrasound* **2**, 13 (2014).
159. O'Reilly, M. A., Muller, A. & Hynynen, K. Ultrasound Induced Loss of Rat Parietal Bone Appears to Be Proportional to Animal Mass at Submegahertz Frequencies. *Ultrasound in Medicine & Biology* **37**, 1930–1937 (2011).
160. InSightec. ExAblate® Model 4000 Type 1 Application: Brain Essential Tremor: Information for prescribers. 2016 System Software Version 6.6. FDA Submission July 2016 Online: http://www.accessdata.fda.gov/cdrh_docs/pdf15/P150038C.pdf. (2016).
161. Pichardo, S., Sin, V. W. & Hynynen, K. Multi-frequency characterization of the speed of sound and attenuation coefficient for longitudinal transmission of freshly excised human skulls. *Physics in Medicine and Biology* **56**, 219–250 (2011).
162. Archer, D. P. & Ravussin, P. A. [Role of blood-brain barrier in cerebral homeostasis]. *Ann Fr Anesth Reanim* **13**, 57–61 (1994).
163. Sweeney, M. D., Zhao, Z., Montagne, A., Nelson, A. R. & Zlokovic, B. V. Blood-Brain Barrier: From Physiology to Disease and Back. *Physiol. Rev.* **99**, 21–78 (2019).
164. Abbott, N. J., Patabendige, A. A. K., Dolman, D. E. M., Yusof, S. R. & Begley, D. J. Structure and function of the blood-brain barrier. *Neurobiol. Dis.* **37**, 13–25 (2010).

165. Pardridge, W. M. The blood-brain barrier: Bottleneck in brain drug development. *NeuroRX* **2**, 3–14 (2005).
166. Pajouhesh, H. & Lenz, G. R. Medicinal chemical properties of successful central nervous system drugs. *NeuroRX* **2**, 541–553 (2005).
167. Lam, M. F., Thomas, M. G. & Lind, C. R. P. Neurosurgical convection-enhanced delivery of treatments for Parkinson's disease. *Journal of Clinical Neuroscience* **18**, 1163–1167 (2011).
168. Zhou, Z., Singh, R. & Souweidane, M. M. Convection-Enhanced Delivery for Diffuse Intrinsic Pontine Glioma Treatment. *Curr Neuropharmacol* **15**, 116–128 (2017).
169. Hersh, D. S. *et al.* Evolving Drug Delivery Strategies to Overcome the Blood Brain Barrier. *Curr. Pharm. Des.* **22**, 1177–1193 (2016).
170. Merkus, F. W. H. M. & van den Berg, M. P. Can nasal drug delivery bypass the blood-brain barrier?: questioning the direct transport theory. *Drugs R D* **8**, 133–144 (2007).
171. Gabathuler, R. Approaches to transport therapeutic drugs across the blood-brain barrier to treat brain diseases. *Neurobiol. Dis.* **37**, 48–57 (2010).
172. Burgess, A. & Hynynen, K. Drug delivery across the blood-brain barrier using focused ultrasound. *Expert Opin Drug Deliv* **11**, 711–721 (2014).
173. Tsai, H.-C. *et al.* Safety evaluation of frequent application of microbubble-enhanced focused ultrasound blood-brain-barrier opening. *Scientific Reports* **8**, (2018).
174. Downs, M. E., Buch, A., Karakatsani, M. E., Konofagou, E. E. & Ferrera, V. P. Blood-Brain Barrier Opening in Behaving Non-Human Primates via Focused Ultrasound with Systemically Administered Microbubbles. *Scientific Reports* **5**, 15076 (2015).

175. Lipsman, N. *et al.* Blood–brain barrier opening in Alzheimer’s disease using MR-guided focused ultrasound. *Nature Communications* **9**, 2336 (2018).
176. Mooney, S. J., Nobrega, J. N., Levitt, A. J. & Hynynen, K. Antidepressant effects of focused ultrasound induced blood-brain-barrier opening. *Behavioural Brain Research* **342**, 57–61 (2018).
177. Todd, N. *et al.* Modulation of brain function by targeted delivery of GABA through the disrupted blood-brain barrier. *Neuroimage* **189**, 267–275 (2019).
178. Sweeney, M. D., Sagare, A. P. & Zlokovic, B. V. Blood-brain barrier breakdown in Alzheimer disease and other neurodegenerative disorders. *Nature Reviews. Neurology* **14**, 133–150 (2018).
179. Pandis, D. & Scarneas, N. Seizures in Alzheimer Disease: Clinical and Epidemiological Data: Seizures in Alzheimer Disease. *Epilepsy Currents* **12**, 184–187 (2012).
180. Nation, D. A. *et al.* Blood-brain barrier breakdown is an early biomarker of human cognitive dysfunction. *Nature Medicine* **25**, 270–276 (2019).
181. Montagne, A., Zhao, Z. & Zlokovic, B. V. Alzheimer’s disease: A matter of blood–brain barrier dysfunction? *Journal of Experimental Medicine* **214**, 3151–3169 (2017).
182. Yang, Y. *et al.* Cavitation dose painting for focused ultrasound-induced blood-brain barrier disruption. *Scientific Reports* **9**, (2019).



MEHMET SIRIN OZDAS

Education

Swiss Federal Institute of Technology, D-ITET, Switzerland

PhD Student: FUS mediated non-invasive targeted drug delivery for CNS disorders with simultaneous in-vivo electrophysiology assessment (2014-2019)

Massachusetts Institute of Technology, RLE, ECSC, USA

Visiting PhD Student: FUS mediated non-invasive targeted drug delivery (2014-2015)

Institute of Neuroinformatics, UZH and ETH Zurich, Switzerland

PhD Student: Neuromorphic chips for brain machine Interfaces (2012-2014)

Imperial College London, EEE, UK

MSc in Analogue and Digital Integrated Circuit Design: A bio-inspired associative memory cell in CMOS (2010-2011)

Nagoya Institute of Technology, EEE, Japan

Department of Electrical and Electronic Engineering: Carbon nanotubes for nanoelectromechanical systems(2008-2009)

Kahramanmaras Sutcu Imam University, Turkey

BSc in Electrical and Electronics Engineering with Honor, **top student in the last 3 years.** (2004-2008)

Awards

CNS Fellowship, USA (2013), Novartis Biotechnology Leadership (2016), Turkish National Ministry of Education Scholarship for Graduate Studies (2010-2016)

Employment

Research Assistant, Institute of Neuroinformatics; Zurich, 2013-2014

Brain inspired brain machine interfaces; Programming of neuromorphic chips for neural data classification.

Research Assistant, Swiss Federal Institute of Technology Zurich, 2015-2019

Focused Ultrasound mediated targeted drug delivery for CNS disorders, in-vivo electrophysiology, data analysis, transcranial Focused Ultrasound Neuromodulation, High speed skull effect analysis of FUS beams, FUS induced Blood Brain Barrier opening.

Teaching Experience

Swiss Federal Institute of Technology Zurich, 2016-2018

Teaching Assistant for Bioelectronics and Biosensors course.

Presentations

Exploring AER Protocol and Implementing in FPGAs, Capo Caccia Cognitive Neuromorphic Engineering Workshop, Italy, 2012

Signal Processing for Brain Machine Interfaces, Capo Caccia Cognitive Neuromorphic Engineering Workshop, Italy, 2013

Invited Talks

“Non-invasive, receptor-specific, millimeter-precision manipulation of brain circuits” Neuro-vascular-glia network Seminar, Zurich, July, 2019 (During PhD)

Conference Abstracts

“Towards real time classification of neural recordings in neuromorphic hardware”

Mehmet Ozdas, Giacomo Indiveri, ISNNE, 2014, Tokyo Japan

“Spatially and temporally controlled, non-invasive, receptor specific neuromodulation using focused ultrasound” Aagam Shah, **Mehmet Sirin Ozdas**, Paul Johnson, Tansel Baran Yasar, Nisheet Patel, Shashank Sirsi, Markus Marks, Mehmet Fatih Yanik, NBBE, Switzerland, 2017 (During PhD)

“Millimeter-precision, non-invasive, receptor-specific manipulation of brain circuits”, **Mehmet Sirin Ozdas**, Aagam Shah, Paul Johnson, Markus Marks, Tansel Baran Yasar, Wolfger von der Behrens and Mehmet Fatih Yanik (OPTO-DBS Conference, June, 2019, Geneva Switzerland) (During PhD)

Journal Articles

“Programmable Spike-Timing Dependent Plasticity learning circuits in neuromorphic VLSI architectures”, JETC- ACM, Mostafa Azgahdi, Saber Moradi, Daniel B. Fasnacht, **Mehmet Ozdas** and Giacomo Indiveri, May 2015.

“Multiscale Modeling of transcranial focused ultrasound neurostimulation and experimental validation: initial results” Hazael Montanaro, **Mehmet S. Ozdas**, Esra Neufeld, Théo Lemaire, Silvestro Micera, Mehmet F. Yanik and Niels Kuster Journal of Therapeutic Ultrasound, vol. 6: no. S1, pp. 77-78, London: BioMed Central, 2018. (During PhD)

“Non-invasive, receptor-specific, millimeter-precision manipulation of brain circuits”, **Mehmet Sirin Ozdas**, Aagam Shah, Paul Johnson, Markus Marks, Tansel Baran Yasar, Wolfger von der Behrens and Mehmet Fatih Yanik (in revision, Nature Communications, 2019) (During PhD)

Transient Seizures followed by transcranial Focused Ultrasound mediated Blood Brain Barrier opening, **Mehmet Sirin Ozdas**, Aagam S. Shah, Paul M. Johnson and Mehmet Fatih Yanik (Manuscript in preparation, 2019) (During PhD)

Curriculum Vitae

“Automated 3D-scanning system for fast characterization of transcranial focused ultrasound fields in rodent skull”, **Mehmet Sirin Ozdas**, Hazael Montanaro, Paul M. Johnson, Aagam S. Shah, Esra Neufeld, Niels Kuster and Mehmet Fatih Yanik (Manuscript in preparation, 2019) (During PhD)
